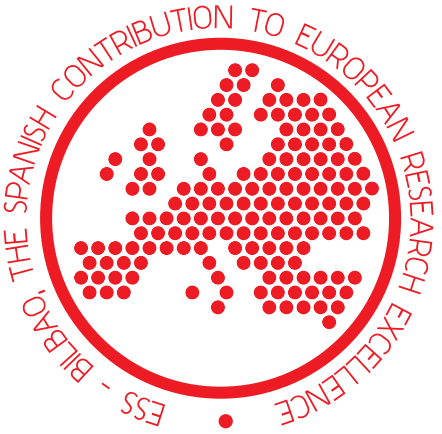

EQUIPMENT SPECIFICATION DOCUMENT:

SPALLATION MATERIAL

Reference:	ESS-0058358
Date:	September 16, 2016
Revision:	0.0

Author	Review	Aprobed
A. Aguilar	F. Sordo	J. L. Martinez
M. Magan	J. L. Martinez	
I. Herranz		
F. Sordo		
T. Mora		
R. Vivanco		
G. Bakedano		
J. Aguilar		
L. Mena		
M. Mancisidor		
J. L. Martinez		

Contents

1 Introduction

Neutron Spallation sources are devices designed to produce neutrons from spallation nuclear reactions. In order to produce this kind of reactions it is necessary to accelerate protons (H+ particles) using electromagnetic fields up to they get a huge amount of kinetic energy or speed close to light velocity. In that moment, protons are led to impact on a nucleus of a heavy atom (generally mercury, lead or tungsten) producing what it is known as spallation reaction.

The place where the reaction is produced it is known as Spallation Target and it is considered the neutron source. This Targets are complex devices, from an engineering point of view, where a huge amount of heat is deposited on the spallation material. In some cases, it is note that the heat density in the spallation target can be higher than fuel bars inside a nuclear power reactor, as a consequence the design of Spallation Target is a real engineering challenge. The ESS target is one of these cases.

The European Spallation Source (ESS) is an ambitious European project with a budget higher to 1800 M€. The aim of the project is to design, build and operate the most important and the bright spallation neutron source in the world. The ESS will use a proton beam with final power deposited on the target of 5 MW (five times higher than SNS and JPARC), which will impact on a tungsten Target cooled by helium gas.

The Target will be designed with a set of tungsten blocks placed inside of a wheel of 2.5-2.6 meter of diameter. Protons will impact at high speed on the wheel in a radial direction. Inside the wheel, helium flows at high velocity, cooling the tungsten blocks dissipating the heat produced by the nuclear reactions. The wheel rotates at a speed of 0.2-0.5 Hz, so the proton beam impacts on a different region of the wheel at a repetition rate of 14Hz, distributing the heat over the whole perimeter of the wheel.

The purpose of this report is to describe the following points that justify the technical decisions associated with the spallation material:

- Loads and requirements
- Optimization process for geometrical configuration
- Methodology developed for Tungsten matrix analysis
- Thermomechanical condition on normal operations (SF1 and SF2)
- Thermomechanical condition on accidental cases (SF3 and SF4)

It should be remarked that Spallation material is not included the list of Target elements that have to fulfill the RCC-MRx design rules. However, the classification of the operational events and loads will be done based on RCC-MRx, in order to be consistent with other elements that have to follow RCC-MRx rules.

2 Loads scenarios

The operational conditions that the component have to withstand along its life time are defined as "load scenarios". The load scenarios are classified based on SF levels[2]:

- SF 1 and 2 are operating conditions associated with Normal operation, start and stop, and normal operational incidents.
- SF 3 Conditions are Operating Conditions which are rare and leads to shutdown and inspection, limit to 10 times in the lifetime.
- SF 4 Conditions are highly improbable but relevant for safety.

Based on the inspection conditions and actions after the scenario, a protection level is associated with the component (Level A,C or D). For the spallation material, inspection is not possible so, events are classified on Levels A (Restart is possible after the event) or D (Restart is not possible after the event). Its maximum operational conditions are defined on section 3 with a soft equivalence to Level classification that is shown on Table 2.

Regarding the different operational scenarios, the Table 1 shows the classification of the events considered for the spallation material design and its protection level. It should be remarked that spallation material is not an equipment under pressure so, the level criteria is only included as indication. Moreover, it should be notice that additional accidental conditions will be consider for licensing purposes, but they are not in the scope of this document.

The Table shows several accidental cases in which the engineering solution for the spallation material will no play a significant role for the behaviors of the whole system. This loads conditions will be evaluated on safety analysis documents [?], but they are not in the scope of this document. The following load cases will not be considered:

- Failure of rastering magnets: This accidental conditions produce a focused beam with one order of magnitude more heat load compared with the design beam. The impact of the beam produces an increase of temperature in the range of thousand degrees in that situation any available cooling conditions will not play a significant role. That means that any spallation material configuration under this beam will be above the design conditions for the spallation material in a single pulse. Based on that the accident is not relevant for design proposes.
- Stationary wheel: If the wheel stops without shutdown the beam, the temperature of the spallation material will increase $\sim 100^oC$ per pulse. The time in between pulses is only 71 ms (14 Hz repetition rate), then in the best conditions, the temperature can be reduce $\sim 4 - 10^oC$ during the cooling period. Due to that, 4 pulses after stopping the wheel the spallation material is above the conditions summarized on Ref. 3 for any cooling configuration. Based on that facts this accident is not relevant for design proposes.

Requirement	**Loads**	**Level**	**Prot.**
Operating Conditions	Nominal Beam [4] Operating pressure (10 bar) Operational cooling conditions (3 kg s^{-1}) Wheel rotation	SF1	A
Vertically displaced beam	Vertically displaced beam Operating pressure (10 bar) Operational cooling conditions (3 kg s^{-1}) Wheel rotation	SF2	A
Unsynchronized wheel	Horizontally displaced beam Operating pressure (10 bar) Operational cooling conditions (3 kg s^{-1}) Wheel rotation	SF2	A
Failure of rastering magnets	Non Raster beam Operating pressure (10 bar) Operational cooling conditions (3 kg s^{-1}) Wheel rotation	SF3	D
Loss of coolant flow and pressure	Nominal beam Operating pressure ($<$ 10 bar) Operational cooling conditions ($<$ 3 kg s^{-1}) Wheel rotation	SF3	D
Stationary wheel	Nominal beam [4] Operating pressure ($<$ 10 bar) Operational cooling conditions ($<$ 3 kg s^{-1}) Wheel stopped	SF3	D
Shut-down	No beam Operating pressure (10 bar) No coolant flow Wheel stopped	SF3	D

Table 1: Operational Scenarios identified for the Spallation Material[3]

3 Materials properties and operational limits

The proton beam produced by the accelerator interacts with the spallation material to produce neutrons. This process will generate a significant heat deposition, which will produces a sharp increase of temperature during the proton pulse. Due to the thermal expansion produces by this increase of temperature, the spallation material have to support high cyclic thermal stresses.

This operational conditions drives the selection of the target concept. Based on this boundary condition the following design criteria were identified[6]:

Requirement	**Rationale**	**Level**
Tungsten maximum temperature during normal operation shall be below 500^o	ESS-0009043	A
Tungsten maximum temperature during SF2 accidents below 600^o	ESS-0009043	A
Tungsten maximum temperature during accidents shall be below 700^oC	ESS-0009043	D
Tungsten averaged maximum stress shall be below 100 MPa	ESS-0009043	A
Tungsten post-pulse peak stress shall be below 50 MPa	ESS-0009043	A

Table 2: Requirements for the spallation material [6]

The values proposed in the Table 2 for the stress conditions are far below the mechanical limits of the material. It should be remarked that the tungsten will suffer damages above 1 dpa in a few months of operation (See section 9), so it should be considered as a brittle material and based on that, the acceptable stress levels are significantly reduced.

Regarding the thermomechanical properties a detail description can be found on ESS Target Materials Handbook [5]. Unless is specified differently, the simulation models included in this document are consistent with the parameters specified in the ESS Target Materials Handbook.

4 ESS Target configuration

The configuration of a 5 MW Spallation target is complex process and there is no an unique solution. Also it should be remark that most of the activated material produced in the spallation reactions will be confine in the target. For that reason the target design is close related to ESS safety issues. In order to guide the selection of the target concept, ESS organized a working group in order to explore several Target options (Target Selection Concept Phase, TSCP). This working group explored several target options from 2010 to 2012[1].

After this process, ESS selected as final solution a solid rotating target cooled by helium. This solution was developed further by ESS and KIT along 2012-2013 and its final concept is summarized on the TDR proposal.

On November 2014, ESS-Bilbao was choose as in-kind partner for Target Wheel, shaft and drive unit. The redesign works started on January 2015. Along this period, ESS-Bilbao has follow and optimization process summarized on the Report [8] that arrives to a new base line proposal in June 2015. The previous configurations analysis is not in the scope of this document.

The proposed new target configuration is based on 10x30x80 mm^3 tungsten bricks. These tungsten bricks are placed on an steel support (the cassette), in a cross flow configuration as it is shown on Figure 1. The coolant will move in the gap in between bricks removing the heat deposited by the proton beam.

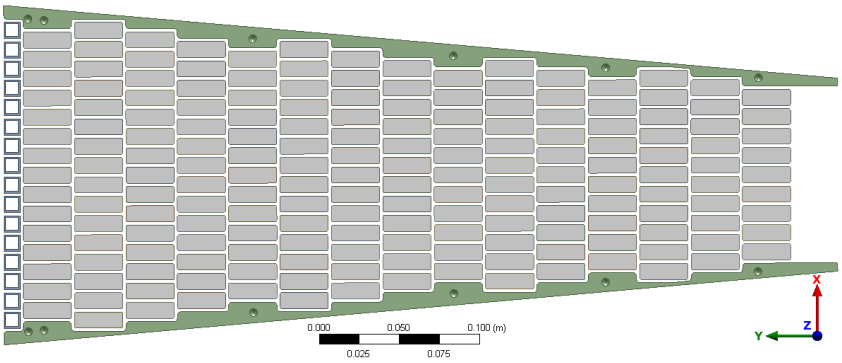

Figure 1: Tungsten bricks(grey) and turbulence generators final (blue) configuration on a Target Wheel sector.

The cassette withstand tungsten bricks and configures the inlet helium channels in the gap between ribs and target vessel (Figure 3). Finally, 36 of these cassettes will be assembled in a sectored wheel as it is shown on Figure 2.

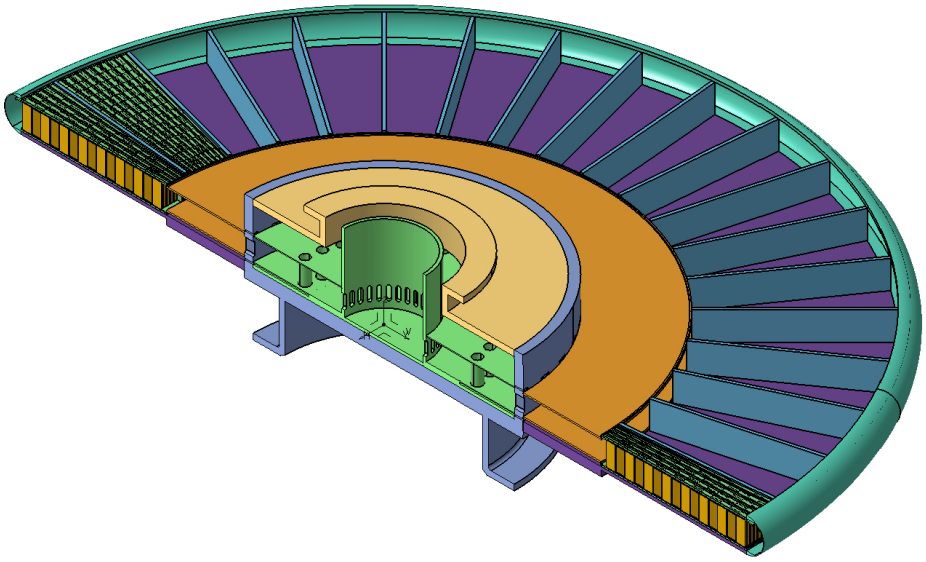

Figure 2: Target wheel configuration

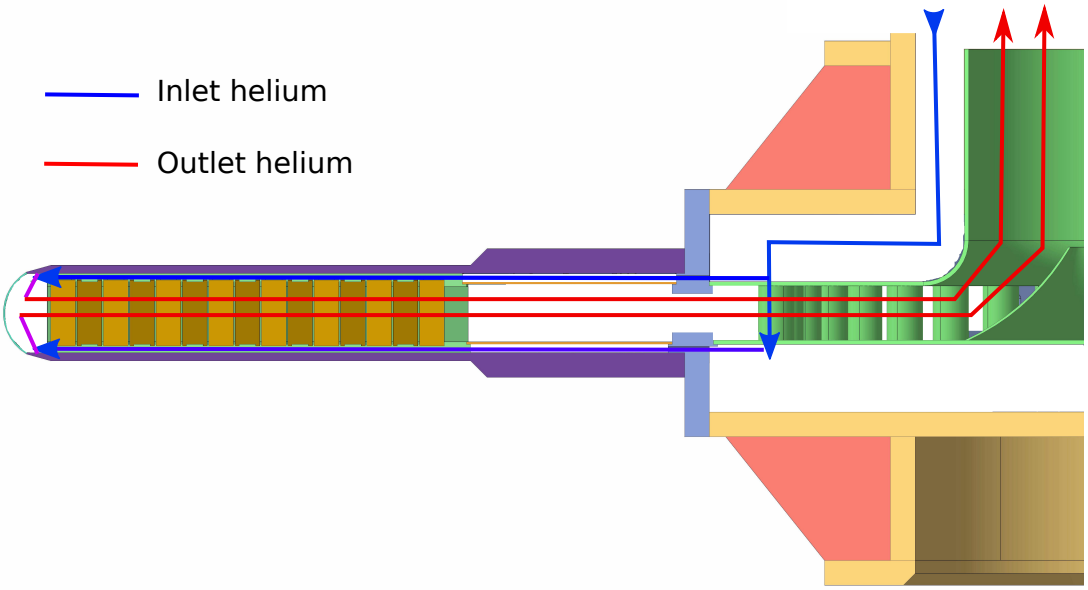

Figure 3: Target wheel helium flow

5 Tungsten bricks configuration

The spallation material is composed by 186 bricks of tungsten disposed in a "cross flow" configuration thus avoiding having a free stream where protons could cross the target without interacting (Figure 1). The bricks are separated from each other 2 mm. The dimensions of a single brick are 10x30x80 mm^3 (Figure 4), the coolant flow is parallel to the transverse dimension (30 mm) of the tungstenÕs brick.

The relative position between bricks is defined by grooves machined in the top and bottom covers of the cassette. The adjustment in between grooves and spallation material produces a gap in between 20-100 $\mu - m$ at room temperature. Under operational conditions, the gap increases up to 200 μ, due to the different thermal expansion coefficients of the different materials. A simplified experimental set-up with 11 brick was produce to make a vibration test of the actual set-up[10]. The results of this vibrational test do not shown any significant powder production due to W bricks movements against the steel frame of the cassette.

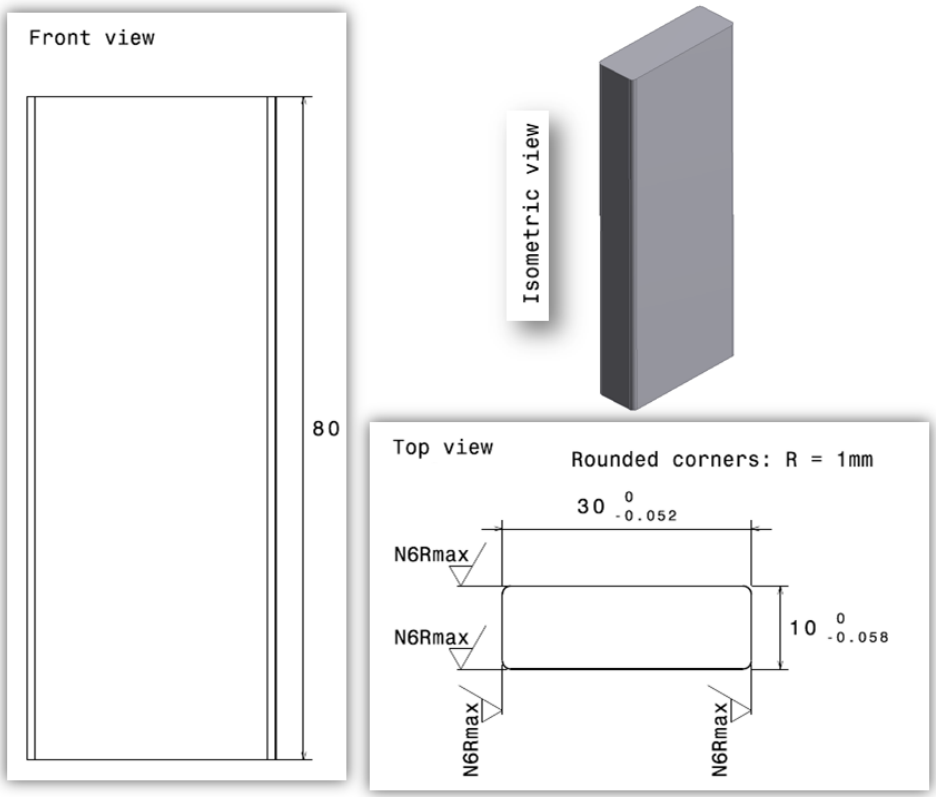

Figure 4: Tungsten brick dimensions and tolerances.

6 Optimization process

The analysis carried out along 2015 shows that TDR configuration [7] do not fulfill the operational stress limits for the Spallation material (Table 2). Thus, in order to reduce the maximum stress values, the tungsten slabs have to be splitted up horizontally producing a much more complex geometry.

On this point ESS-Bilbao proposed the brick configuration described in the previous section. The optimization process carried on to achieve the optimal main geometrical dimensions of the bricks was summarized on previous reports [8]. To complete the optimization process additional analysis has been completed based on the detail CFD analysis described on Section 7. The next sections show the final steps of this design optimization process, in which we propose to introduce as final configuration the rounded bricks and turbulence generators.

6.1 Tungsten bricks rounding

The initial configuration based on bricks on cross flow configuration, considers sharp angles in order to simplify the tungsten manufacturing process. This sharp corners increase significantly the turbulence in the helium flow, then increasing the heat transfer coefficient. However, they are a conflictive region for mechanical fatigue and erosion processes. As a consequence, materials experts recommends to round it the cornerÕs shape of the W bricks, along the direction of the Helium flow. After studying different configurations and rounding radius it has been concluded that the best option will be to round all the tungsten bricks corners with 1 mm radius.

The optimization studies summarized in this section were performed considering a Target Wheel divided in 33 sectors and the thermal source defined by the ESS TDR of 2013 [7]. Hence, the results are not directly comparable with the thermal models (section 7). However the conclusions of the optimization process can be extended to the final 36 sector configuration with the current thermal source.

In the Table 3 is shown the pressure drop and maximum velocity in the helium flowing trough the bricks and also the maximum temperature in the tungsten bricks. Rounding the sharp corners of the the bricks along the He flow direction allows significantly decrease in the pressure drop, but on the other hand it will increases significantly the maximum temperature in the W bricks. The rounded corners generates a lower turbulence production compared with the sharp corners, this induces the reduction in the pressure drop due to a much more laminar He flow. On the other hand, the He laminar flow is much less efficient removing the heat and this reflected in a signicantly lower heat transfer coefficient.

Rounding (mm)	ΔP (bar)	$v_{max}(\frac{m}{s})$	$T_{max-tungsten}(^oC)$
No rounding	0.25	99	352
1	0.1	76	447

Table 3: Pressure drop, maximum helium velocity and maximum tungsten temperature for W bricks rounded by 1 mm and no rounded

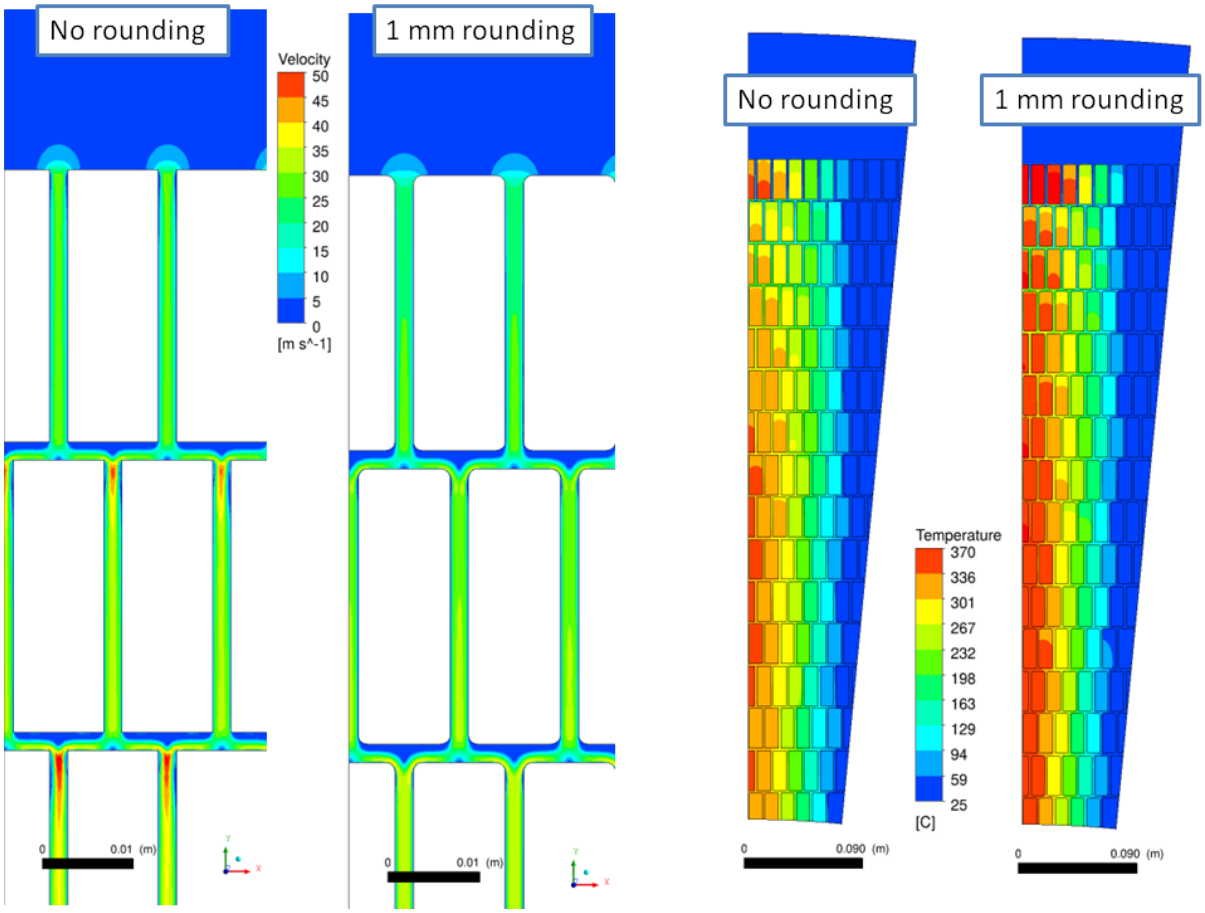

Figure 5: Temperature and velocity profiles comparison between no rounded and 1 mm rounded W bricks.

Hence, rounding the corners has a positive effect on reducing the pressure drop, but the maximum temperature increases. However, the increase of temperature can be limited by the introduction of the turbulence generators in front of the spallation material.

6.2 Turbulence generators

As it was remarked in the previous section, rounding the corners has a negative effect in the maximum temperature due to the lower turbulence production. It is interesting to point out

that the maximum temperature is produced in the first two layers of brick, so a practical solution will be in to increase locally the turbulent in front of this region, in order to improve the heat transfer coefficient, without large impact in the total pressure drop.

Based on this idea, the turbulence generators were included in the design of the upstream of spallation material. This concept is inspired in the proposal for the first layer of rods in the SINQ target[11]. These turbulence generators consist in 16 steel SS-316L hollow bricks which are separated 2 mm from each other and from the first row of bricks, as it is shown in the Figure 1. The dimensions of each single turbulence generator are 10x10x80 mm^3 and it has 1 mm thickness.

The Table 4 contains the results of the CFD optimization analysis. In this study 6 different rounding configuration were simulated to compare the pressure drop and the temperature of the tungsten bricks. The column "Description" of the Table 4 includes the details of the geometry.

Configuration	**Description**	**ΔP (bar)**	**$v_{max}(\frac{m}{s})$**	**$T_{max}(^oC)$**
A	All tungsten bricks and turbulence generators rounded 1 mm	0.1	76	370
B	All tungsten bricks rounded 1 mm and turbulence generators no rounded	0.1	76	367
C	1^{est} row of tungsten bricks no rounded, the others rows 1 mm rounded and turbulence generators no rounded	0.11	76	365
D	1^{est} and 2^{nd} of tungsten bricks no rounded, the others rows 1 mm rounded and turbulence generators no rounded	0.1	76	367
E	All tungsten bricks and turbulence generators no rounded	0.26	102	342
F	Bricks sharp in the symmetry plane, others rounded and turbulence generators	0.11	85	477

Table 4: Pressure drop, maximum helium velocity and maximum tungsten temperature for bricks rounded 1 mm and no rounded.

Configuration E has the lowest maximum tungsten brick temperature, but on the other hand the pressure drop is the highest. Configurations A, B, C and D present a reduction of the pressure drop of the helium due to the rounded corners of most of the elements, also the presence

of the turbulence generators achieves temperatures in the tungsten brick much lower than the configuration with rounded bricks, but no turbulence generators, as presented in Table 3. The maximum temperature in the spallation material, as well as the pressure drop have no major differences between them, as it can be observed in the temperature profiles (Figure 6). The first rows of bricks upstream have lower temperatures in the configurations D and C.

The F case shows a very negative performance due to the difference pressure drop between the channel chose to the symmetry plane and others. The sharp corners in the symmetry plane increases the pressure drop in the central channel and due to that the helium flows less in the center, as a consequence increases the maximum temperature.

Despite the minor differences between cases B,C and D, the configuration B is finally chosen for the Target because it simplifies the assembly of the spallation material.

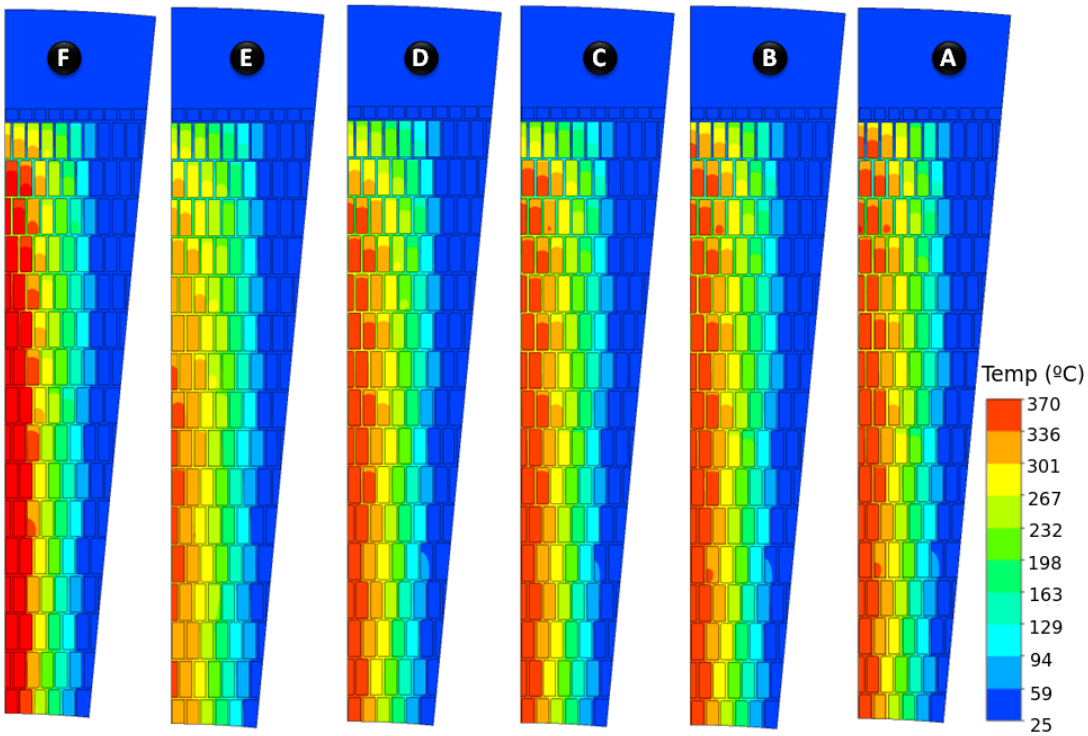

Figure 6: Temperature profile comparison between different configurations with turbulence generators.

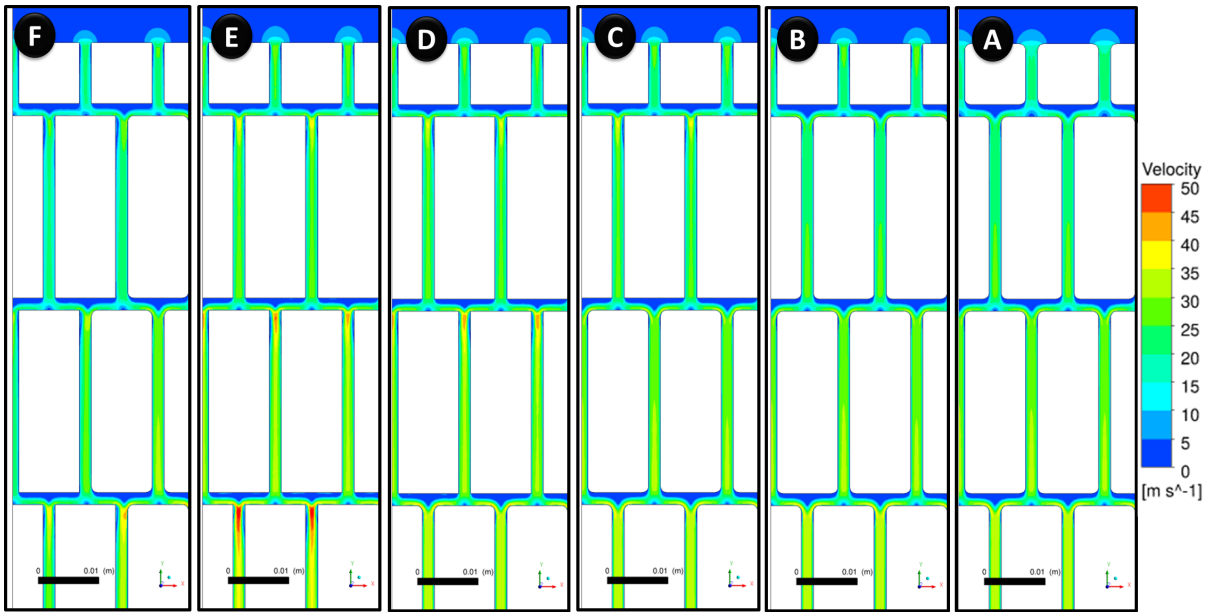

Figure 7: Velocity profile comparison between different configurations with turbulence generators.

7 Methodology

7.1 Particle transport analysis

The radiation transport analysis in complex geometries needs several codes, software and tools to be implemented. This study combine the software *SuperMCAM or MCAD* [12] [**?**], the codes *MCNPX/6* [15] and *ACAB 2008* [14], and the tool developed by the ESS Bilbao Team *GIGANT* [13]:

- ◇ *SuperMCAM or MCAD:* software to convert CAD geometries to MCNP format and other codes.
- ◇ *MCNPX/6:* general-purpose Monte Carlo N-Particle code that can be used for particles transport.
- ◇ *ACAB 2008:* computer program designed to perform activation and transmutation calculations for nuclear applications.
- ◇ *GIGANT:* (General Implemented Geometry Activation Neutron Tool) developed to implement complex geometries for activation calculations.

The methodology used to reach the results is shown in the Figure 8, which summarizes the followed process.

The first step is to transform the CAD geometry into the format used in the code for particles transport, MCNP. The software that does the transformation is SuperMCAM.

The initial geometry has to be modified and simplified in order to make it easily to transform and simulate with the Monte Carlo code. In a general way, the simplification consists on to remove or to change elements that are dispensable, from the neutron transport point of view. Some of these elements are bolts, nuts or chamfers. Moreover, several types of geometries are not able to be transformed to MCNP format, like spirals or surfaces defined with sketches.

The target model transformed by SuperMCAM has been implemented in the ESS Target Station model for MCNP. This model includes a detailed geometry of the target and the shaft with the final helix shape, which are the most important components for the analysis.

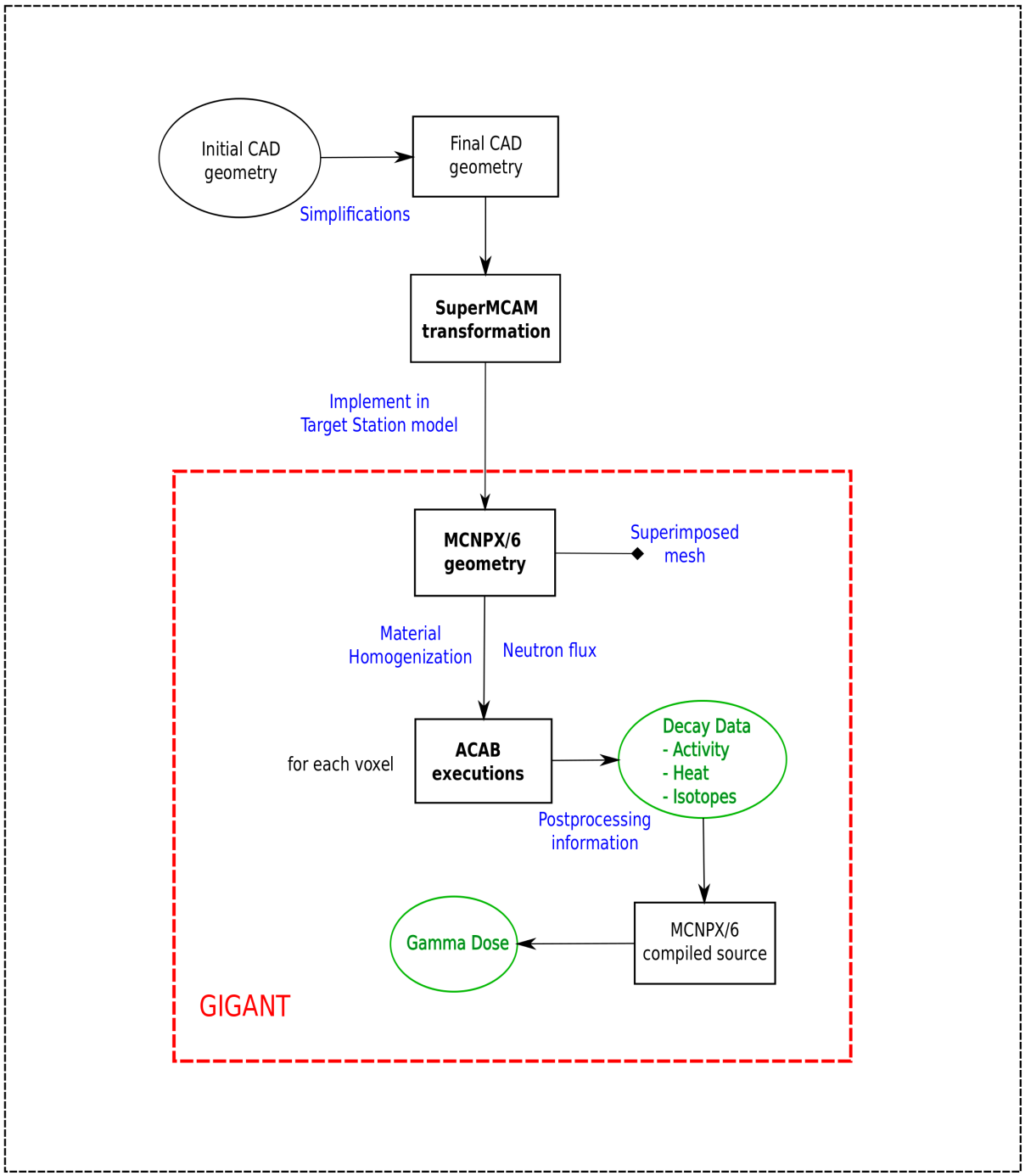

Figure 8: Scheme followed in the calculations from the initial CAD model to the final results.

Figure 9 shows the MCNPX model for the target spallation material. A detailed geometry for one sector has been included, in order to produce high accuracy results for heat load, irradiation damage and streaming proton paths along the wheel. The remaining 35 sectors has been simplify as an homogeneous mixture of helium and tungsten keeping the average density.

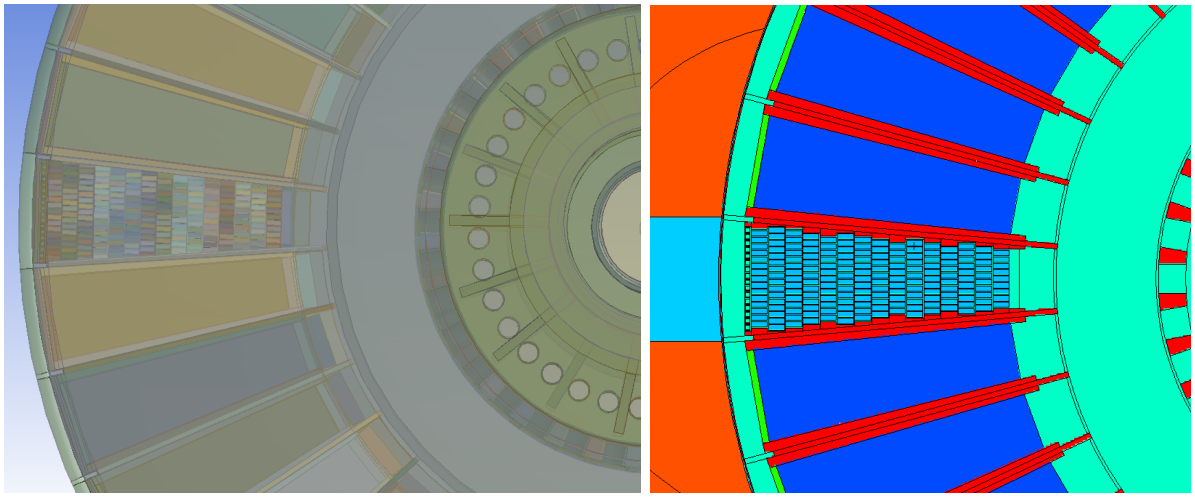

Figure 9: Geometry transformation from CAD model to MCNP format for ESS Target.

7.2 Residual heat methodology

The activation process, which is responsible of the after heat produced by an irradiated target, has two main components: Spallation Residuals and Activation by neutrons.

The spallation residuals are the residual nuclei produced in the spallation process, typically this nuclei needs several decay processes to arrive to a stable configuration. The spallation process is mainly produced by protons on the target material, so these products will be accumulated inside the target wheel. To evaluate these residual nucleus MCNPX intranuclear cascade models are used (CEM03 [18]) and they are introduced in the inventory code as a continuous isotope source. The MCNPX code uses physics models for neutrons above 55 MeV and protons in all the energy range.

The second component in the process is the activation produced by neutrons. The operation of the proton beam on the target will generate an intense neutron flux that will reach the whole set of materials of the Target station. This flux will be greater at target surrounding elements, and will ease off while breaking through the shielding layers. These neutrons can be captured generating an unstable nucleus which will starts a decay chain. The neutron energy spectrum used is the $VITAMIN\ J+$, which higher energy is 55 MeV.

Codes used to perform the calculations are $MCNPX$ [20] and $ACAB$ [14], as shown on Figure

10. MCNPX is a transport code used to evaluate the residual nucleus generation and also the neutron flux. ACAB evaluates the inventory considering the decay process, the external sources (the continuous source of spallation residuals) and the decay and the neutron capture reactions. Libraries used for transport calculations are *ENDF/B-VII.0*; and the multigroup activation libraries to estimate the isotopic inventory used by ACAB are the ones provided by the developers of the code *EAF-2007*.

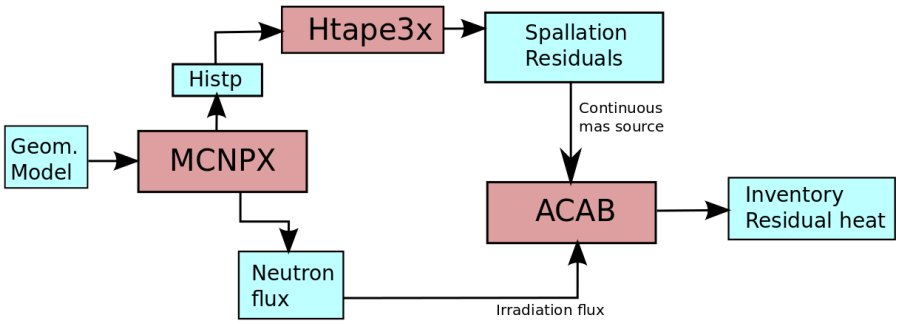

Figure 10: Activation analysis

The aim of this analysis is to determine the evolution of the residual heat and its spacial distribution in the target geometry. In this analysis, the activation of structural materials is not included. The reason is that the contribution to the total after heat is negligible. Basically all of the heat is produced in the target material properly.

7.2.1 Residual heat spatial distribution

The proton beam footprint has a flat distribution and it doesn't impact with all the tungsten. The Figure 11 represent the dimensions of the footprint. Due to the footprint symmetry we are allows to simplified the problem into a quarter symmetry problem.

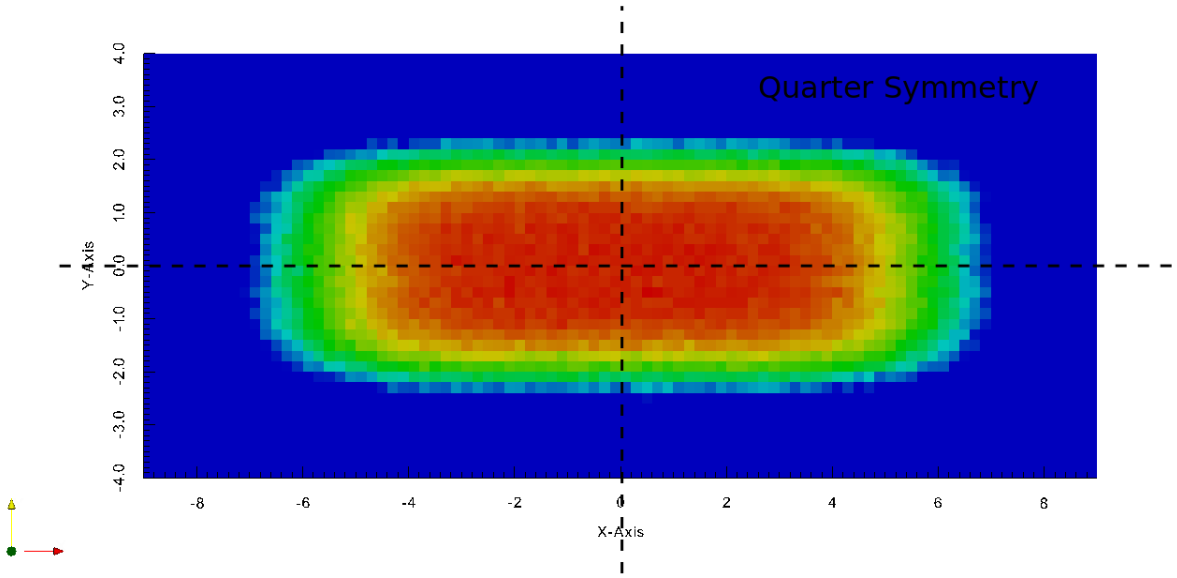

Figure 11: Proton beam footprint, representing the quarter symmetry analysed.

The methodology applied on the spatial distribution analysis follows the previous scheme: neutron transport with MCNPX and activation with ACAB. But some additional considerations have been added: the neutron flux has been analyzed homogeneously with no angular divisions, but the spallation residuals have been analyzed for different angles.

The scheme of the methodology is represented in the Figure 12. It shows the implementation of the two different simulations, using the proper normalization parameters for each case.

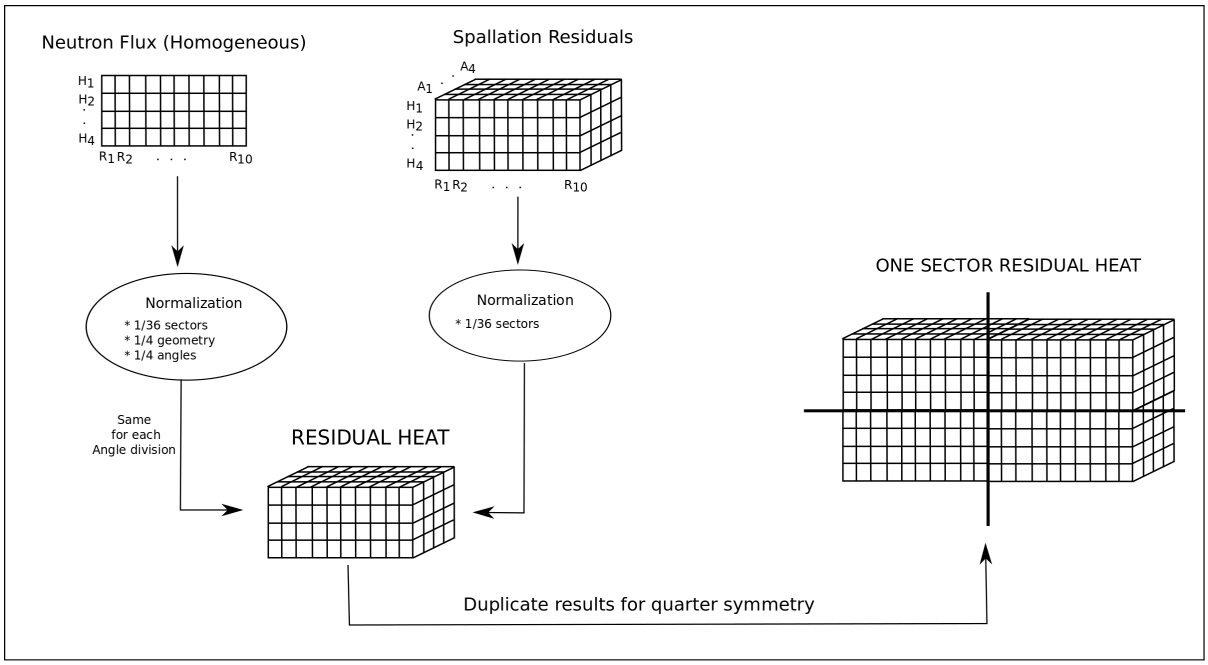

Figure 12: Scheme of the methodology followed to calculate the residual heat, taking into account the proton beam footprint on the target.

For the simulations are 10 divisions in radii, 4 divisions in height and 4 divisions in angle. They corresponds with a quarter of a sector of the whole target wheel (36 sectors). Then, the results have been replicated to complete the total geometry of a sector. The irradiation period has been set at 25000 hours of operation, using a proton beam of 2 GeV and 2.5 mA of average current.

The MCNPX geometry used to the calculations are shown in the Figure 13, that corresponds with the neutron flux calculations (left figure) and the spallation residual calculations (right figure). The residual heat analysis uses a tungsten target with homogeneous density instead of the detailed bricks geometry.

The Figure 14 represents the CAD detailed geometry and the one with the homogeneous density for the tungsten, which is the used for the analysis.

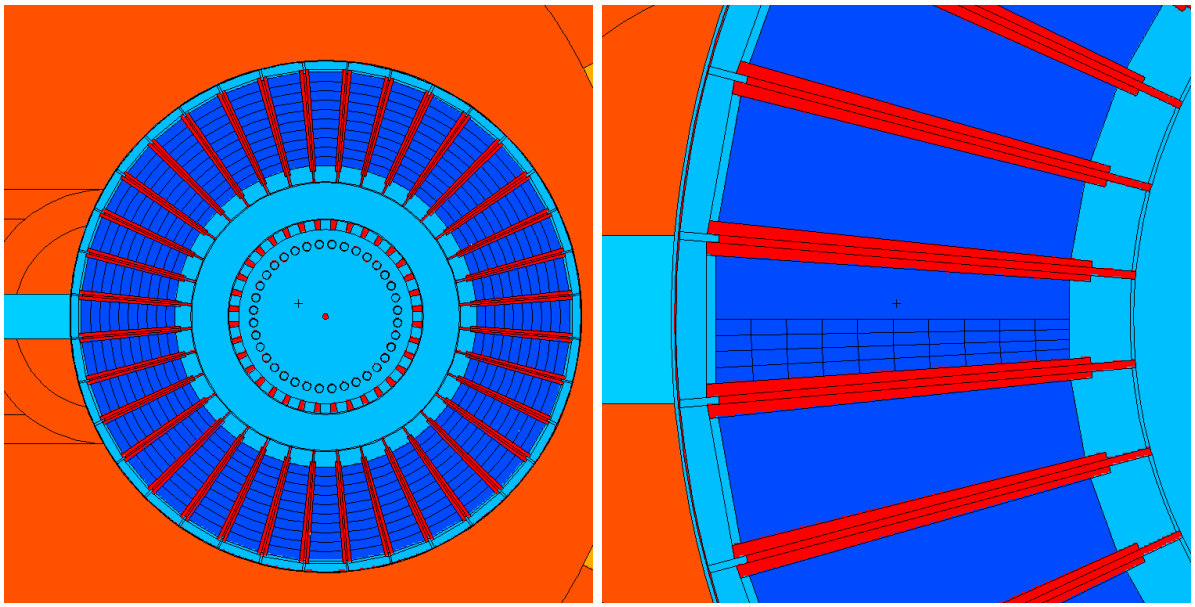

Figure 13: MCNPX geometries for neutron flux homogeneous calculations (left figure) and the spallation residual calculations using angle divisions (right figure).

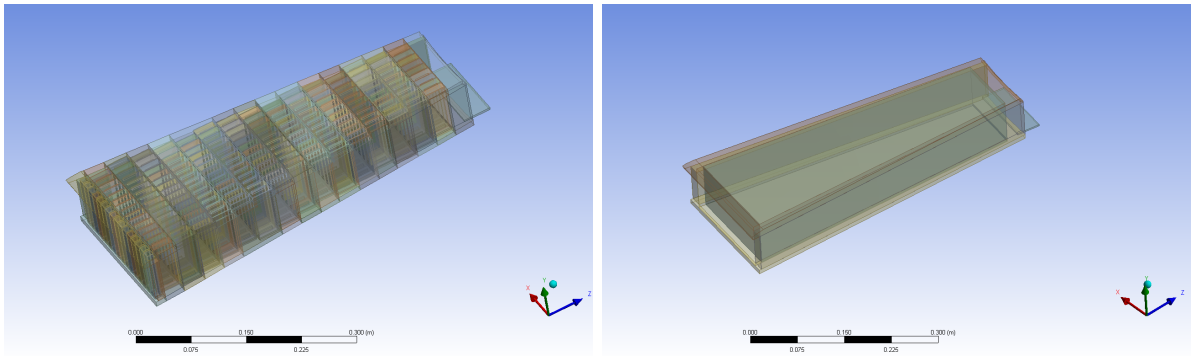

Figure 14: CAD geometries from the detailed tungsten target (left) to the density homogeneous tungsten target (right) .

The MCNPX model used for the calculations has been defined by the next parameters and properties::

- Target material: tungsten and vacuum. Average density 16.1 g/cm^3
- Target volume and mass: $Vol = 1.91 \cdot 10^5\ cm^3$ and 3.089 Tn
- Target dimensions: Cylinder approximation, $R_{int} = 77\ cm$; $R_{ext} = 125\ cm$; $H = 8\ cm$

7.3 CFD modeling

In the cross flow configuration proposed for the spallation material cooling, the turbulence flow has a significant impact on the heat transfer coefficient.

The proper resolution of the turbulence production demands a high density mesh in the fluid-solid interface. The required mesh should have enough number of elements to correctly solve the boundary layer ($y^+ \approx 1-5$).

Due to the complexity of the fluid boundary in contact with the walls of the spallation material and the cassette and the need of a fine boundary layer solving a 3D CFD model of this problem, the computational time and computer resources is prohibitive. As a consequence, some simplifications and assumptions have to be taken into account.

This section shows the methodology developed for the Spallation material transient analysis based on 2D simplified models.

7.3.1 Convection cooling analysis

Transient analysis require solving a lot of time steps, for this reason it has been used a simplified 2D model. The geometry includes the turbulence generators and the tungsten bricks with 1 mm of rounding radius. It is important to remark that the heat source used for the sensitivity analysis in the associated with ESS TDR of 2013 [7], so the maximum temperatures are not comparable the with actual conditions, however the conclusions of the analysis will be still valid.

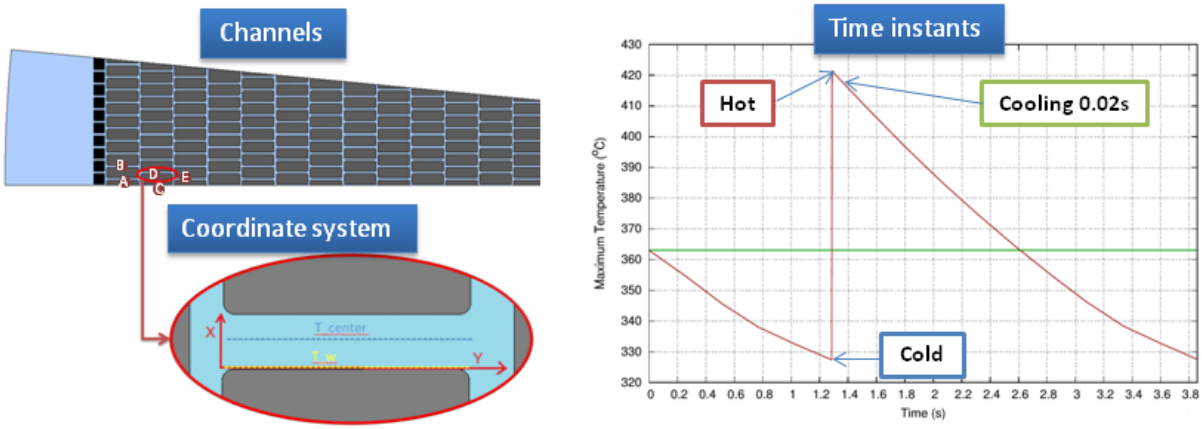

Figure 15: Channels, local coordinate system and instants employed to analyze the tungsten cooling evolution along the time.

In Figure 15 are defined the channels of coolant, where the study was focused and the local coordinate system used to reference the variables. These channels were selected because they

are in contact with the tungsten bricks, where the thermal source is higher. To perform the transient analysis and compare the variables, when time is changing, three instants were chosen:

- **Cold:** is the instant at the end of the cooling process and just before the beam impacts again a particular Target sector, which is 2.56857 s after the end of the previous proton pulse in that particular sector.
- **Hot:** is the time instant just at the end of the 2.86 ms protons beam pulse in the studied Target sector.
- **Cooling 0.02 s:** is the time instant 0.02 s after the end of a the proton pulse in that particular Target sector.

The results of the cooling transient analysis have been used to plot the graphics included in Figures 16, 18 and 17. From these figures, the following conclusions are obtained:

- Helium temperature near the tungsten wall have a considerably variation over time. However the temperature in the helium close to the center of the channel is almost no time dependent, as it is shown in the Figures 16 and 17.
- Over the width of the channel helium temperature has a sloping shape near the wall (thermal boundary layer), but in the center of the channel the profile is flat (outside the thermal boundary layer).
- Heat transfer coefficient between helium and walls the tungsten is practically invariant over the time $h(y) = q" \cdot (T_{wall} - T_{center})^{-1}$, as showed in Figure 18.

If it is considered that the heat transfer coefficient and the bulk temperature are no time dependent variables, the fluid-solid uncoupling is allowed to solve our problem. This means that a convection boundary condition (BC) on the surfaces in contact with helium could be calculated from a steady state simulation and this BC will not vary over the time.

The BC basically consist in heat transfer coefficient and a helium bulk temperature values associated with each point of the solid surface in contact with the helium fluid, that once calculated from a steady state CFD simulation, it can be introduced in a thermal FEM model where only solids are taken into account. As result the thermal and stress distribution of the spallation material and the cassette can be solved reducing the computational resources and time to something reasonable.

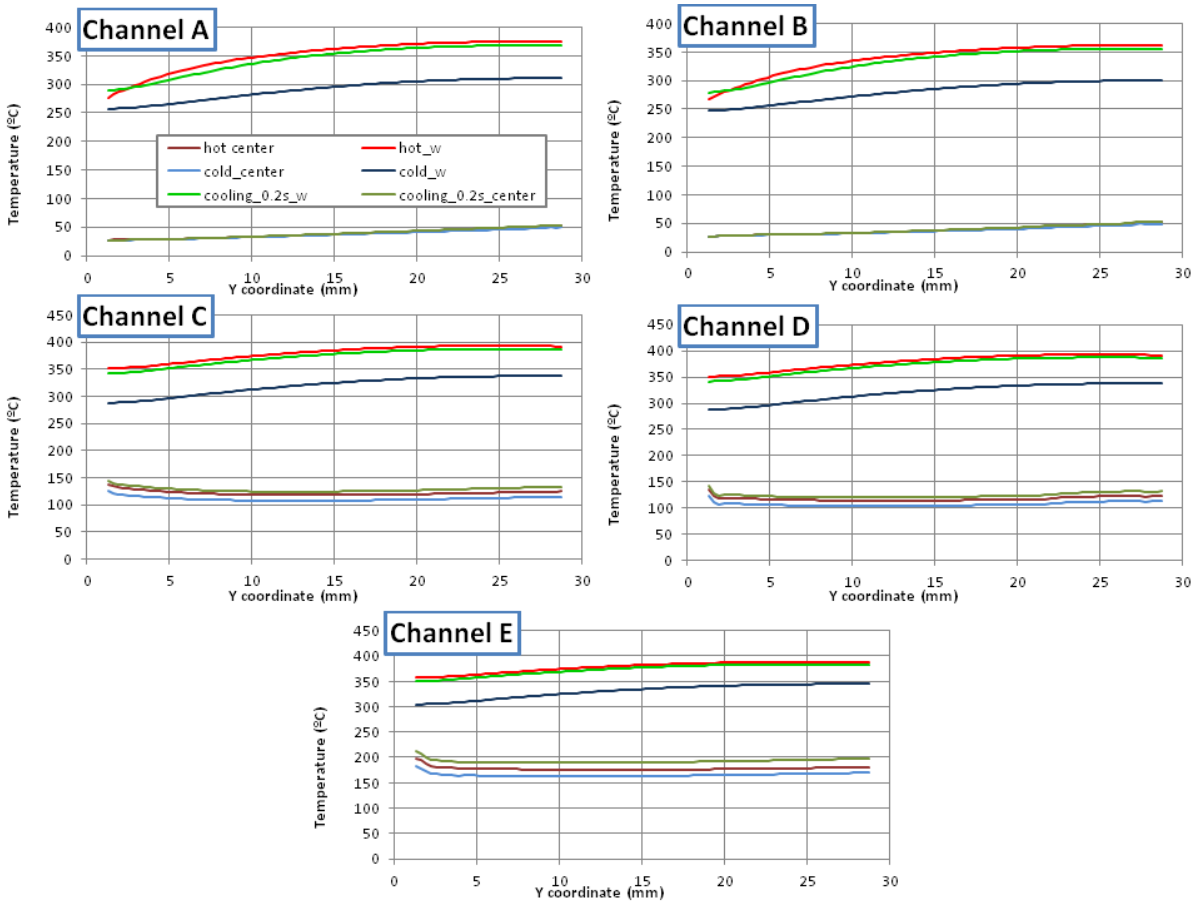

Figure 16: Temperatures of the tungsten wall and helium in the channel center vs channel length (Y) for different instants.

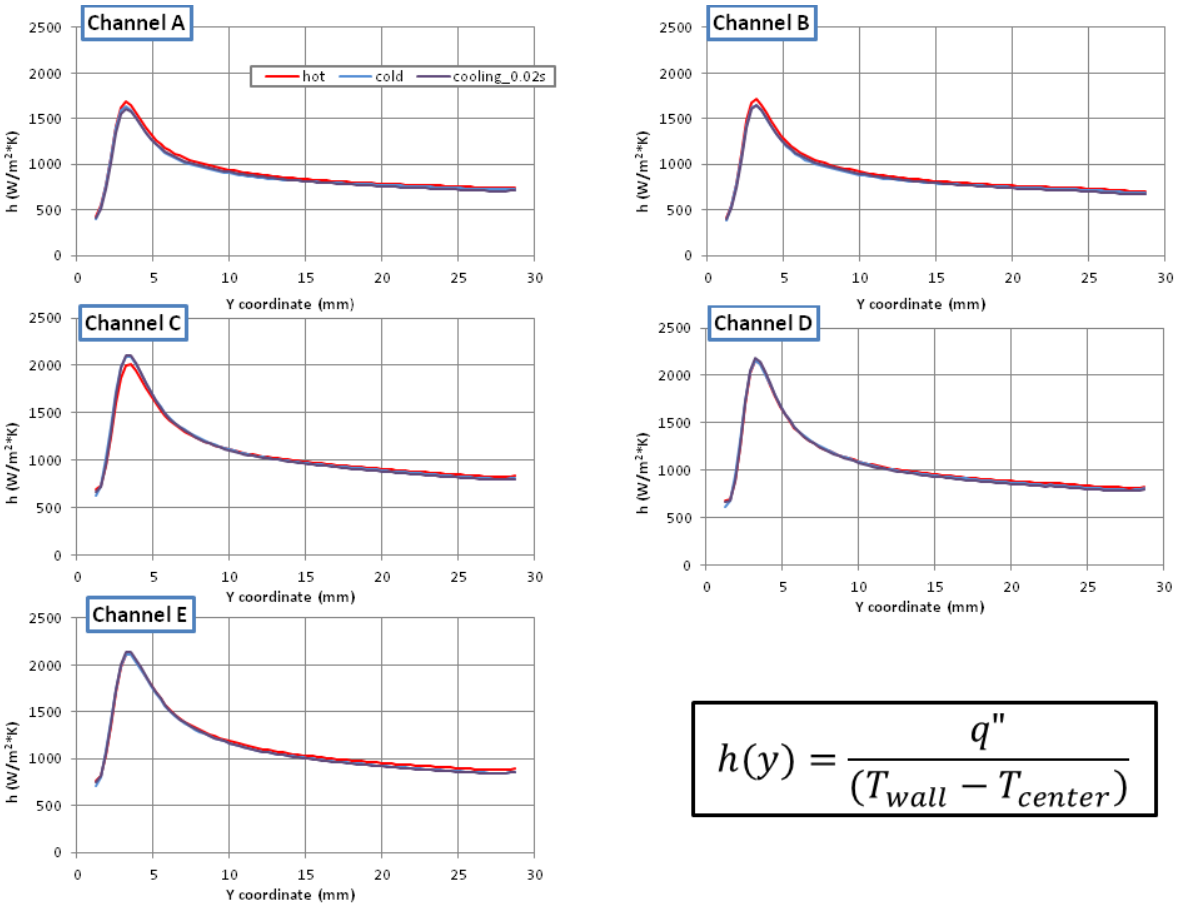

Figure 17: Heat transfer coefficient vs channel length (Y) for different instants.

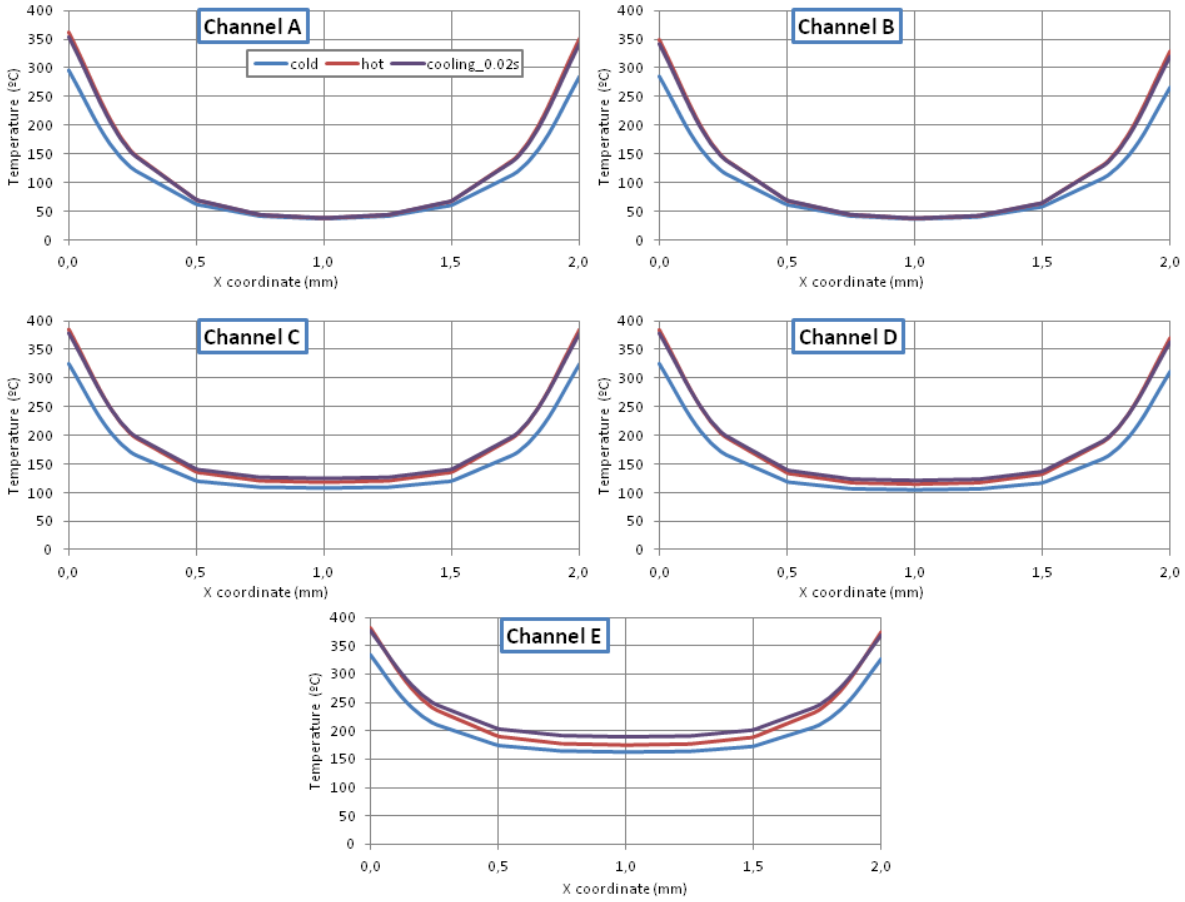

Figure 18: Helium temperature vs channel width (X) at Y=15 mm for different instants.

In order to validate and check the methodology of the cooling convection, BC were obtained for the 2D geometry stated in the study described in the section 7.3.1. After BC were imported to a 2D FEM thermal transient model. The results of the FEM simulation were compared with the ones obtained from a 2D CFD transient model. In Figure 19 is shown a comparison between the thermal profiles obtained by both methods. The temperature results are practically identical, as well as the maximum temperature, but the time and computational resources required to solve the CFD CASE are much higher than those needed to solve the FEM problem.

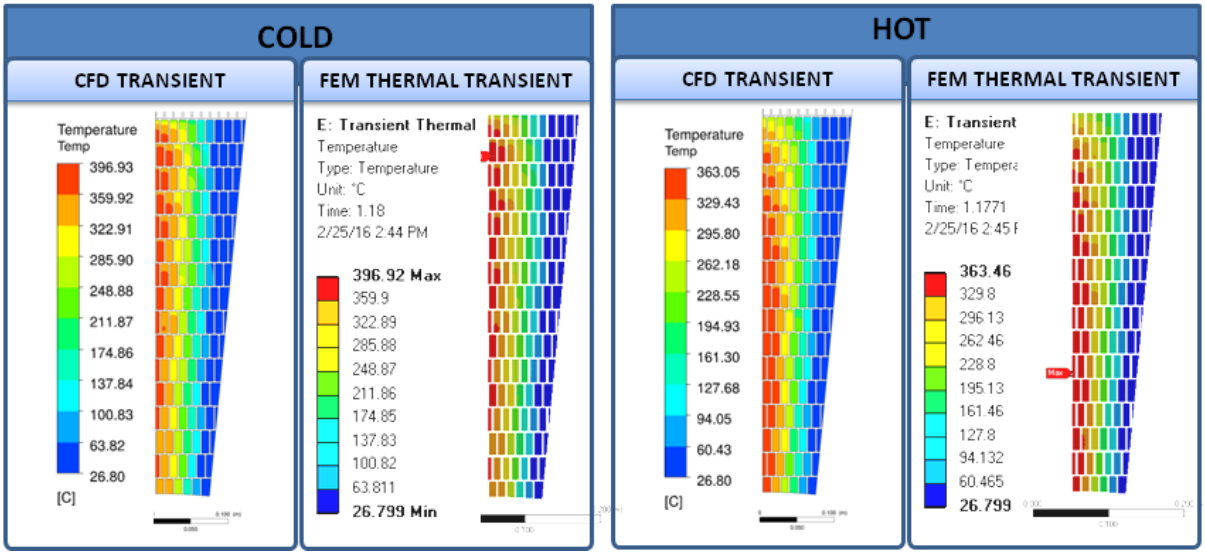

Figure 19: Thermal profile comparison between 2D transient CFD and FEM thermal model before (cold) and after (hot) the proton beam pulse.

7.3.2 CFD-Tungsten convection

In the section 7.3 was concluded that uncoupling the fluid problem from the solid is possible because the heat transfer coefficient and the bulk temperature of the coolant are no time dependent variables. As a consequence, it is possible to obtain a boundary condition (BC) from a CFD steady state simulation, which will be able to reproduce the cooling effect of the helium on the solid walls. The aim of this section is describe the CFD model used to generate the convection boundary condition, that will be used in the complete FEM model, in order to obtain the temperature and stress profiles evolution during a pulse and the subsequent cooling on the tungsten brick and the cassette.
The following boundary conditions and assumptions have been considered to generate the convective cooling boundary condition:

- Steady state thermal source based on Design Beam Footprint[4] is considered, which is valid according section 7.3.
- Helium inlet conditions are: pressure of 10 bars and temperature of 115°C. Coolant massflow is 3 $kg \cdot s^{-1}$ for the whole Target and is equally divided between the 36 sectors. The temperature of the helium inlet has been obtained trough an iterative process using the CFD-FEM model of the spallation (grey zone in figure 20) material described in the sections this section and 7.4 and an additional model that reproduces the helium behaviour in the rest of the Target Wheel and Shaft[17] (blue and red zones in figure 20). In the figure 20 it is shown a scheme with the interface boundaries in red and the interfaces variables used for the iterative calculation. From this iterative process $T_{in} = 95°C$ is obtained as the area average at the interface between both models (Figure 20), in order

to obtain conservative stress and temperature profiles the inlet temperature of the helium was increased in 20°C.

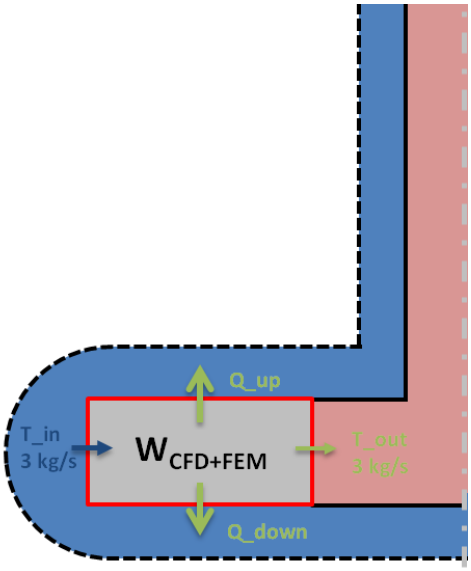

Figure 20: Interface boundaries and variables between CFD sub-models

- The influence of the up and down plates of the cassette is considered negligible so the heat conduction from the tungsten to the cassette plates is avoided. Heat conduction will be allowed in the thermal model (7.4), but for the calculation of the convective cooling boundary the simplification can be assumed.
- Following the assumptions and boundary conditions described above one quarter symmetry can be assumed for the SF1 load conditions, however for the SF2 loads conditions just one half symmetry should be assumed, because the symmetry plane depends on the SF2 load case.

A conformal mesh composed by hexahedral cell elements divided in 4 cell zones was used to solve the CFD problem. The solid zones of the domain are: the turbulence generators, the side wall of the cassette and the tungsten. Due to the main X and Y are the main fluid directions and the small variable gradients in the Z direction, along the Z axis the mesh has one cell per centimeter which is coarser resolution than X and Y axis. However in the X and Y direction the size of the mesh is fine enough to accurately solve the boundary layer and the heat transfer. In the Figure 21 and table details of the mesh are showed.

Parameter	Value
N^o Elements	2,205,420
Orthogonal Quality	0.992
Skewness	0.024

Table 5: Mesh quality for CFD model

The employed model to solve the turbulence in the fluid was the SST $\kappa - \omega$ model which is a two-equation eddy-viscosity model. The use of a $\kappa - \omega$ formulation in the inner parts of the boundary layer makes the model directly usable all the way down to the wall through the viscous sub-layer. The SST formulation also switches to a $\kappa - \epsilon$ behaviour in the free-stream and thereby avoids the common $\kappa - \omega$ problem that the model is too sensitive to the inlet free-stream turbulence properties.

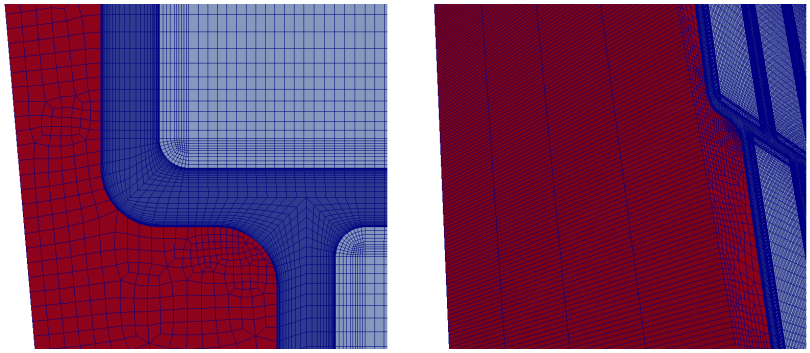

Figure 21: Details of mesh used to generate the convective cooling boundary condition

As it was explained in previous paragraphs, the aim of solving this CFD problem is to obtain a boundary condition, which reproduces the cooling effect of the helium in the wall surfaces of the tungsten. The boundary condition consist on two values associated with each solid wall cell ($\tilde{r}_w$) in contact with the helium:

- $T_{bulk}(\vec{r}_w)$: Bulk temperature is the temperature of helium on a fluid cell separated from the solid a normal distance ÒdÓ, where fluid is outside the thermal boundary layer and temperature can be considered no time dependant, between 0.55 - 0.7 mm.
- $h(\vec{r}_w)$ is the heat transfer coefficient calculated $h(\vec{r}_w) = q"(\vec{r}_w) \cdot (T_{bulk}(\vec{r}_w) - T(\vec{r}_w))^{-1}$

  These values can not be obtained directly from the CFD solution data so a post-processing process is required. It was required to develop a specific computer tool to do the post-processing and generate an input file for the thermal model. The input file contains the X,Y and Z coordinates ($\tilde{r}_w$) of each surface point in contact with the helium and its cooling boundary condition ($T_{bulk}(\vec{r}_w)$, $h(\vec{r}_w)$)

7.4 FEM-Thermal model

As shown in the section 7.3.1 the thermal profile of the cassette and the tungsten bricks can be solved with a FEM thermal solid, where only solids are taken into account and the cooling effect of the helium is reproduced by a convective boundary condition which is no time dependent. The aim of this section is to describe the thermal transient FEM model used to calculate the temperature evolution during the proton pulse and the subsequent cooling. The results of the simulations performed with this model are presented in the section 10.1 .

The following boundary conditions and assumptions have been considered to solve the thermal transient problem:

- The employed heat source is based on the Design Beam Footprint (REF). The heat source is activated in the simulation during the pulse ($t_{pulse} = 2.86 \cdot 10^{-3}$ ms) and disabled during the cooling ($t_{cooling} = 2.56857$ s).
- On the faces of the tungsten bricks, the turbulence generators an the side wall of the cassette, which are in contact with the helium, it has been applied the convection boundary condition that was described in the section 7.3. For the cassette this convection boundary condition was applied only on the internal face of the side wall.
- The heat transfer between internal plates faces to the helium is not considered, which is a conservative approach.
- It was defined a convection boundary condition to consider the cooling effect of the helium on the inlet channel of the cassette plates. The increase of temperature of the helium flowing trough these channels is considered linear and was obtained from the CFD sub-model that reproduces the helium behaviour in the rest of the Target Wheel and Shaft (blue and red zones in figure 20), in the figure 22. To obtain the heat transfer coefficient the Dittus-Boelter [19] equation was used:

$$Nu_D = 0.023 \cdot Re_D^{0.8} \cdot Pr^{0.4} \text{ [19]}$$

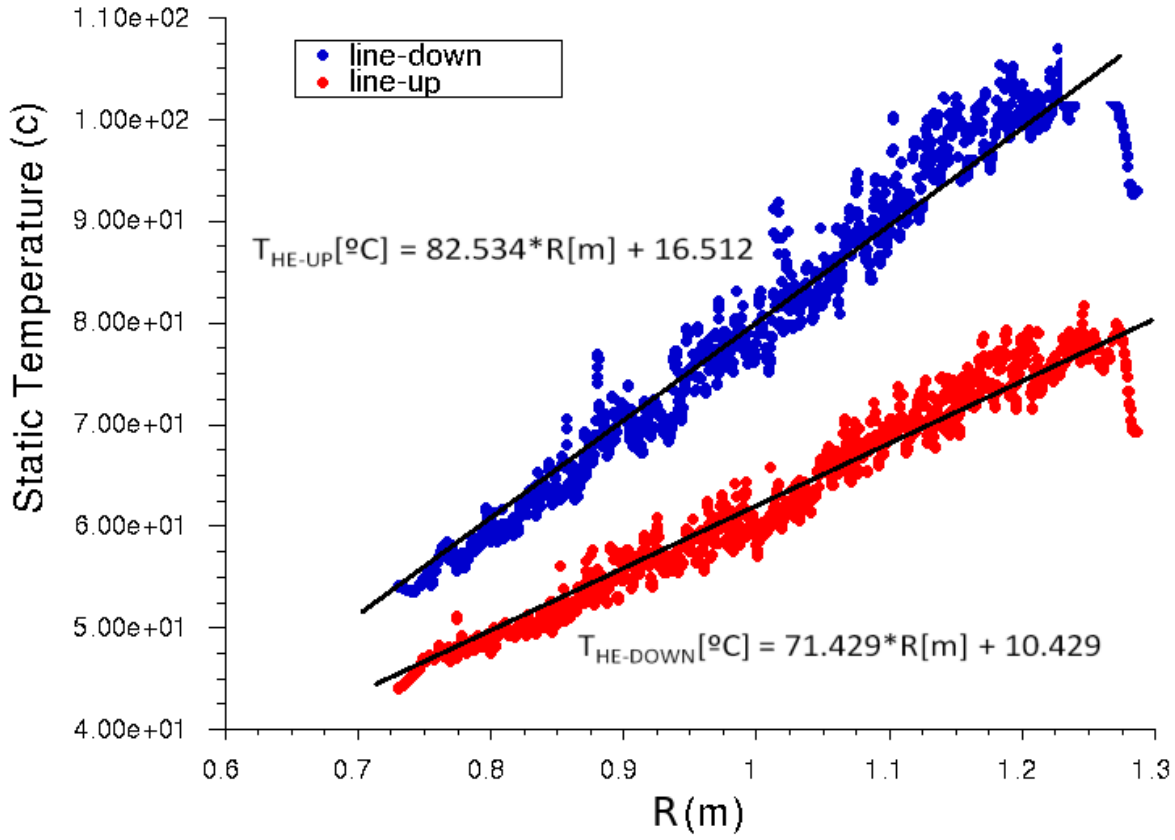

Figure 22: Helium bulk temperature in the inlet up and down cassette channels

- Between the tungsten bricks and the cassette is assumed a perfect thermal contact.
- All other surfaces are considered adiabatic
- One half symmetry is considered, YZ is the symmetry plane.

Unlike the CFD problem the required mesh to accurately solve the thermo-mechanical problem is coarser. A non conformal mesh composed by 466,000 elements was employed, most are hexahedrons but some complex bodies were meshed with tetrahedrons (Figure 24).

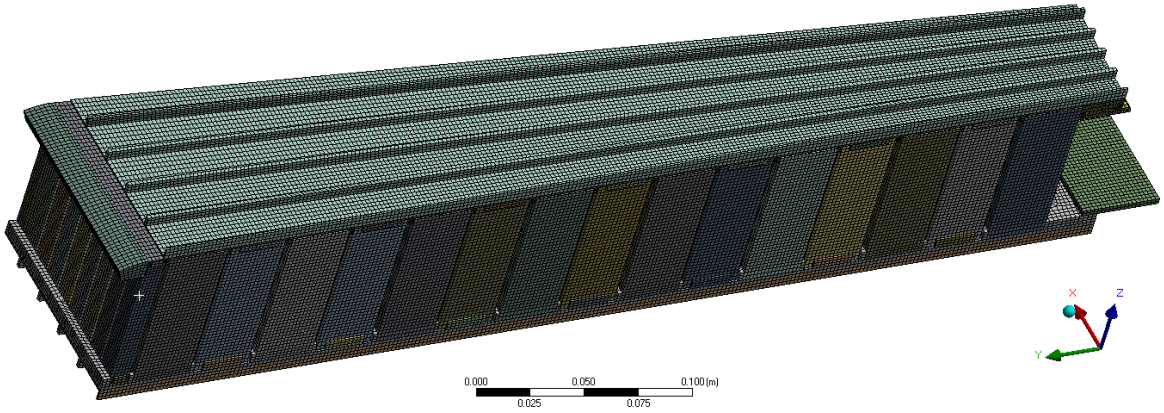

Figure 23: Mesh used to solve the FEM thermal problem of the spallation material and cassette

7.5 FEM-thermal model for shut-down analysis

The shutdown scenario describe on section 10.7 considers a case in which the beam is off shut-down and the coolant flow is interrupted. In this conditions the residual heat have to be evacuated by means of conduction between bodies and thermal radiation. Obviously, the helium inside the target establishes convection between tungsten bricks, however, the small size of the gaps in between bricks will reduce its effect. Based on that, we propose a conservative scenario in with there is only heat transmission between solid bodies.

The FEM consider is based on the FEM-Thermal model shown on Section 7.4 in which we have include two stainless steel plates connected to the cassette ribs. The bottom plate is bounded to the cassette taking into account that gravity will guaranty a good thermal contact. In the cassette of the connection which the top plate a thermal resistance equivalent to 1 mm helium gab is included.

Regarding the heat generation profile, only spallation material is considered as decay heat source. A detail description of the evaluation process is shown on Section 8. Finally, the vessel removes the heat by radiation on its external surfaces to a black body at room temperature.

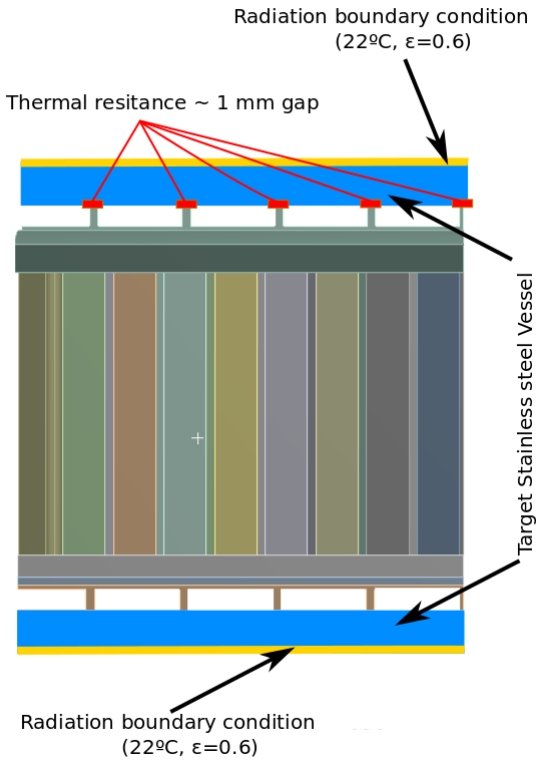

Figure 24: Thermal resistances and boundary conditions for the shutdown case

7.6 FEM-Mechanical model

The temperature distributions evaluated by means of the FEM-Thermal model(See section 7.4) are considered as thermal loads for the mechanical analysis. This section is described the mechanical model to calculate the stress profile evolution in the spallation material.

The following boundary conditions are included in the mechanical model:

- The load considered for the calculation is only the temperature distribution produced by heat source generated by the proton beam interaction with the tungsten. Two temperature profiles have been imported from the thermal transient model described in the section 7.4, at the end of the cooling and at the end of the protons beam pulse. Both instants correspond respectively to the minimum and maximum temperature of the system, which conducts to the minimum and maximum stress on the spallation material.
- The mechanical boundary conditions on the spallation material have been set to reproduce the supports of tungsten bricks on the cassette, avoiding the simulation of the cassette. The tungsten bricks are held by the cassette plates but having certain space/gap to expand. In the Figure 25 are detailed the following boundary conditions for the support:
  - **A:** No displacement is allowed for these points.
  - **B:** No displacement is allowed along Y and Z direction, but X displacement is free for these points.
  - **C:** No displacement is allowed along Z, but X and Y displacement is free for these points.
  - **D:** YZ is a symmetry plane which slices some tungsten bricks. The symmetry condition is considered applying a frictionless support to the sliced faces.

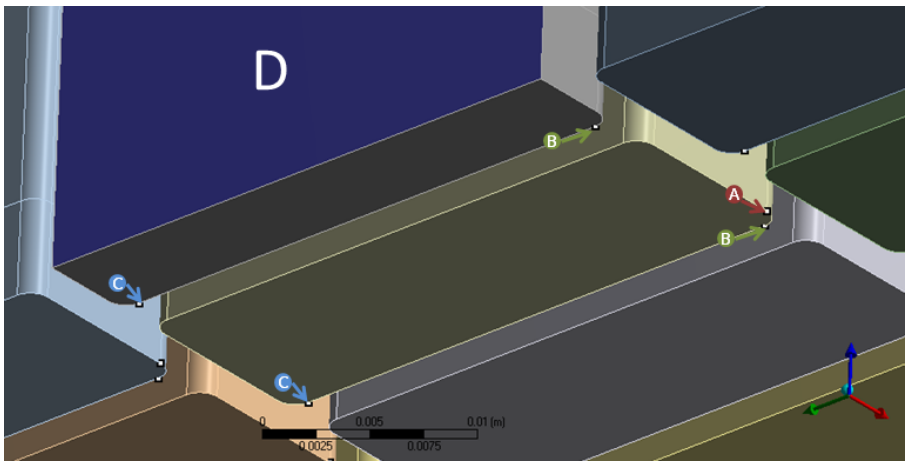

Figure 25: Support boundary conditions used to solve mechanical problem of the spallation material

Regarding the mesh, a non conformal mesh composed by 321,200 hexahedral elements was employed.

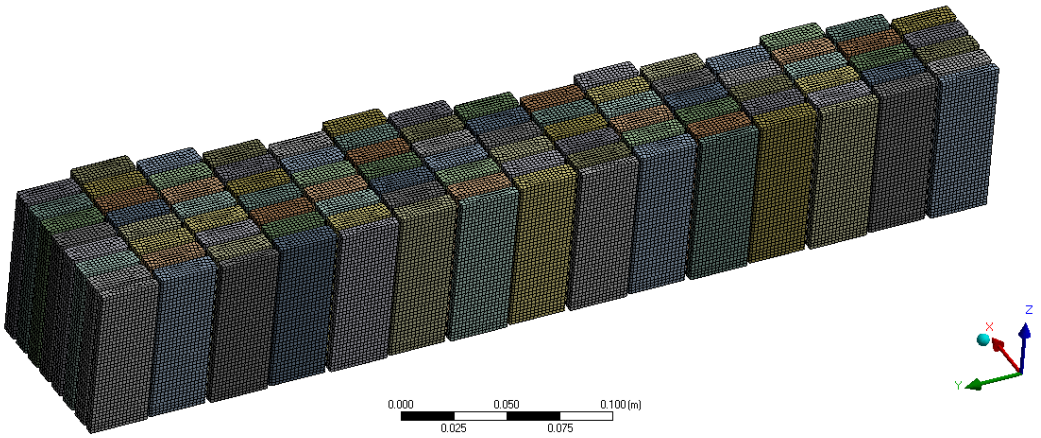

Figure 26: Mesh used to solve mechanical problem of the spallation material

8 Residual heat and inventory

The residual heat analysis uses the parameters described in the Table 6. The results explain the spatial distribution of the after heat produced by 25000 *hours* of irradiation. Moreover, the main isotopes that contribute to the residual heat have been identified.

	Parameters
Mean beam intensity	2.5 mA
Mean proton energy	2 GeV
Power proton beam	5 MW
Irradiation period	25000 h

Table 6: Simulation conditions for the residual heat analysis.

8.1 Residual heat results

The contribution of the spallation residuals to the total residual heat is very important. For that reason, the heat footprint generated in the tungsten by the proton beam has been analysed in detail.

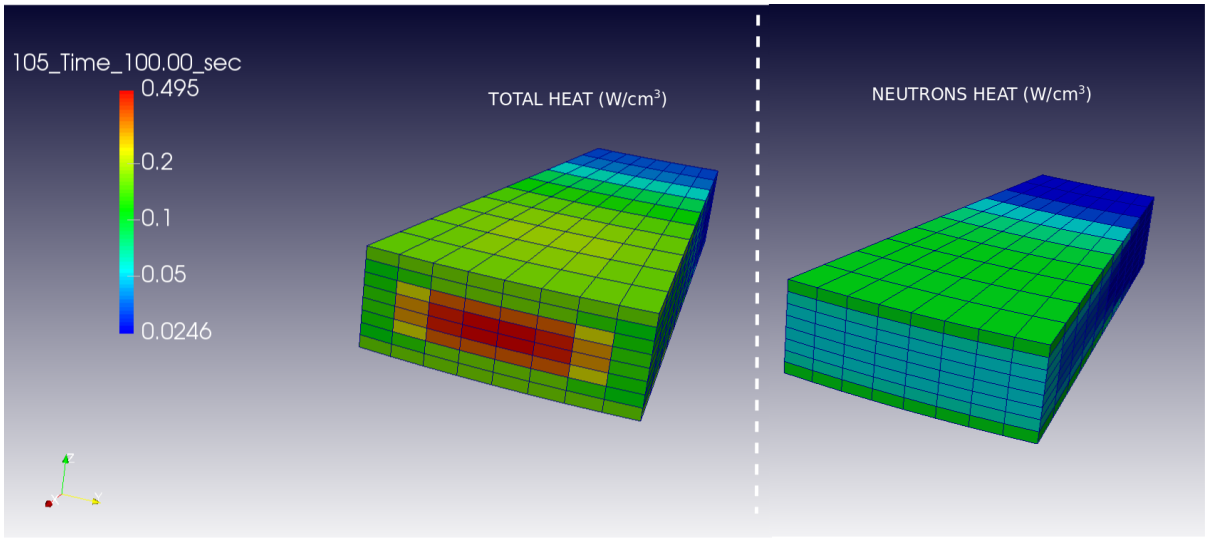

Figure 27: Residual heat distribution comparing the importance of the neutron flux (right) with the total heat (left).

The neutron captures also generate important heat, but this heat is lower than the generated

by the spallation residuals. The Figure 27 represents the comparison between the results of the total residual heat and the generated by neutron flux. The heat peak produced by the proton beam footprint is clearly remarked by this analysis.

The decay evolution is also affected for this separation of the results. The Figure 28 shows the decay evolution of the residual heat, comparing the total heat with the generated by neutron flux.

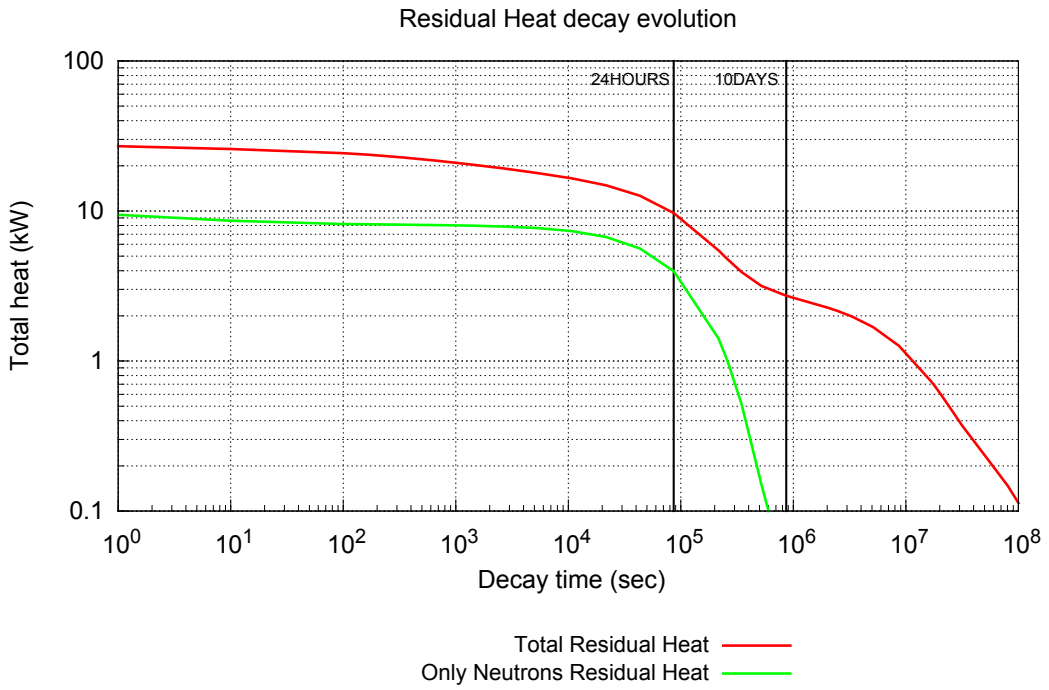

Figure 28: Residual heat evolution comparing the total with the generated by neutron flux only.

The Table 7 represents some most relevant elements of the time decays. During the first 24 hours, the spallation residuals represent the 60% of the total heat. Then, its importance grows until the 99% when 10 days has passed.

The Figure 29 shows the difference between the simulations with angular division and without angular divisions (homogeneous distribution). The maximum peak in W/cm^3 disappears in the homogeneous calculation, distributing the heat around the target thickness. The total heat power is similar in the two simulations, but the heat peak is closer to real situation, when the angular division is taking into account.

Decay time	Total Heat	Neutrons heat	Spallation residuals
100 secs	24.2 kW	8.1 kW	57 %
24 hours	9.7 kW	3.9 kW	60 %
10 days	2.7 kW	0.036 kW	99 %

Table 7: Residual heat division between spallation products and neutron flux, compared in different time decays (100 secs, 24 hours and 10 days).

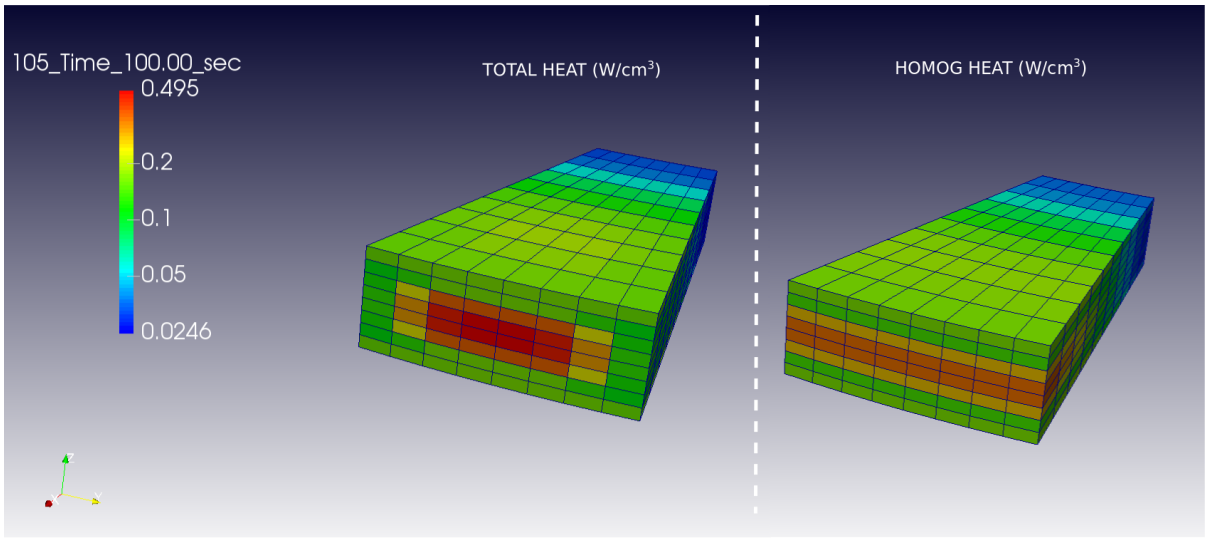

Figure 29: Residual heat distribution comparing the importance of angular divisions (left) with homogeneous calculations (right).

The volumetric residual heat decreases with the time decay. It passes from a peak of 0.5 W/cm^3 at 100 secs after shutdown to a peak of 0.05 W/cm^3 after 10 days or 0.005 W/cm^3 after 2 years. The Figures 30 and 31 show the residual heat distribution at different time decays.

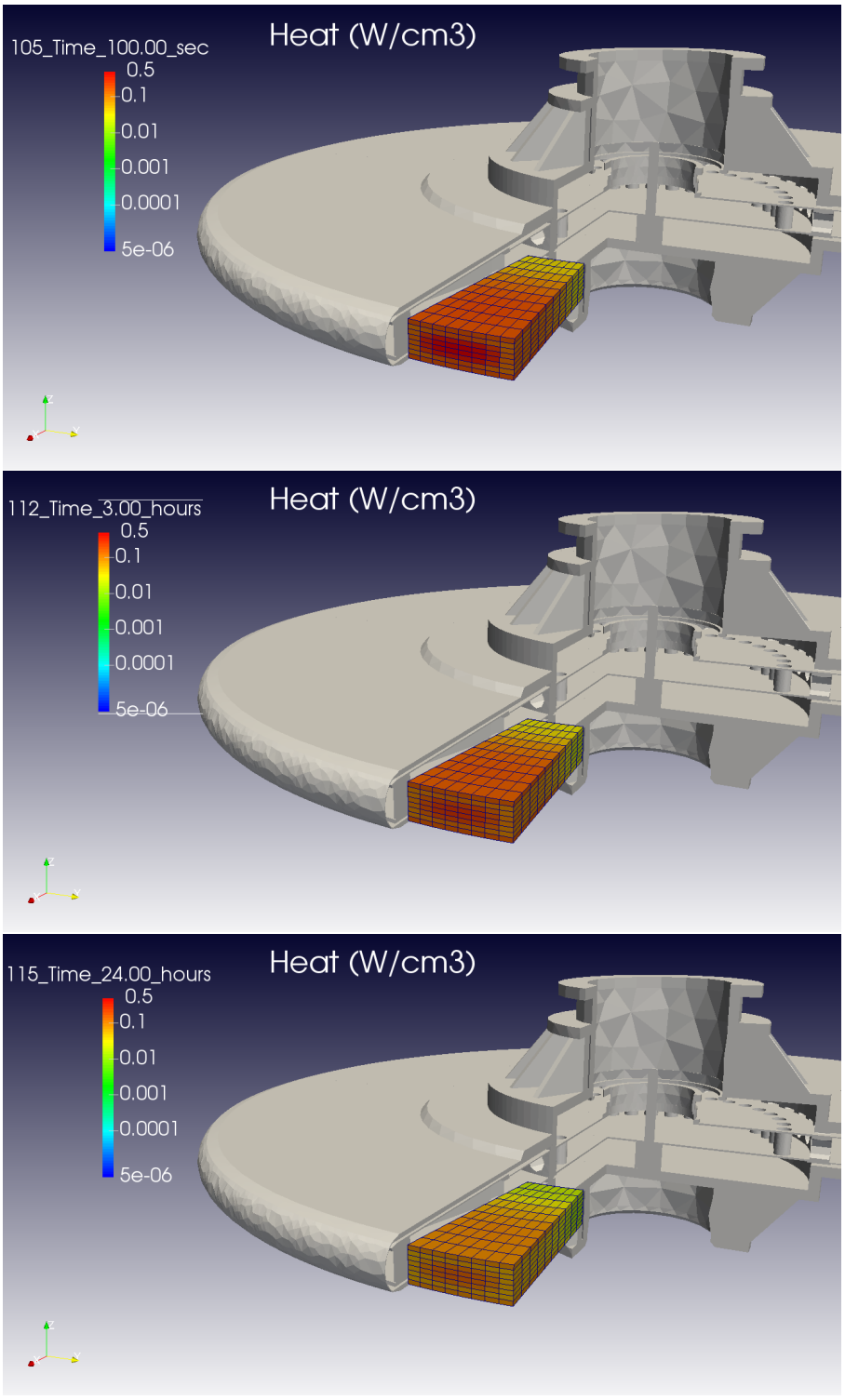

Figure 30: Residual heat distribution through the target cells after 100 secs, 3 hours and 24 hours of decay.

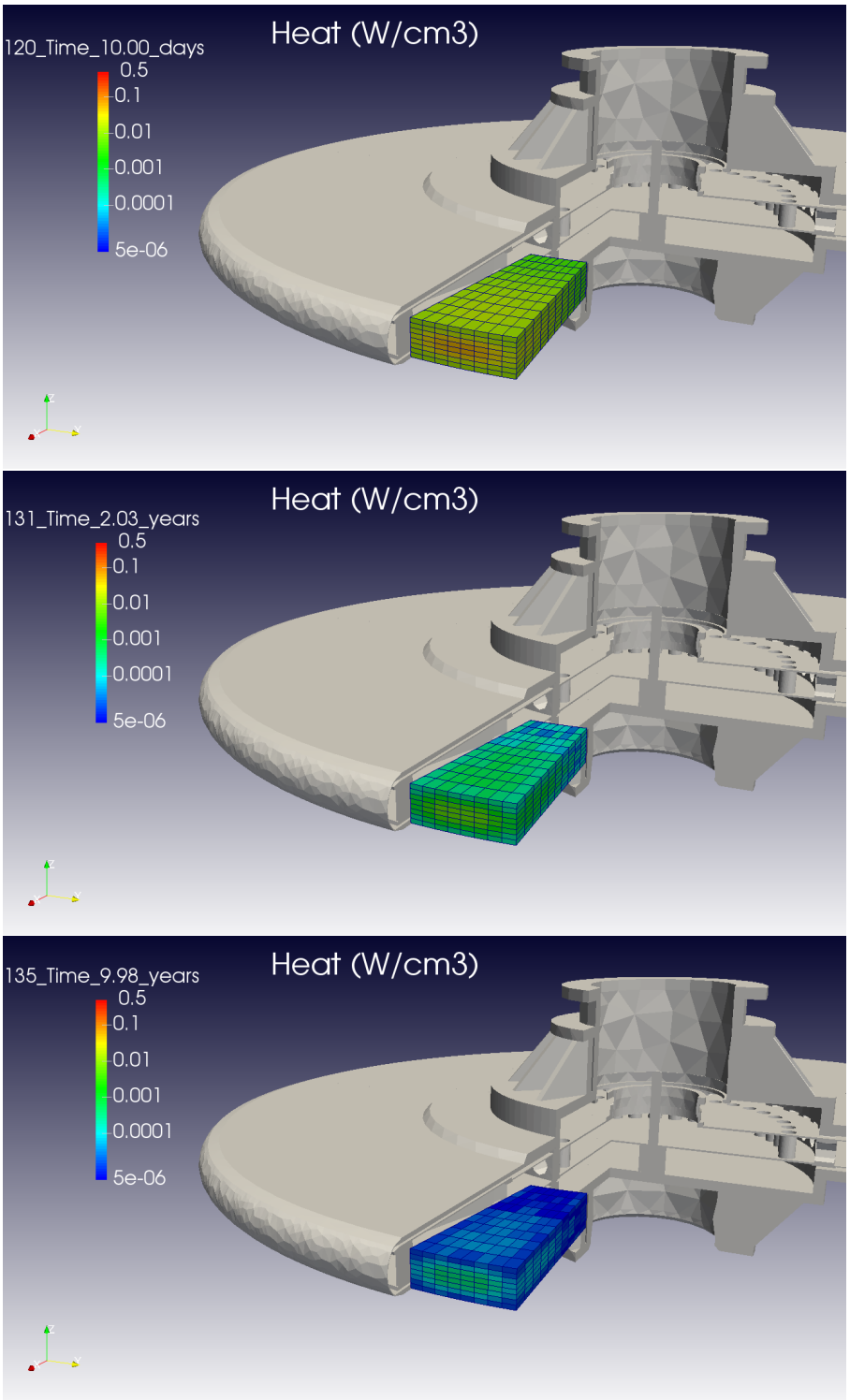

Figure 31: Residual heat distribution through the target cells after 10 days, 2 years and 10 years of decay.

The radial distribution indicates a maximum residual heat on the external annulus. It is generated for the impact of the protons in the first layers of the tungsten. While the protons are slowed, the generation of spallation products decreases, producing less residual heat in the internal annulus of the target.

Moreover, the high capture cross section of tungsten reduces the neutron flux in the center of the wheel and due to that, the residual heat produced by activation is lower in the center.

The vertical distribution reveals a peak in the center of the target height. That maximum corresponds with the proton footprint in the tungsten, that generates the major contribution of the spallation products on this area. Moreover, there is another heat increment in the vertical direction.

This new increase is caused by a higher neutron flux on this area. The higher neutron flux comes from the rebounds of the neutrons on the reflector, increasing the neutron captures in the tungsten. The higher number of neutron flux with medium and high energy contributes in major measure to the residual heat on the external area of the target.

After shutdown, the total heat reaches $27,2$ kW to decrease quickly in the first 100 secs to 24.2 kW. Then, it decreases to 9.7 kW and 2.7 kW at 24 hours and 10 days, respectively.

8.2 Inventory

The main isotopes that contribute in the residual heat are shown in the Figures 32, 33 and 34. These plots reveals the dominant isotopes at shutdown, 24 hours and 10 days of decay, respectively.

At shutdown, ^{187}W, ^{185}W, ^{183M}W and ^{176}Ta contribute the most. The metastable ^{183M}W ($T_{1/2} = 5.2s$) decays in the first 100 sec and then its contribution is negligible.

After 24 hours of decay, isotopes ^{187}W, ^{185}W still being the dominant constituents followed by the heat produced by ^{170}Lu and ^{172}Lu.

Finally, at 10 days of decay, the contribution of ^{187}W is lower than in other decay periods. The main isotopes at this decay time are ^{185}W, ^{172}Lu and ^{182}Ta.

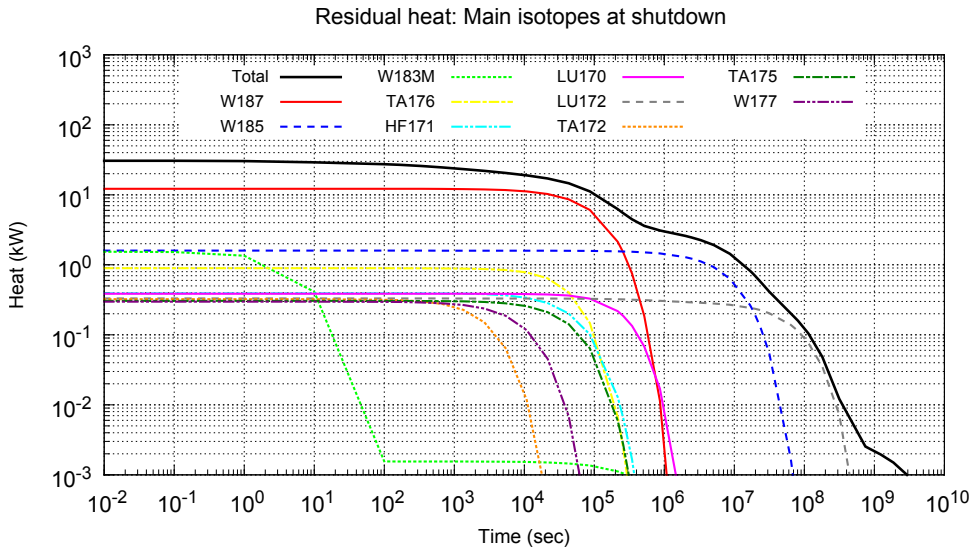

Figure 32: Main isotopes at shutdown. Decay heat as a function of the decay time: dominant constituents after 25000 hours of irradiation.

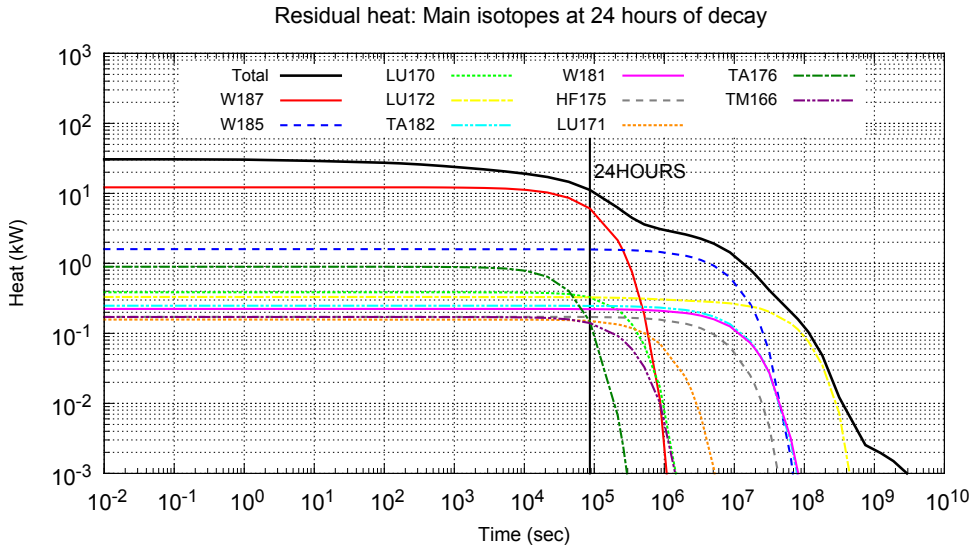

Figure 33: Main isotopes at 24 hours of decay. Decay heat as a function of the decay time: dominant constituents after 25000 hours of irradiation.

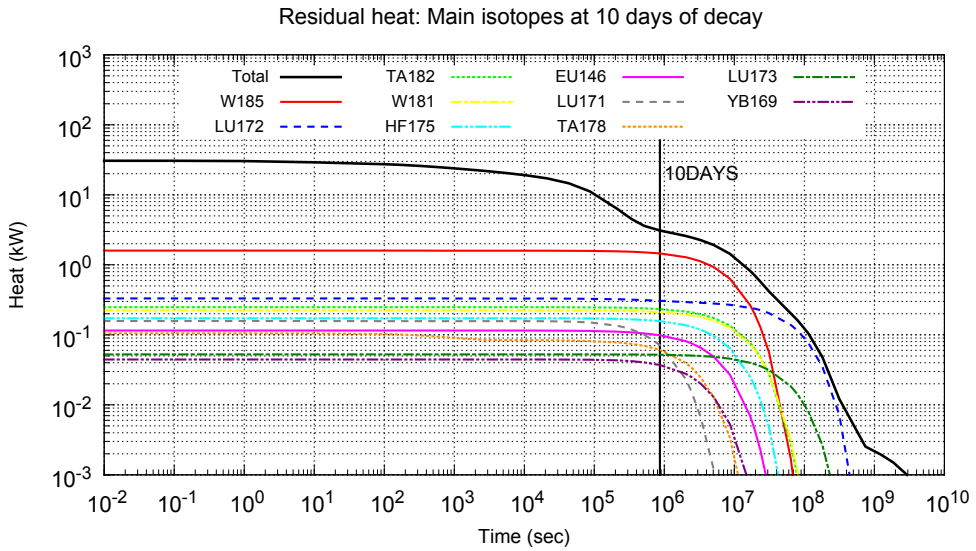

Figure 34: Main isotopes at 10 days of decay. Decay heat as a function of the decay time: dominant constituents after 25000 hours of irradiation.

8.3 Conclusions

The main conclusions about the residual heat analysis of the target are described bellow:

- A multicell analysis allows to evaluate the spatial distribution of the heat and to implement the results to the accidental scenarios. The residual heat distribution has a maximum on the external annulus of the target and on the center of its height.
- The spallation residuals are important compared with the activation by neutron flux (more than 60% of the total heat) . For that reason, the heat footprint created by the proton beam has been analysed.
- The total residual heat after shutdown reaches 27.2 kW and 3 hours later this value is 16.5 kW. The main contributors to the activity and the residual heat are the ^{187}W and ^{185}W.

9 Irradiation damage conditions

As it was mentioned in the introduction, the ESS Target will use tungsten as spallation material. This element is well known to became brittle with relative very small values of irradiation damage [9], so the evaluation of the irradiation conditions during operation is essential for the target design. However, tungsten is not an structural material in the wheel, hence, its failure is not associated with a loss in the pressure confinement barriers of the system.

The damage in the tungsten has two clear components: in one hand we have protons from the beam, which produced the spallation reactions. The proton beam will hit each sector every 36 pulses, so the total damage is distributed in all the elements of the wheel. In order to evaluate the worst conditions from the irradiation point of view, we have assumed a perfect synchronization between the beam and the rotation of the wheel, in that conditions, the maximum proton beam current is always in the same position. The detail description of the damage analysis process is shown on document ESS-0037287[16].

Figures 35, 36 and 37 shows the dpa, hydrogen and helium produced on the spallation material by neutrons and protons on nominal beam conditions (SF1) and 5000 h of operation.

After 5 years of full power operation, the spallation material will accumulate 12.5 dpa and 2500 appm of helium. Based on the ESS Material Handbook [5] we should expect a 0.22% increase of volume due to swelling, which is not a significant geometrical effect for the tungsten configuration. Regarding the damage, we should expect to have a completely brittle material after only a few months of operation.

This irradiation conditions has been considered to set the material operation limits 3 and due to this conditions the acceptable stresses are far below the nominal limits under non irradiated conditions.

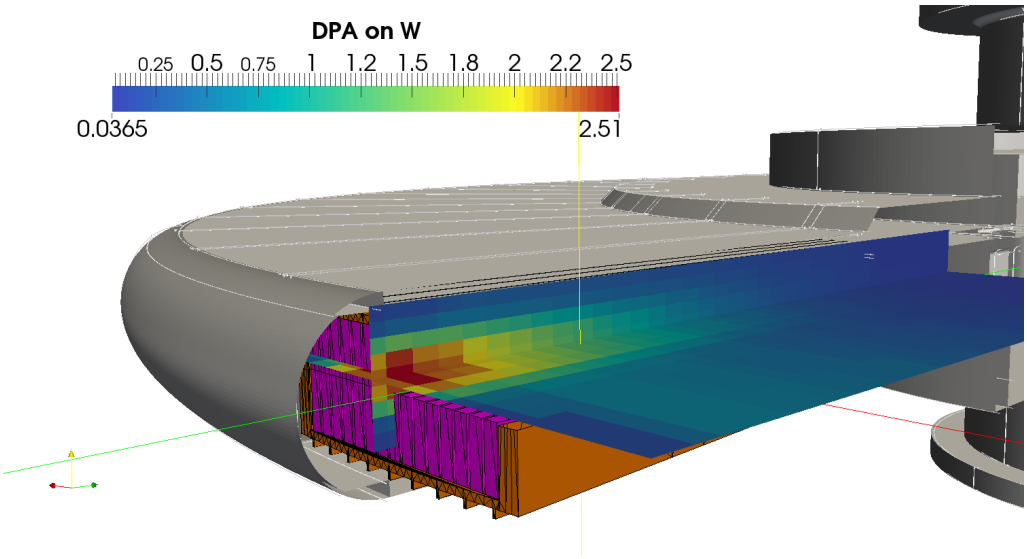

Figure 35: Proton induced damage (DPA) in the spallation material for 5000 h full power operation on nominal beam conditions (SF1)

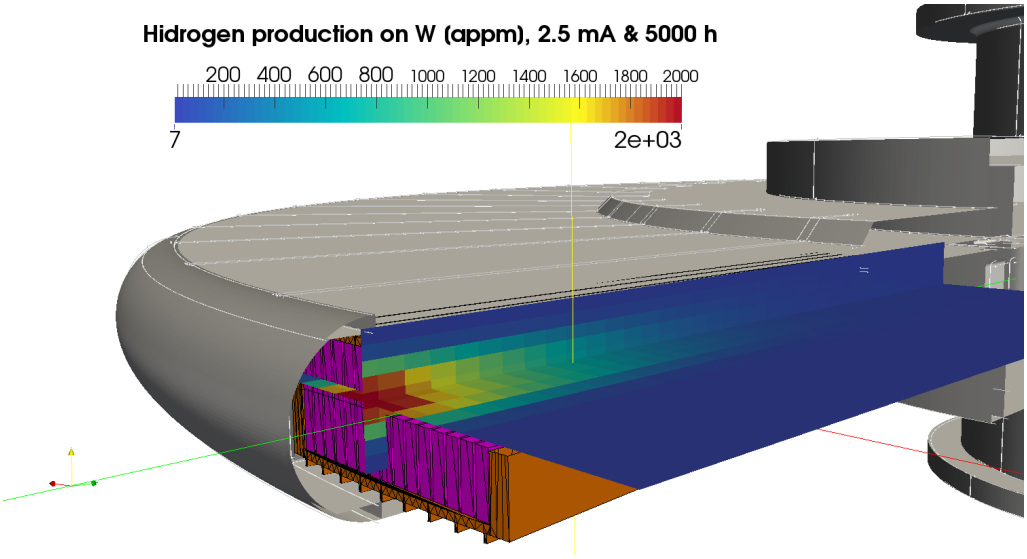

Figure 36: Hydrogen production by protons in the spallation material for 5000 h full power operation on nominal beam conditions (SF1)

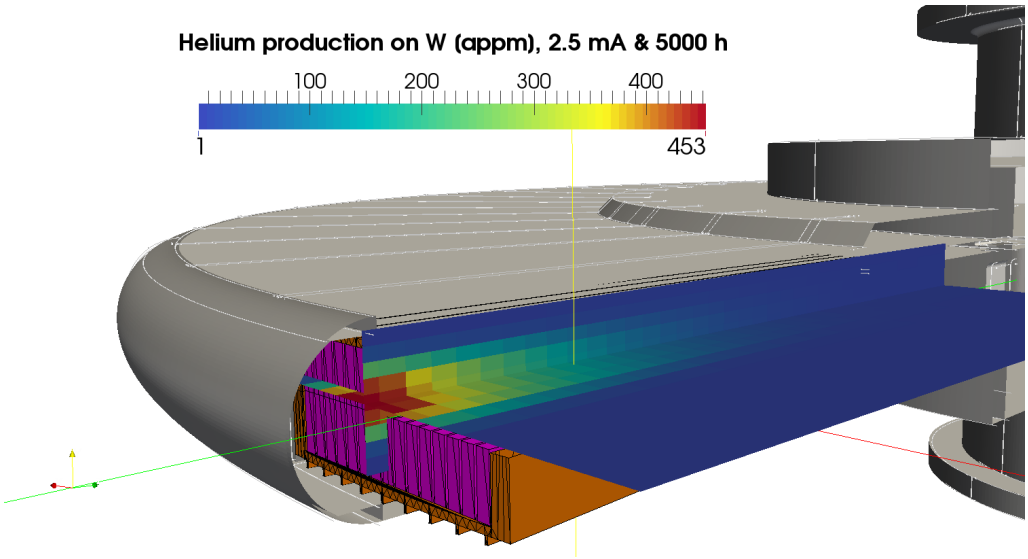

Figure 37: Helium production by protons in the spallation material for 5000 h full power operation on nominal beam conditions (SF1)

10 Load scenarios thermomechanical analysis

10.1 SF1: Normal operational conditions

Based on the description shown on Section 2, loads on nominal conditions are produced by the design beam under nominal frequency for the repetition rate, with the wheel at his nominal rotation speed. Also the beam is considered synchronized with the wheel and hitting in the center of the cassette. The cooling system is working at nominal conditions, so helium mass flow trough the wheel is 3.0 kg/s which means 0.0833 kg/s in each cassette. Figures 38 and 39 shows the beam on nominal conditions. Design beam includes the uncertainty on beam instrumentation, which means 20% more concentrated beam than nominal one.Table 8 shows the main beam parameters.

Parameter	Units	Value
Beam Energy	GeV	2.0
Maximum Beam Energy	GeV	2.2
Pulse Repetition Rate	Hz	14
Beam energy per pulse	kJ	357
Maximum Energy per pulse	kJ	371

Table 8: Main beam parameters[4]

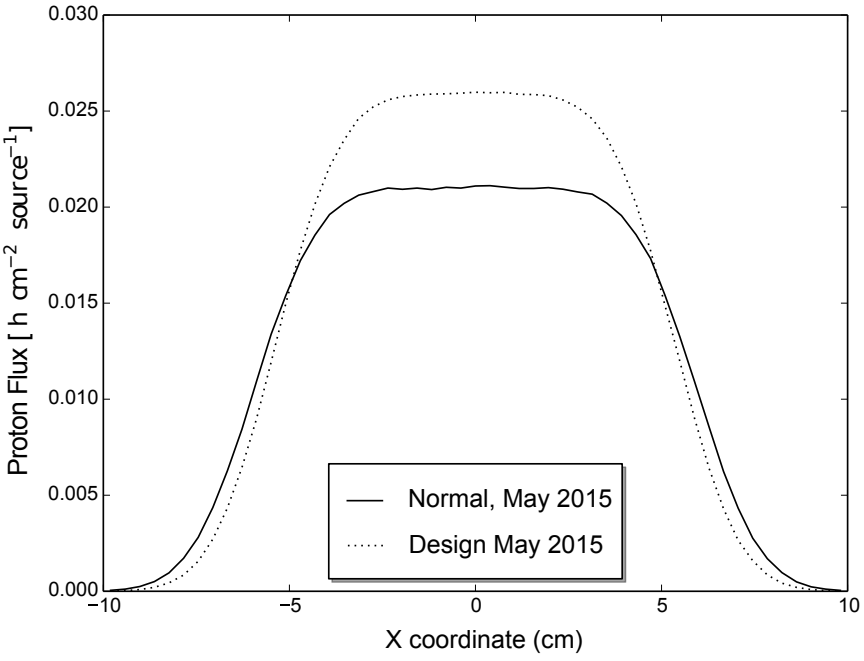

Figure 38: Nominal Beam and design beam[4]. Profile on longer dimension.

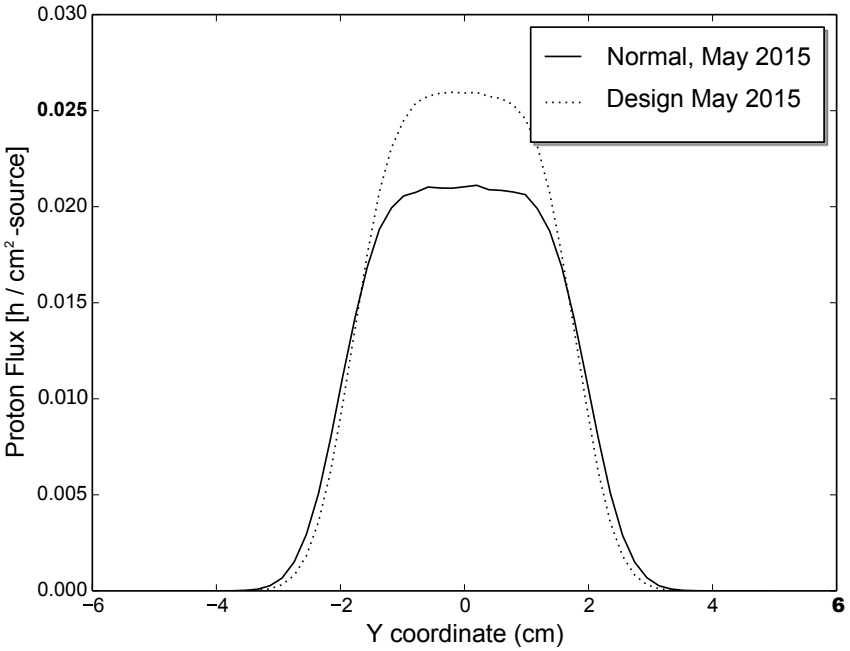

Figure 39: Nominal Beam and design beam[4]. Profile on shorter dimension

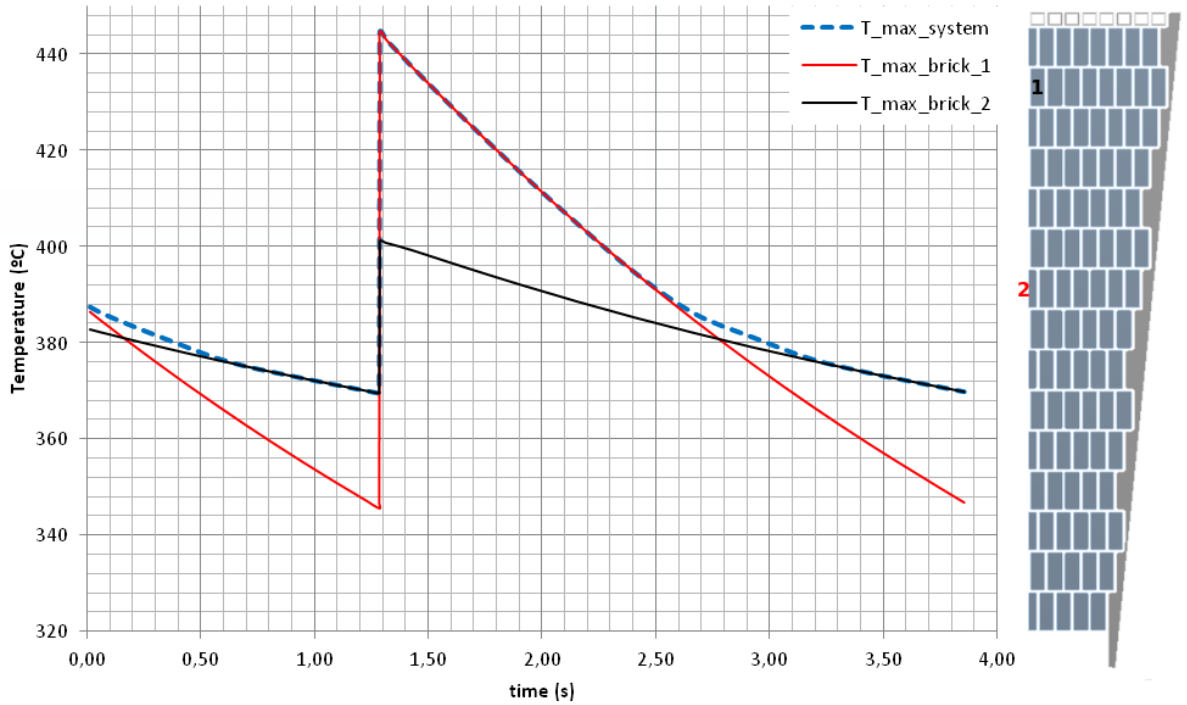

Figure 40: Time evolution of Maximum temperature for the system and two tungsten bricks

The temperature and stress profile evolution of the spallation material during normal operation (SF1 and SF2) are presented in the next figures. The solution has been obtained following the methodology described in the section 7, which means solve the described CFD and FEM models.

In the Figure 40 the time evolution of the maximum temperature of the whole system was represented. The maximum temperature increase happens when the beam hits the tungsten, the energy deposition of the protons interacting the spallation material produces a ΔT of 75 degrees, which occurs in the brick 1 (Figure 40). The front rows bricks have higher heat deposition by protons but they are better cooled, for this reason at the end of the cooling the temperature of front these bricks is lower than others. The brick 2 (40) has the maximum temperature at the end of the cooling cycle.

In the Figures 41 and 42 is shown, respectively, the temperature profile of the spallation material at the end of the cooling and at the end of a protons beam pulse. The maximum temperature at the end of the cooling is 370^{o}C and after the pulse is 445^{o}C, but as is shown in Figure 40 the hottest brick changes during the pulse and subsequent cooling process.

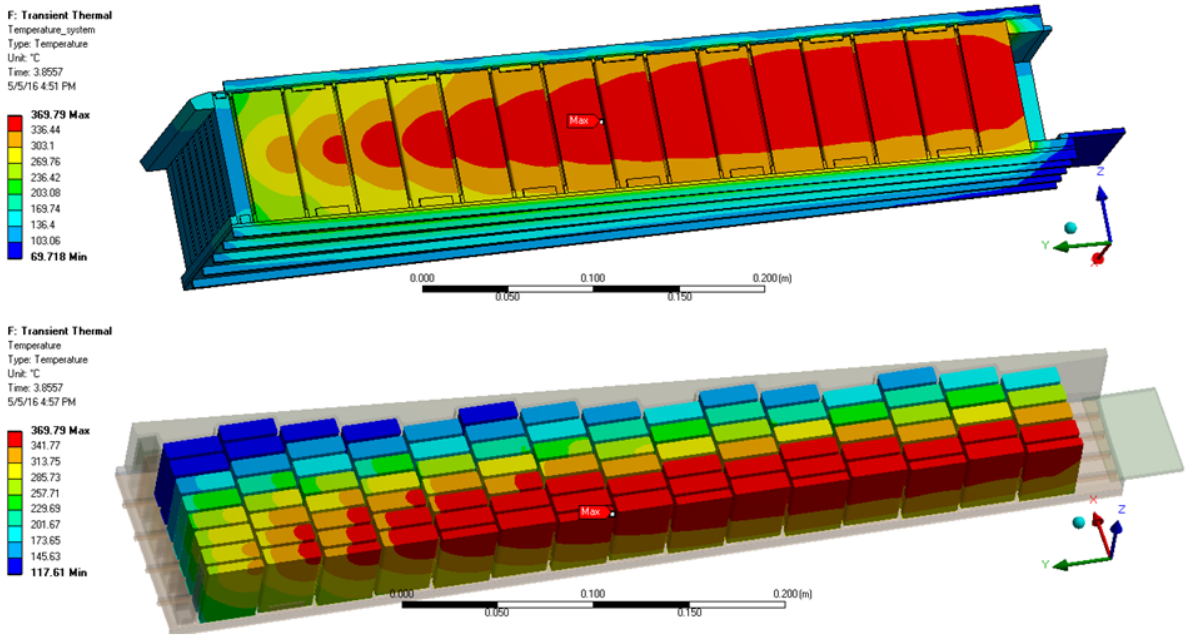

Figure 41: Temperature profile of the tungsten at the end of the cooling

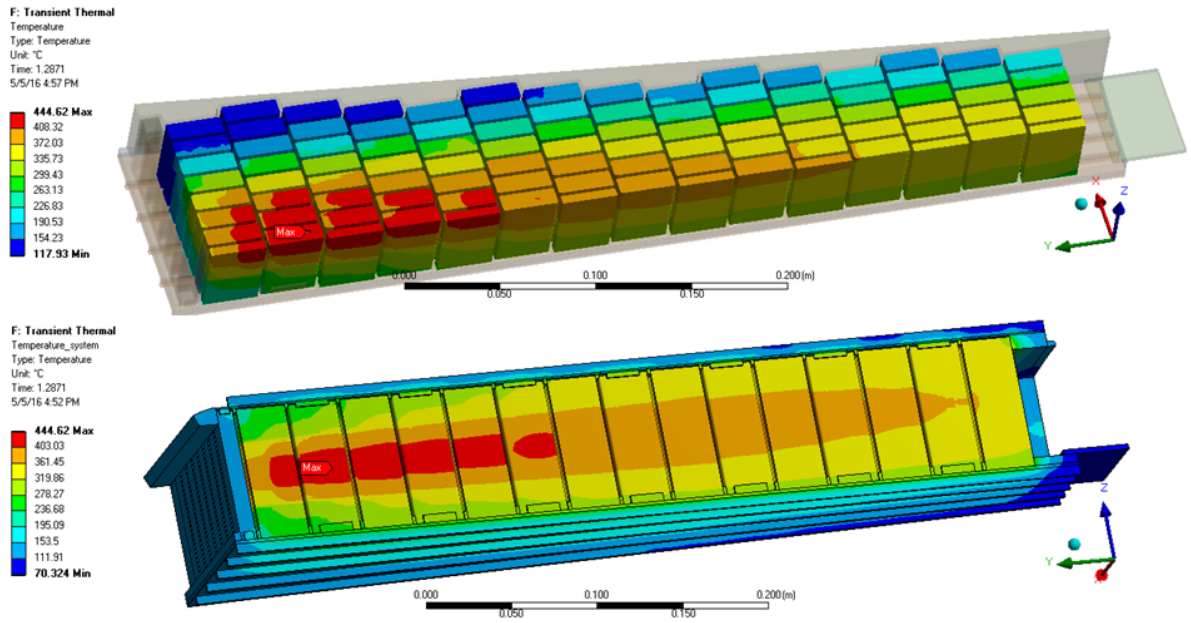

Figure 42: Temperature profile of the tungsten at the end of the pulse

In the Figures 43 and 44 it is shown respectively the von-Mises equivalent stress profile of the spallation material at the end of the cooling and at the end of a proton beam pulse. The maximum stress at the end of the cooling is 44 MPa and after the pulse is 110 MPa.

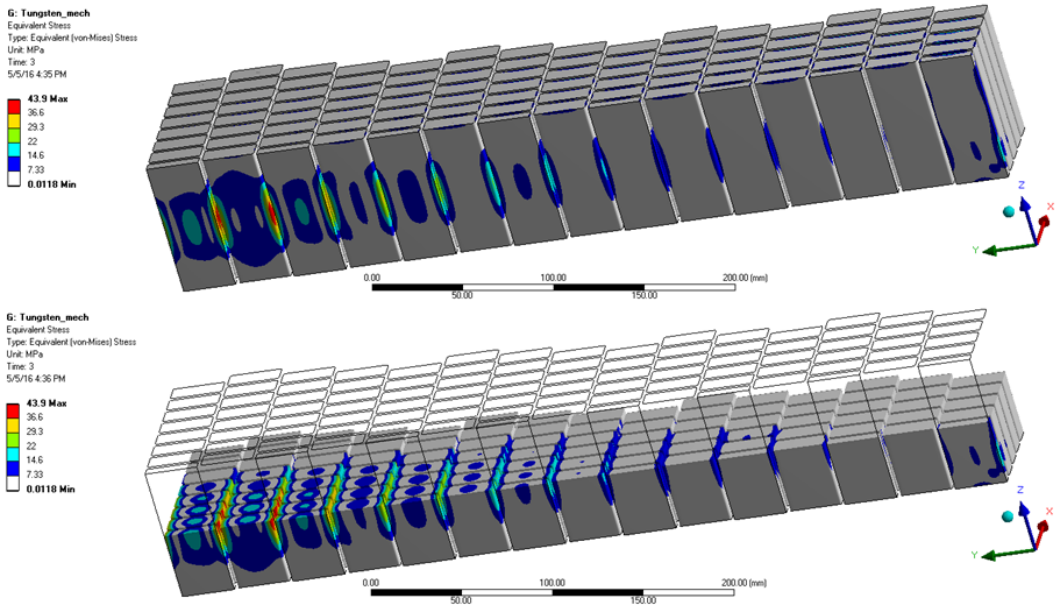

Figure 43: Von-Mises equivalent stress profile of the tungsten at the end of the cooling

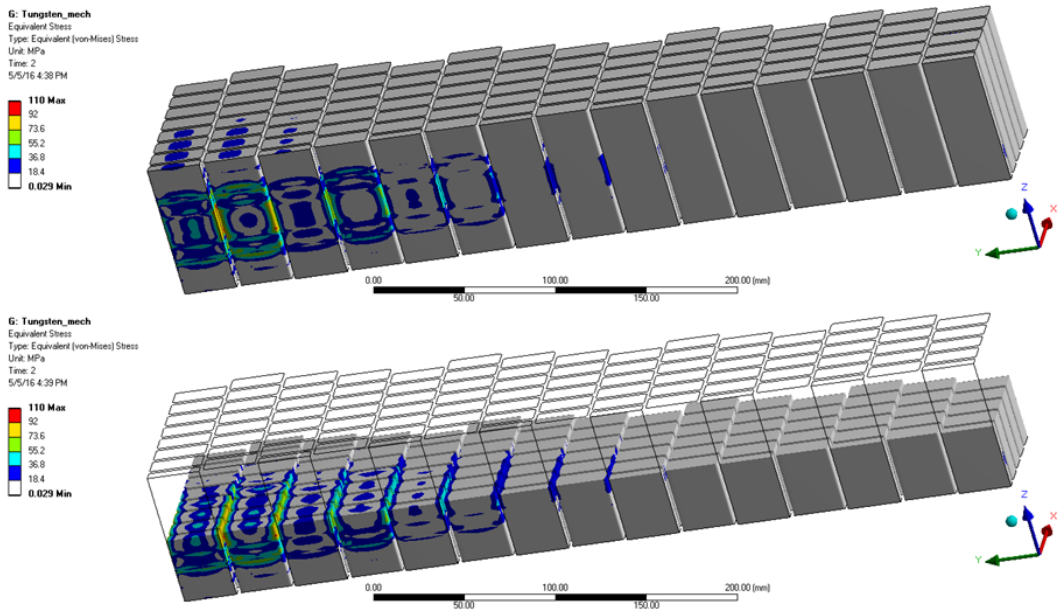

Figure 44: Von-Mises equivalent stress profile of the tungsten at the end of the pulse

10.2 SF2: Vertical displacement beam

Based on the description shown on Section 2, loads on this scenario are produced by the design beam under nominal frequency, with the wheel at his nominal rotation speed. Also the beam is considered synchronized with the wheel and hitting tungsten with a positive vertical displacement of 1 cm from the center of the cassette, as indicated in Figure 45. The cooling system is working at nominal conditions, so helium mass flow trough the wheel is 3.0 kg/s which means 0.0833 kg/s in each cassette.

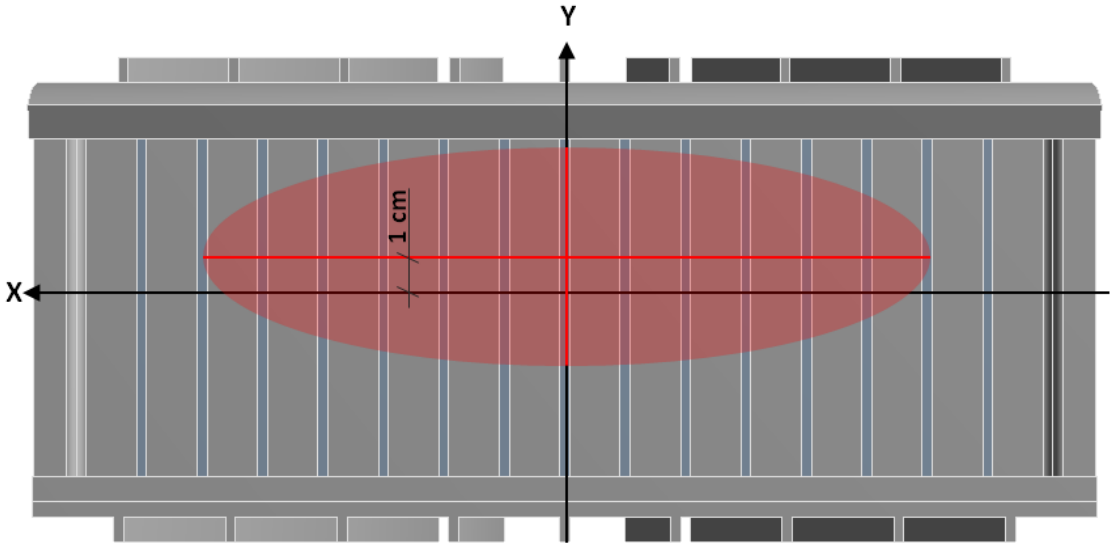

Figure 45: Beam vertical displacement

The solution has been obtained following the methodology described in the section 7, which means solve the described CFD and FEM models. The vertical displacement of the beam changes the temperature profile of the helium flowing between the spallation materia. For this reason, a new tungsten wall convection boundary condition was obtained from the one half vertical symmetry CFD model described in the section 7.3. This convection boundary condition differs from SF1 load scenario, however in the cassette plates convection has been considered the same as SF1 case.

In the Figure 46 is shown the time evolution of the maximum temperature of the whole system during one pulse, once reached the steady state with the beam vertically displaced 1 cm. The maximum temperature increase happens when the beam hits the tungsten, the energy deposition of the protons interacting the spallation material produces a ΔT of 100^{o}C, which occurs in the brick 1 (Figure 46). The front rows bricks have higher heat deposition by protons but are better cooled, for this reason at the end of the cooling the temperature of front bricks is lower than others. The brick 2 (46) has the maximum temperature at the end of the cooling. As the figure 47 shows the vertical displacement of the proton beam produces 12^{o}C of maximum temperature increase comparing with SF1 load condition.

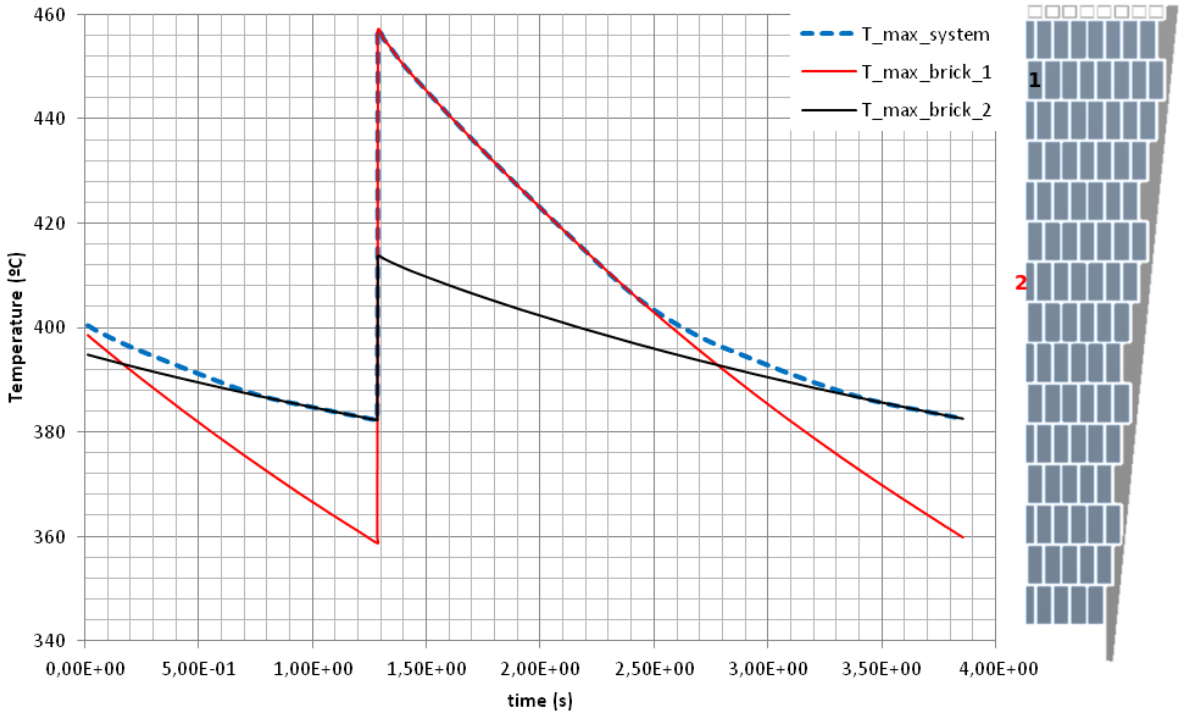

Figure 46: Time evolution of Maximum temperature for the system and tungsten bricks

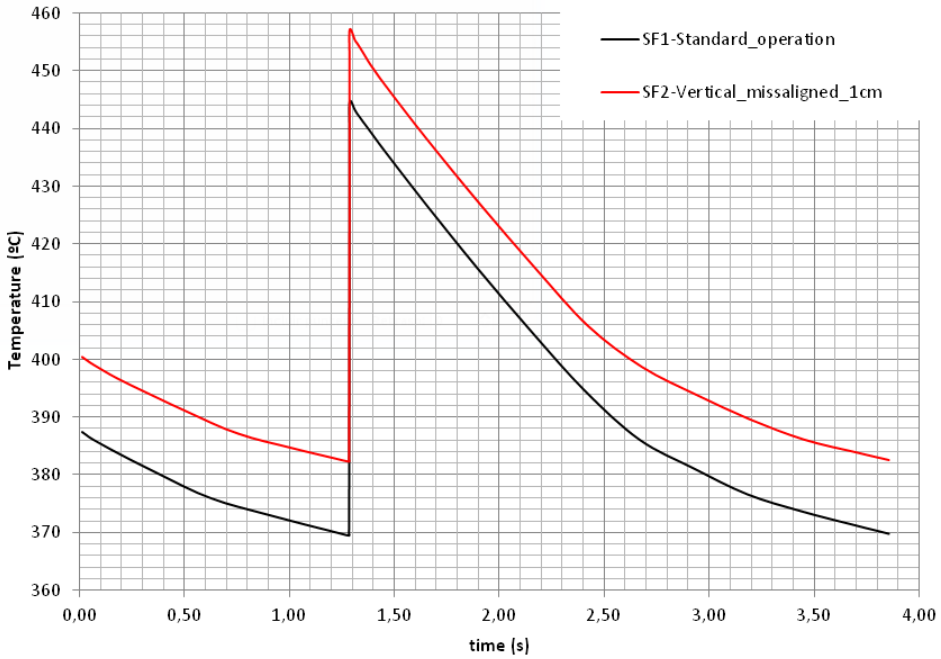

Figure 47: Time evolution of spallation material maximum temperature on SF1:Nominal conditions and SF2: Vertically displaced beam by 1 cm.

In the Figures 48 and 49 it is shown, respectively, the temperature profile of the spallation material at the end of the cooling and at the end of a protons beam pulse. The maximum temperature at the end of the cooling is 370°C and after the pulse is 445°C, but as is shown in Figure 40 the hottest brick changes during the pulse and subsequent cooling cycle.

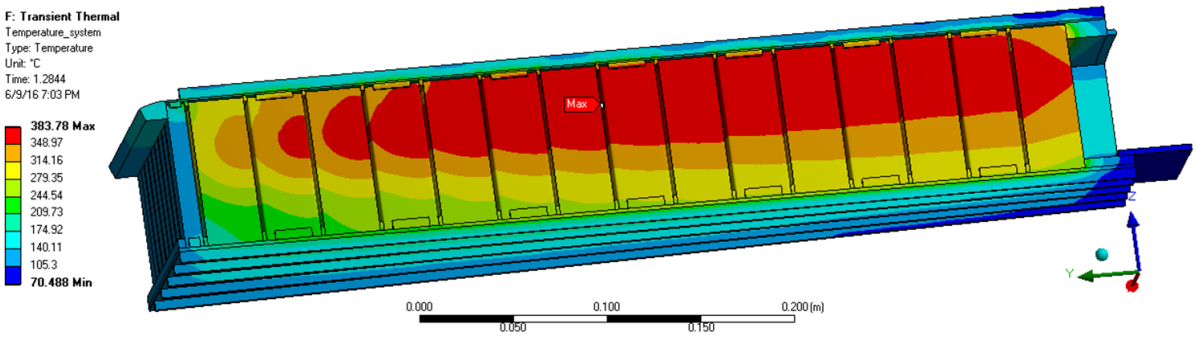

Figure 48: Temperature profile of the tungsten at the end of the cooling

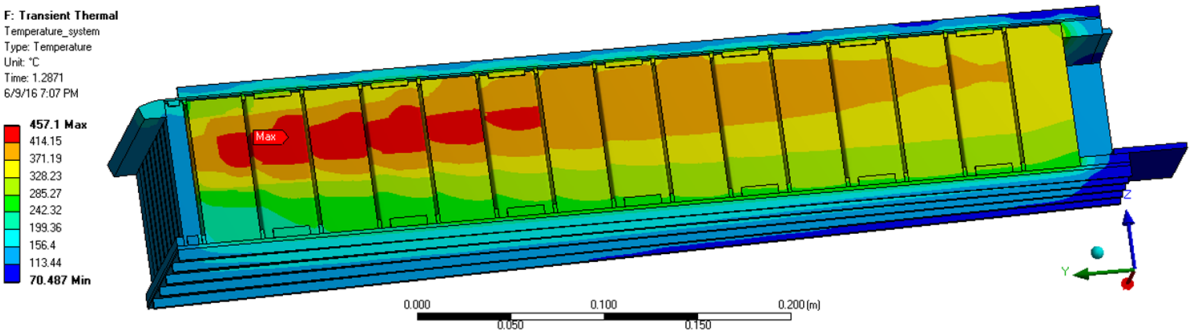

Figure 49: Temperature profile of the tungsten at the end of the pulse

In the Figures 50 and 51 it is shown, respectively, the von-Mises equivalent stress profile of the spallation material at the end of the cooling and at the end of a proton beam pulse. The maximum stress at the end of the cooling is 43 MPa and after the pulse is 111 MPa. The stress profile obtained in this load scenario is practically the same as the produced in then SF1 load scenario.

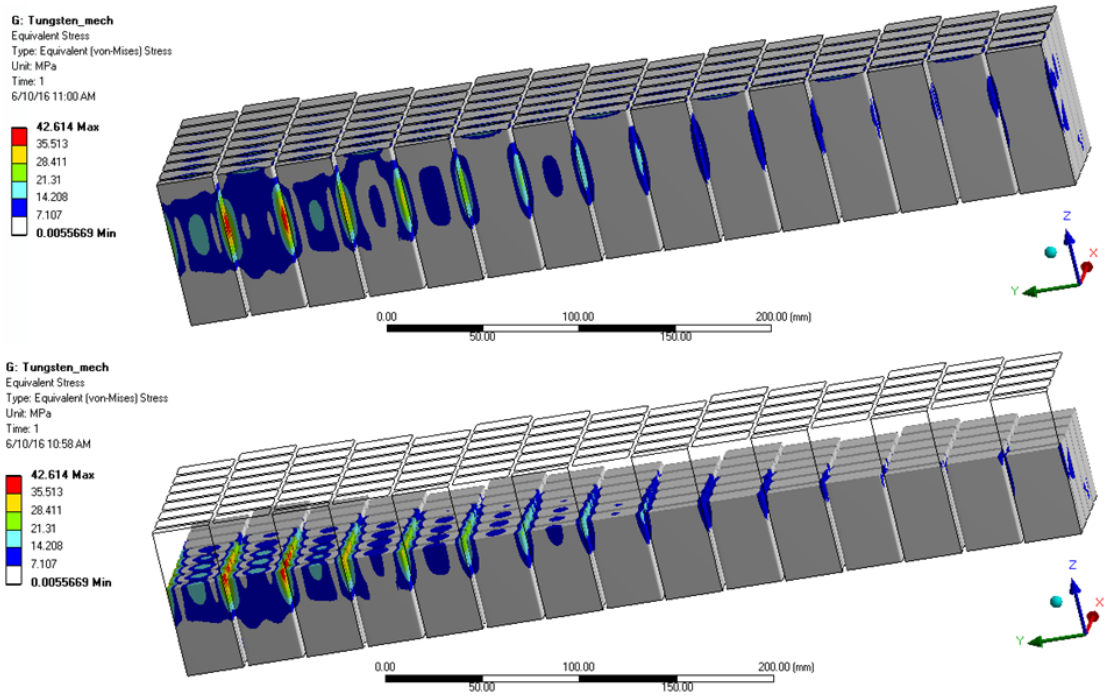

Figure 50: Von-Mises equivalent stress profile of the tungsten at the end of the cooling

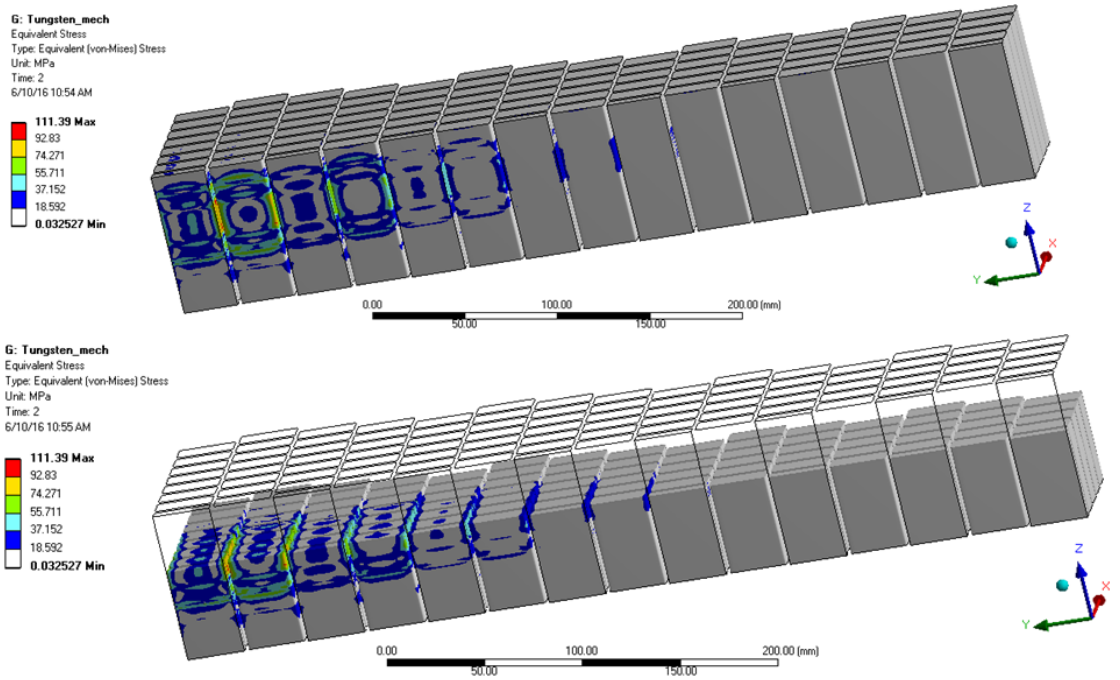

Figure 51: Von-Mises equivalent stress profile of the tungsten at the end of the pulse

10.3 SF2: Unsynchronized wheel

Based on the description shown on Section 2, loads on this scenario are produced by the design beam under nominal frequency, with the wheel at his nominal rotation speed. The beam is considered vertically centered but unsynchronised with the wheel rotation which produces a horizontal displacement of 1 cm from the center of the cassette (Figure 52). The cooling system is working at nominal conditions so helium mass flow trough the wheel is 3.0 kg/s, which means 0.0833 kg/s in each cassette.

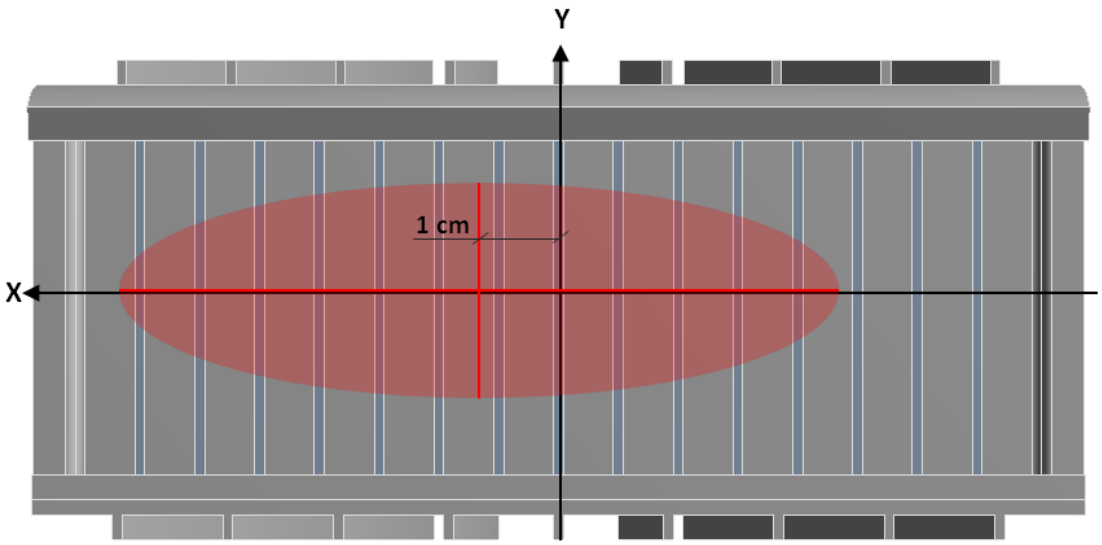

Figure 52: Beam horizontally displaced

The solution has been obtained following the methodology described in the section 7, which means solve the described CFD and FEM models. The horizontal displacement of the beam changes the temperature profile of the helium flowing between the spallation material for this reason a new tungsten wall convection boundary condition was obtained from the one half horizontal symmetry CFD model described in the section 7.3. This convection boundary condition differs from SF1 load scenario, however for the cassette plates convection has been considered the same as SF1 case.

In the Figure 53 is shown the time evolution of the maximum temperature of the whole system during one pulse, once reached the steady state with the beam horizontally displaced by 1 cm. The maximum temperature increase happens when the beam hits the tungsten, the energy deposition of the protons interacting the spallation material produces a ΔT of 100^{o}C, which occurs in the brick 1 (Figure 53). The front rows bricks have higher heat deposition by protons but are better cooled, for this reason at the end of the cooling the temperature of front bricks is lower than others. The brick 2 (53) has the maximum temperature at the end of the cooling process. As Figure 54 shows, the horizontal displacement of the proton beam produces 4^{o}C of maximum temperature increase comparing with SF1 load condition, also the position of the hottest bricks changes (bricks 1 and 2 in the Figure 53).

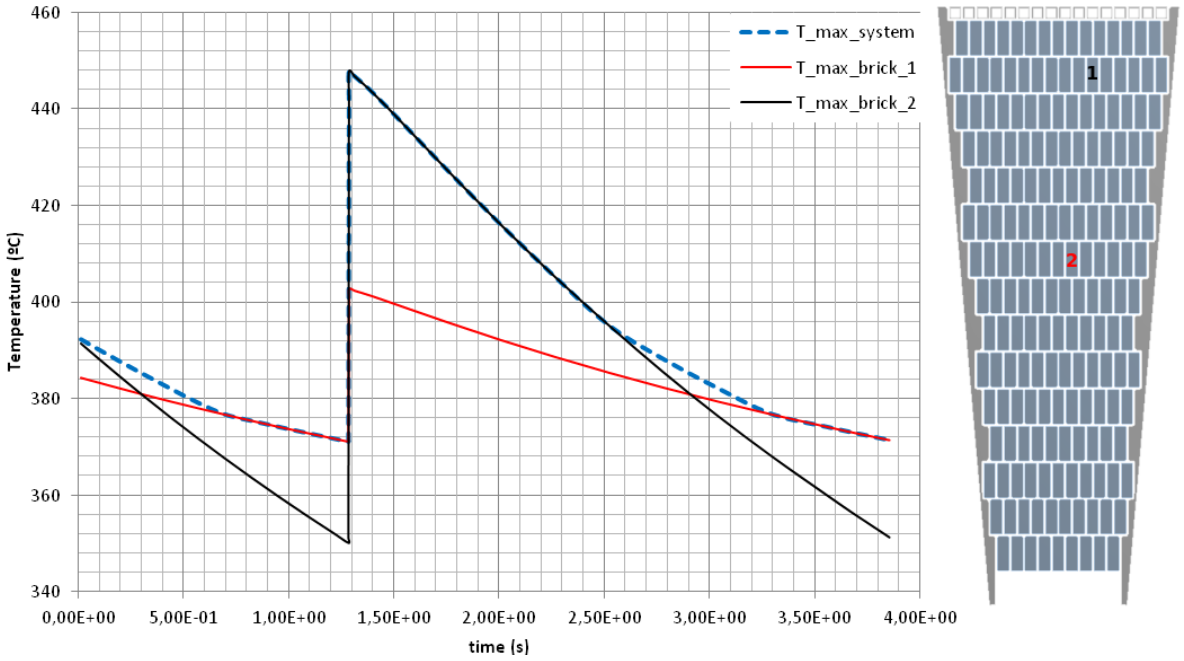

Figure 53: Time evolution of Maximum temperature for the system and tungsten bricks

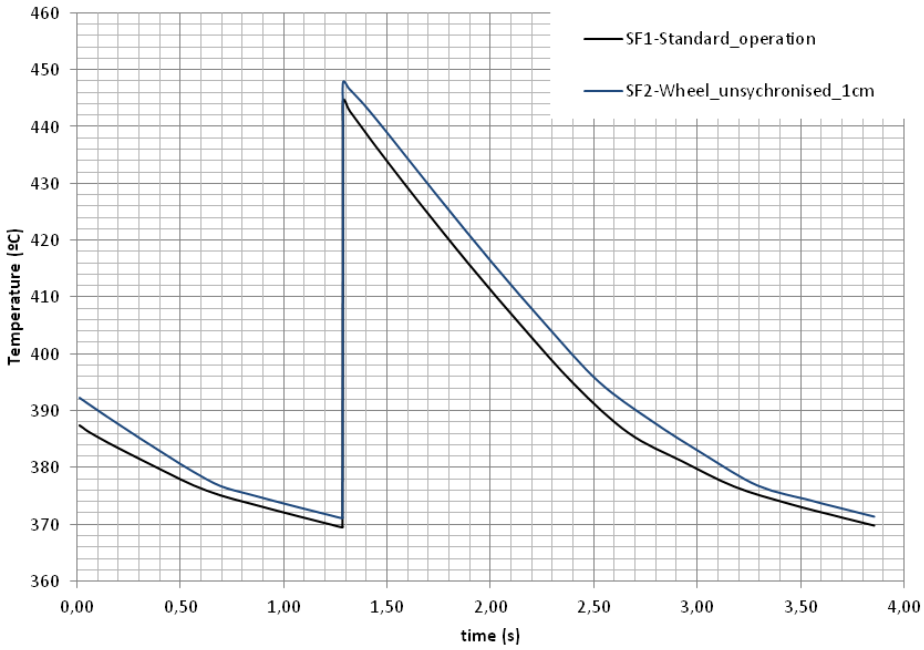

Figure 54: Time evolution of spallation material maximum temperature on SF1:Nominal conditions and SF2: Unsynchronized wheel.

In the Figures 55 and 56 it is shown, respectively, the temperature profile of the spallation

material at the end of the cooling and at the end of a protons beam pulse. The maximum temperature at the end of the cooling is 370^{o}C and after the pulse is 445^{o}C, but as is shown in Figure 40 the hottest brick changes during the pulse and subsequent cooling.

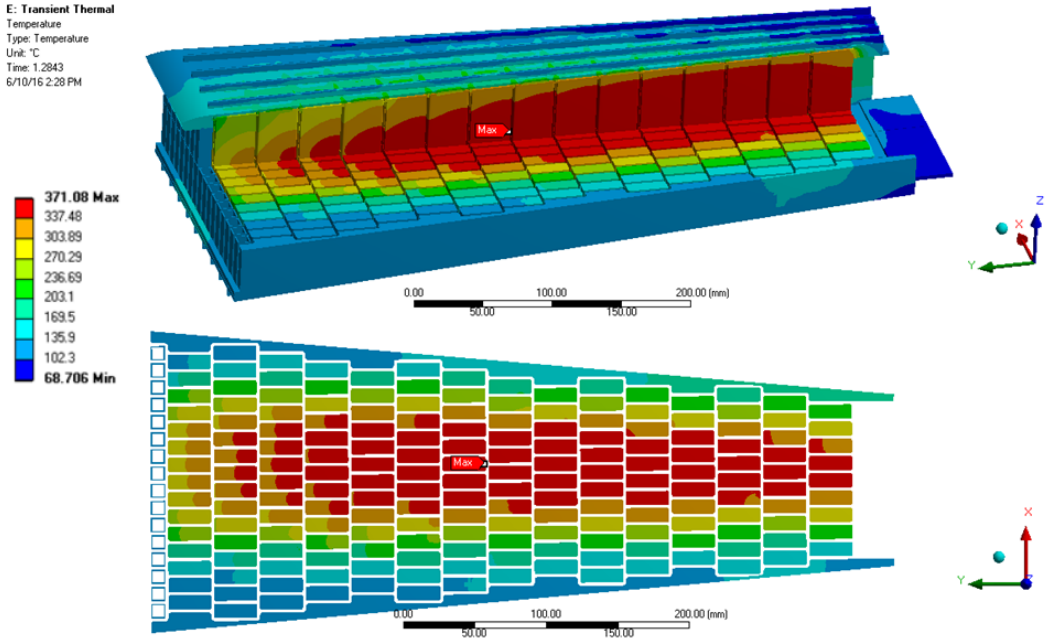

Figure 55: Temperature profile of the tungsten at the end of the cooling

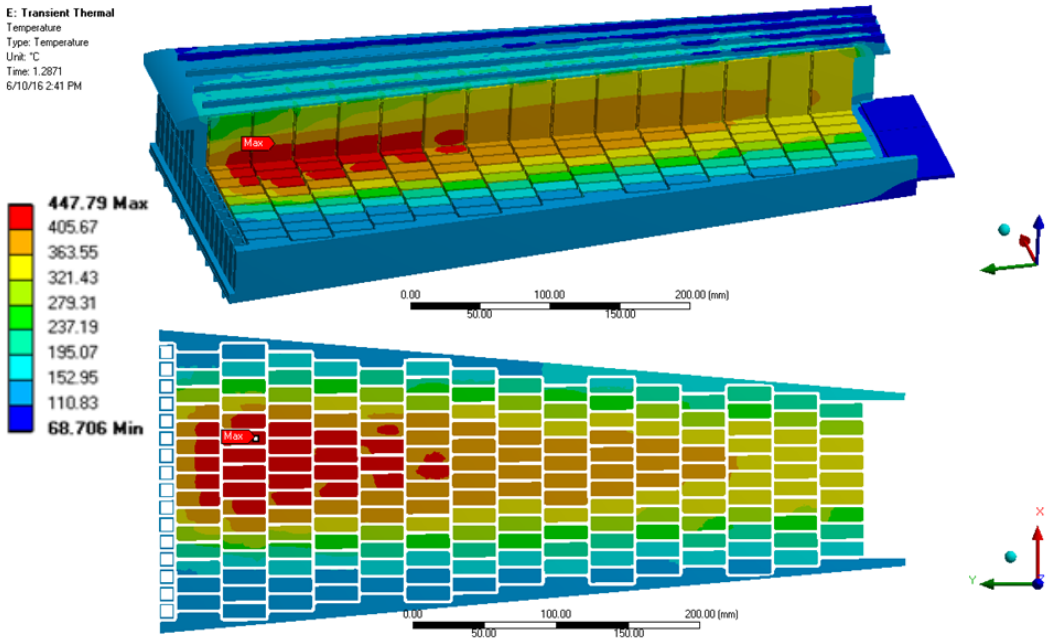

Figure 56: Temperature profile of the tungsten at the end of the pulse

In the Figures 57 and 58 it is shown, respectively, the von-Mises equivalent stress profile of the spallation material at the end of the cooling and at the end of a proton beam pulse. The maximum stress at the end of the cooling is 43 MPa and after the pulse is 95 MPa. The stress profile obtained in this load scenario is practically the same as the produced on SF1 load scenario at the end of the cooling however is 16 MPa lower at the end of the protons pulse.

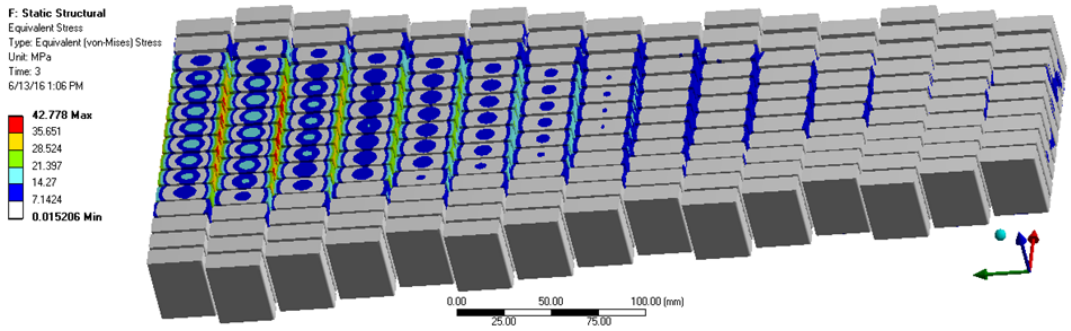

Figure 57: Von-Mises equivalent stress profile of the tungsten at the end of the cooling

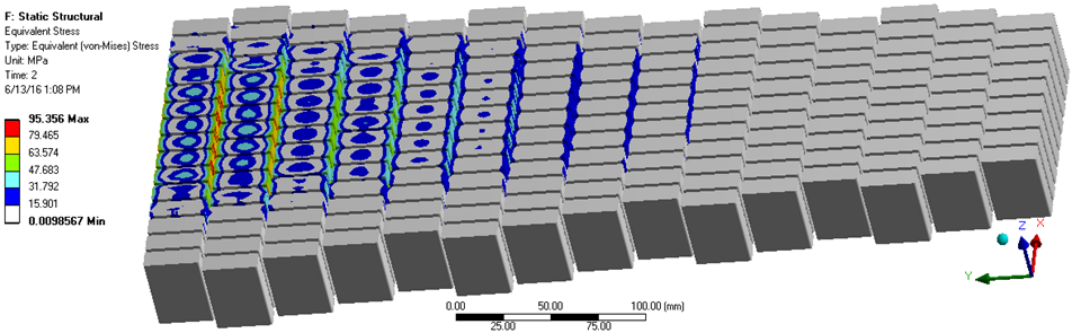

Figure 58: Von-Mises equivalent stress profile of the tungsten at the end of the pulse

10.4 SF2: Channel blockage

Based on the description shown on Section 2, loads on this scenario are produced by the design beam under nominal frequency, with the wheel at his nominal rotation speed. The beam is considered centered and synchronized with the wheel rotation. The cooling system is working at nominal conditions so helium mass flow trough the wheel is 3.0 kg/s, which means 0.0833 kg/s in each cassette.
For this load scenario it is considered that one of the helium channels is completely blocked. To simulate the non-cooling conditions, the adjacent walls of the channel are considered adiabatic (Figure 59). The marked channel in the Figure 59 was chosen because its blockage is the worst from the thermomechanical point of view for this load scenario.

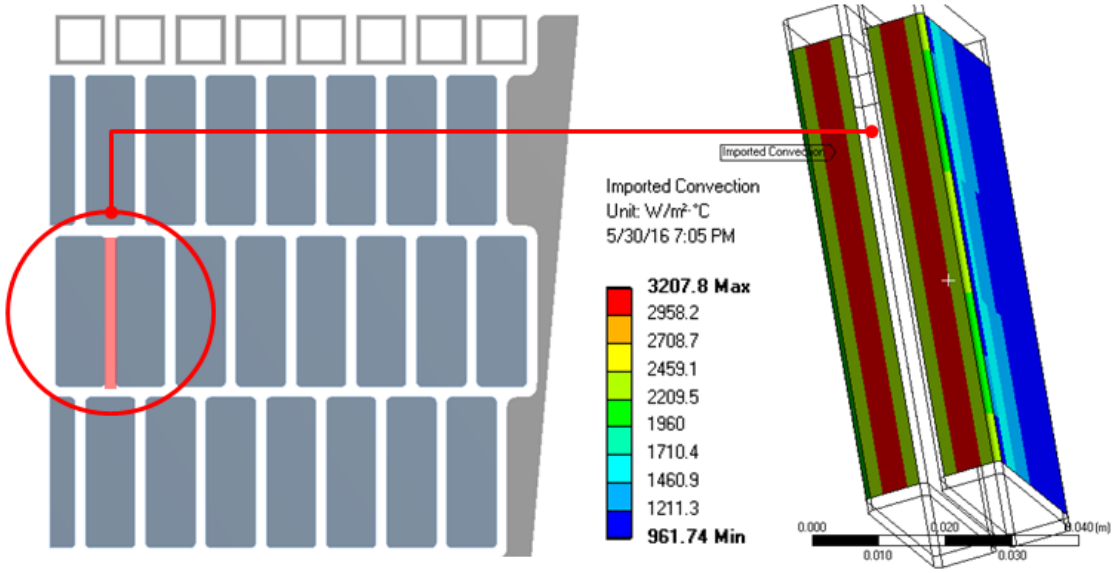

Figure 59: Blocked channel and convection BC applied in adjacent tungsten walls

The solution has been obtained following the methodology described in the section 7, which means to solve the described CFD and FEM models. The convection boundary conditions in the tungsten walls and the cassette plates is the same as considered in the SF1 load scenario, except in the adjacent walls of the blocked channels where the convection BC was suppressed.

In the Figure 60 is shown the time evolution of the maximum temperature of the whole system during one pulse, once reached the steady state with the mentioned channel blockage.The temperature in the bricks 1 and 2 is 70^{o}C, higher than the same bricks in the SF1 load scenario (Figure 61).

In the Figures 62 and 63 it is shown respectively the temperature profile of the spallation material at the end of the cooling and at the end of a protons beam pulse. The maximum temperature at the end of the cooling is 422^{o}C and after the pulse is 518^{o}C. The maximum temperature of the system is located in the bricks 1 and 2 of Figure 60 because of the channel blockage and a worse cooling.

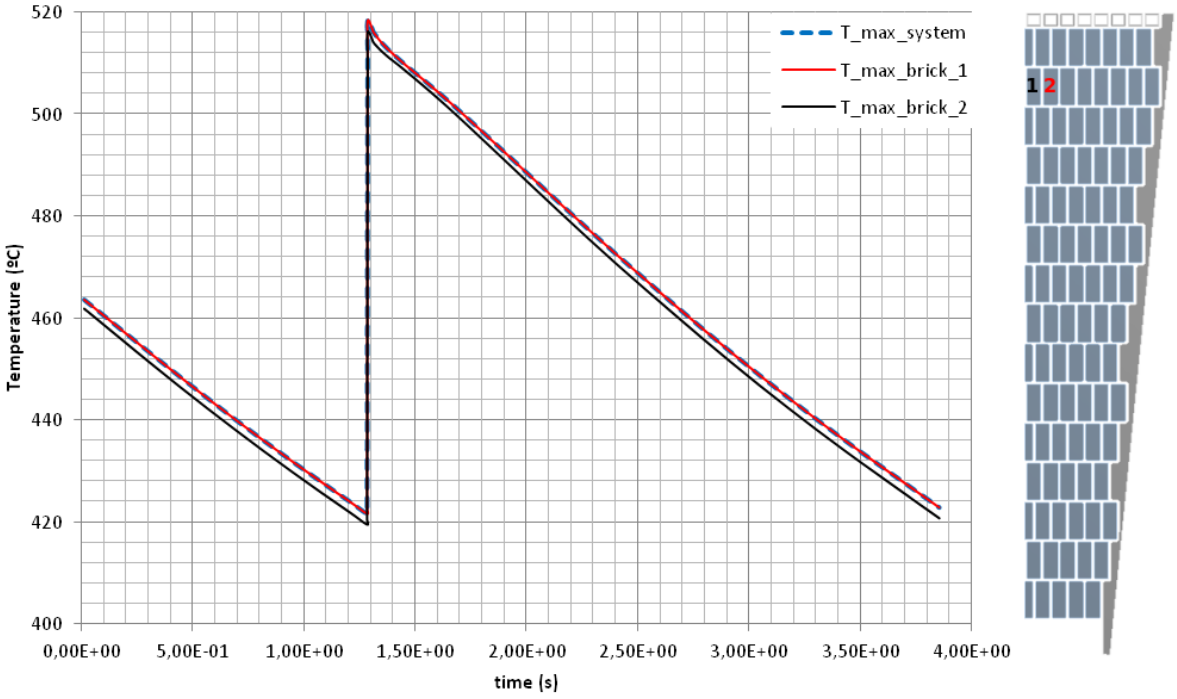

Figure 60: Time evolution of Maximum temperature for the system and tungsten bricks

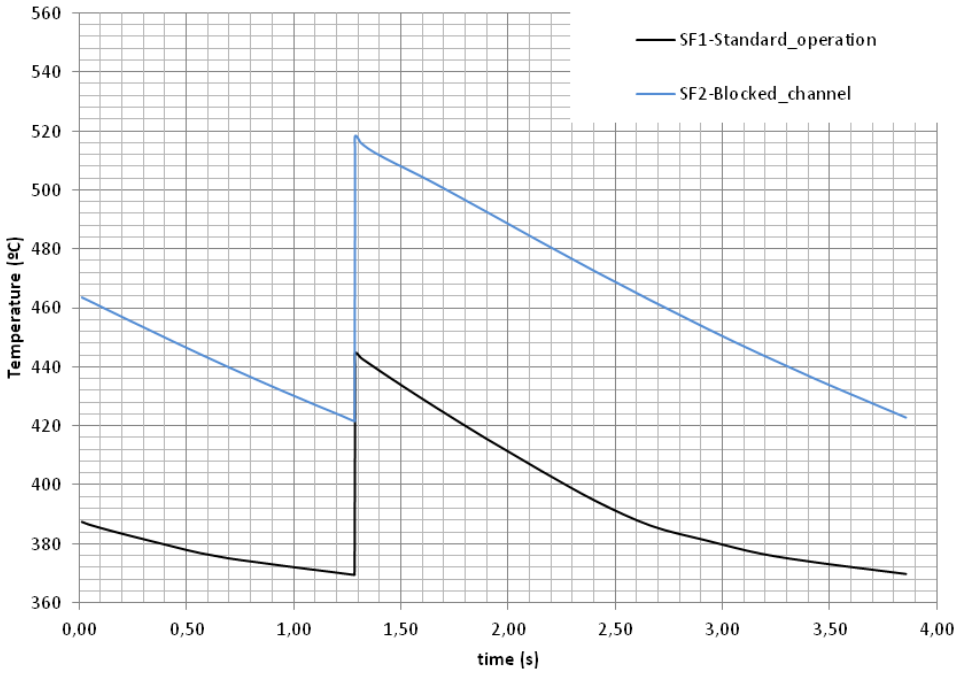

Figure 61: Time evolution of spallation material maximum temperature on SF1:Nominal conditions and SF2: Channel blockage.

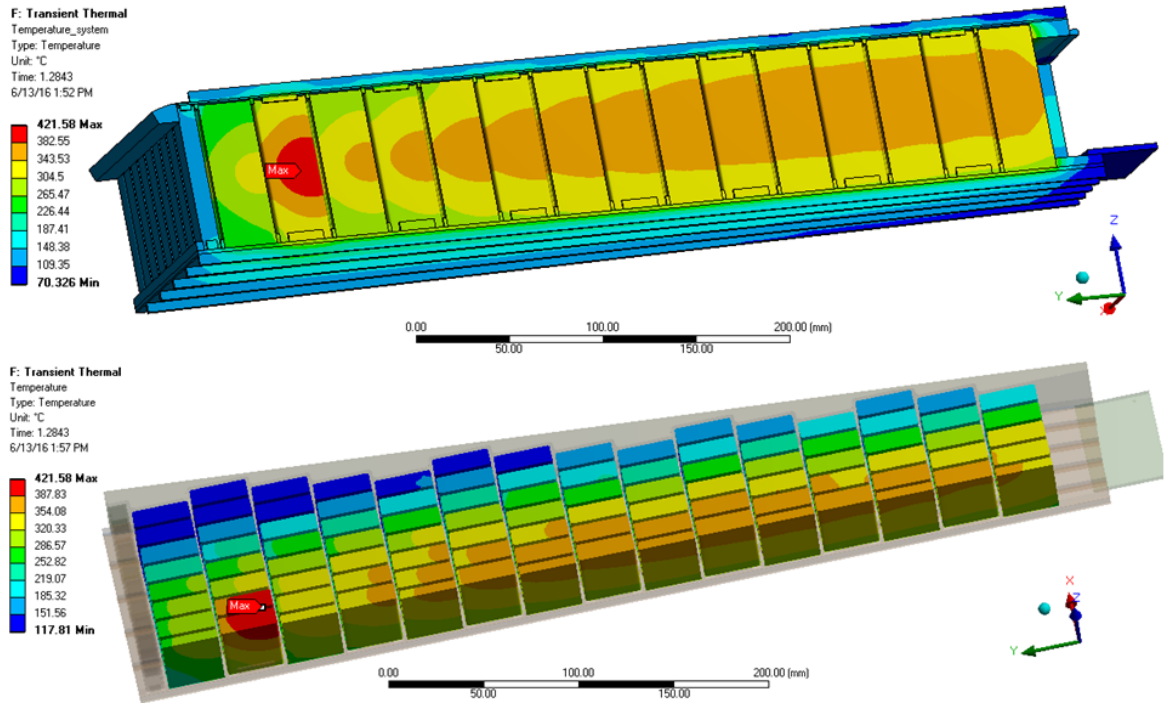

Figure 62: Temperature profile of the tungsten at the end of the cooling

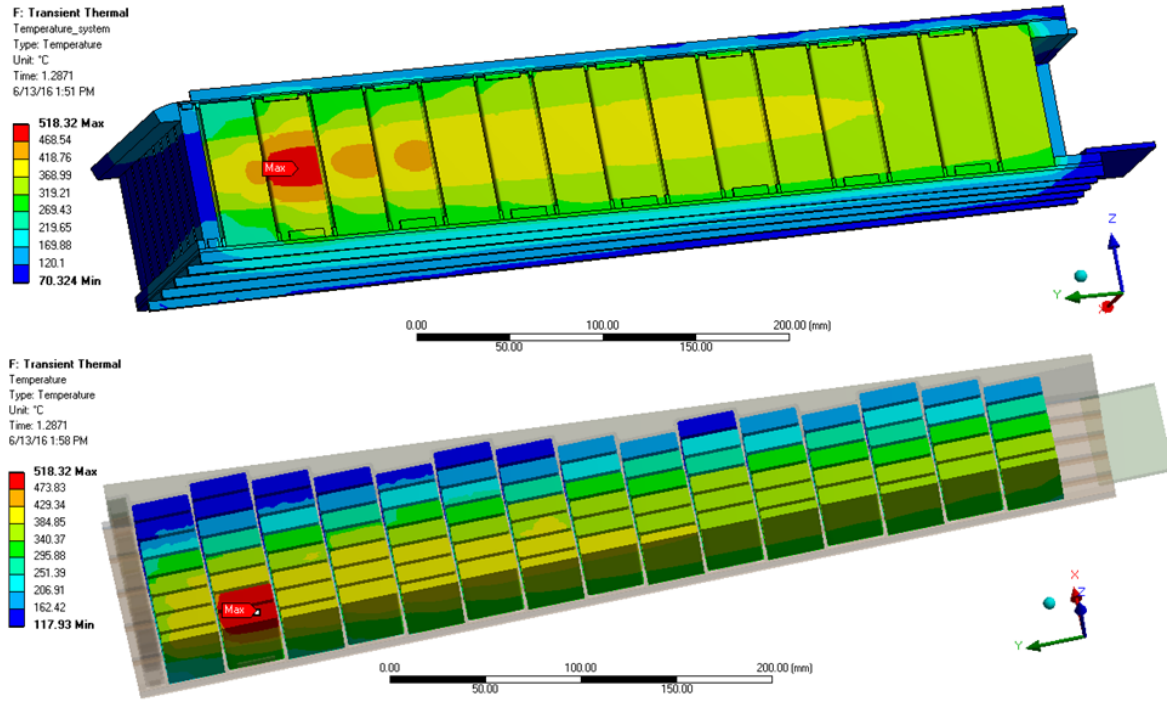

Figure 63: Temperature profile of the tungsten at the end of the pulse

In the Figures 64 and 65 it is shown, respectively, the von-Mises equivalent stress profile of the spallation material at the end of the cooling and at the end of a proton beam pulse. The maximum stress at the end of the cooling is 58 MPa and after the pulse is 125 MPa. The stress profile obtained in the adjacent bricks to the blocked channel is 15 MPa higher compared to the SF1 load scenario.

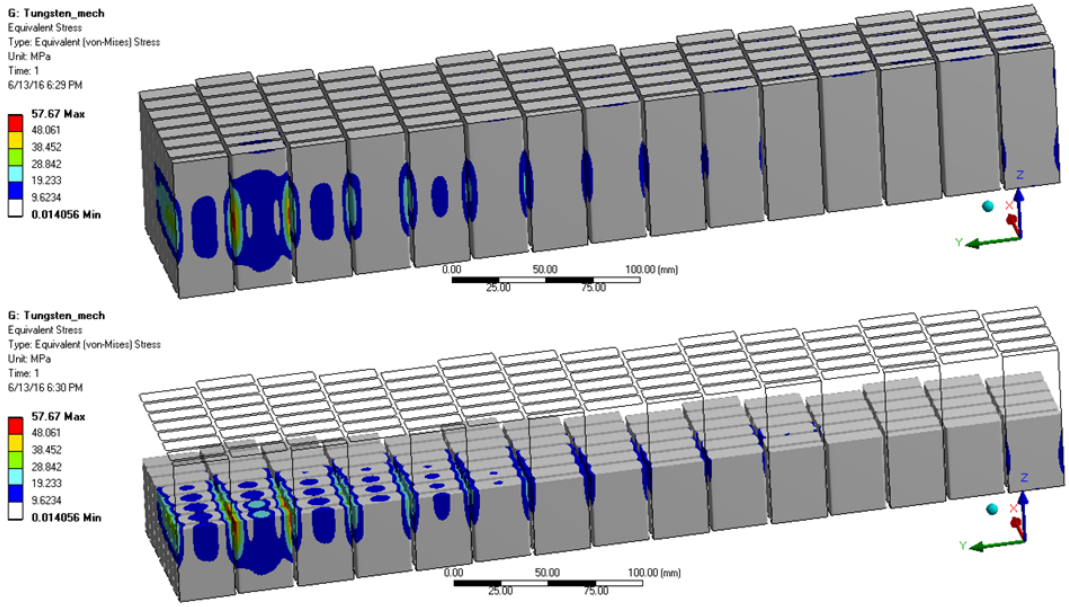

Figure 64: Von-Mises equivalent stress profile of the tungsten at the end of the cooling

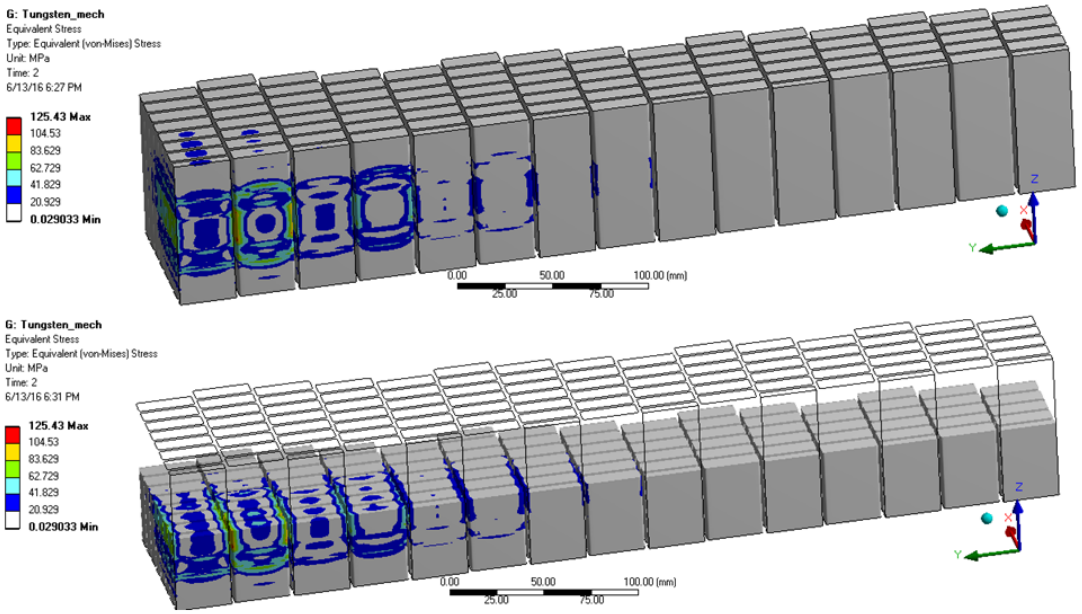

Figure 65: Von-Mises equivalent stress profile of the tungsten at the end of the pulse

10.5 SF2: Tungsten brick break

Based on the description shown on Section 2, loads on this scenario are produced by the design beam under nominal frequency with the wheel at his nominal rotation speed. The beam is considered centered and synchronized with the wheel rotation. The cooling system is working at nominal conditions so helium mass flow trough the wheel is 3.0 kg/s, which means 0.0833 kg/s in each cassette.
For this load scenario it is considered that one of the tungsten bricks was broken, left its position and is in perfect contact with the adjacent brick as show in the Figure 66. The considered broken brick and its position on the adjacent brick are the worst configuration from the thermomechanical point of view for this type of accident.

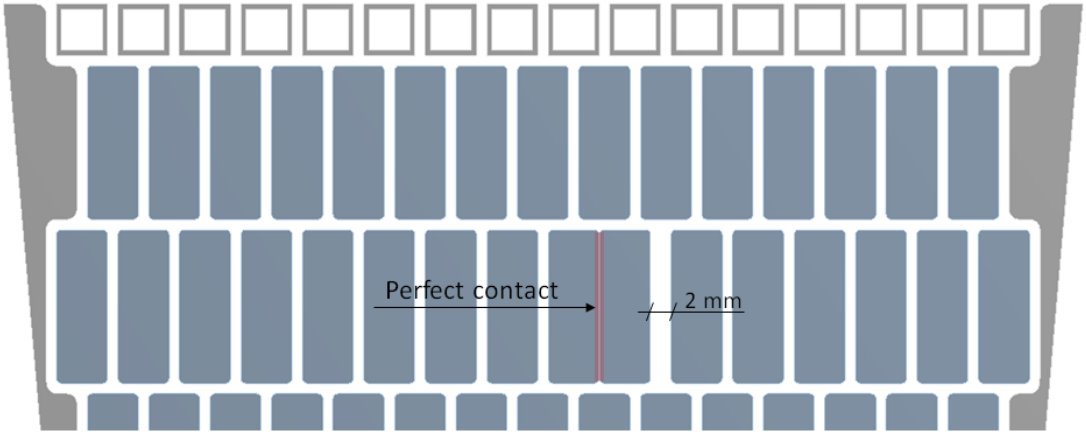

Figure 66: Broken brick considered position

The solution has been obtained following the methodology described in the section 7, which means solve the described CFD and FEM models. The change in the position of the broken bricks modifies the helium flux, therefore it is necessary recalculate the convection boundary condition in the tungsten walls solving the CFD model with the new geometry. However the cassette plates convection has been considered the same as SF1 load scenario.

In the Figure 67 is shown the time evolution of the maximum temperature of the whole system during one pulse, once reached the steady state with the beam horizontally displaced 1 cm. The maximum temperature increase happens when the beam hits the tungsten, the energy deposition of the protons interacting the spallation material produces a ΔT of 100^oC, which occurs in the brick 1 and 2 (Figure 67).

The maximum temperature of the system is located in the contact between the broken brick (brick 1) and the adjacent (brick 2). Due to the protons beam interaction, this zone has the highest heat deposition and the perfect contact assumed prevents the coolant flow. The Figure 68 also shows the temperature evolution of the bricks to the sides of the bricks in contact, the temperature these bricks (brick 3 and 4) is more than 110^oC lower than the bricks 1 and 2.
In the Figure 67 is shown the time evolution of the maximum temperature of the whole system

during one pulse once reached the steady state with the mentioned channel blockage.The temperature in the bricks 1 and 2 is 100^{o}C higher than the same bricks in the SF1 load scenario (figure 68).

In the Figures 69 and 70 it is shown, respectively, the temperature profile of the spallation material at the end of the cooling and at the end of a protons beam pulse. The maximum temperature at the end of the cooling is 444^{o}C and after the pulse is 545^{o}C. The maximum temperature of the system is located in the bricks 1 and 2 of Figure 67 because of the channel blockage and a worse cooling process.

In the figures 71 and 73 it is shown respectively the von-Mises equivalent stress profile of the spallation material at the end of the cooling and at the end of a proton beam pulse. The maximum stress at the end of the cooling is 61 MPa and after the pulse is 113 MPa. Although the temperature is 100 °C greater in the broken and adjacent brick due to the mechanical boundary conditions there is no restriction for the thermal expansion of the broken brick so the mechanical stress is not much higher compared to the SF1 load scenario.

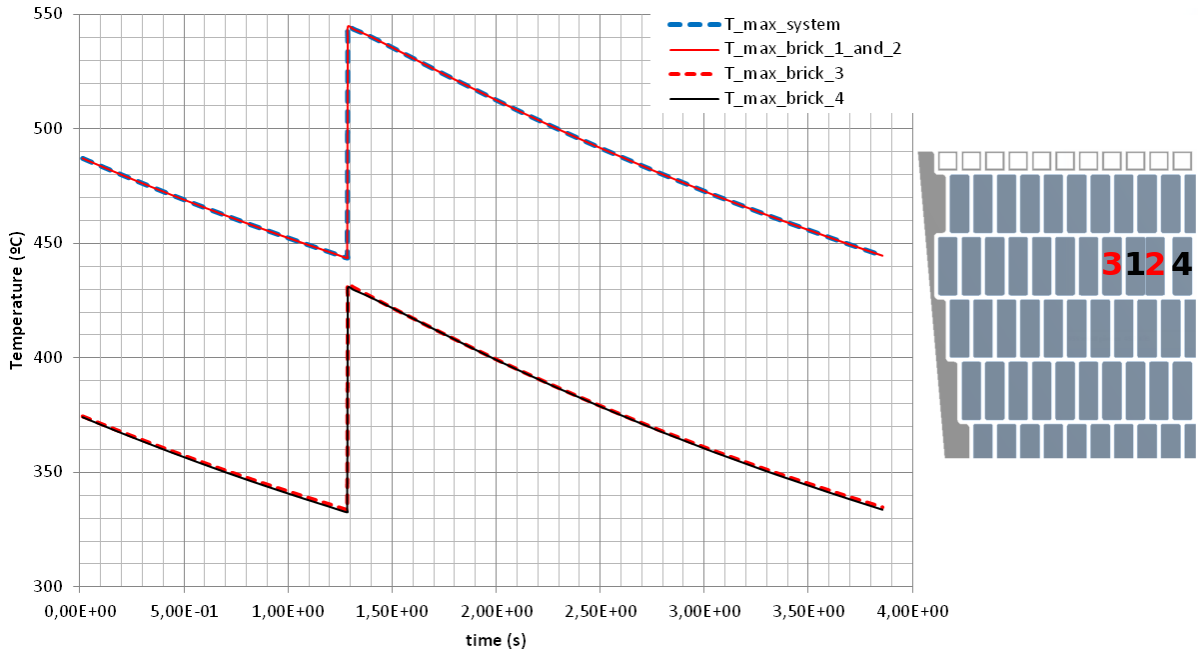

Figure 67: Time evolution of Maximum temperature for the system and tungsten bricks

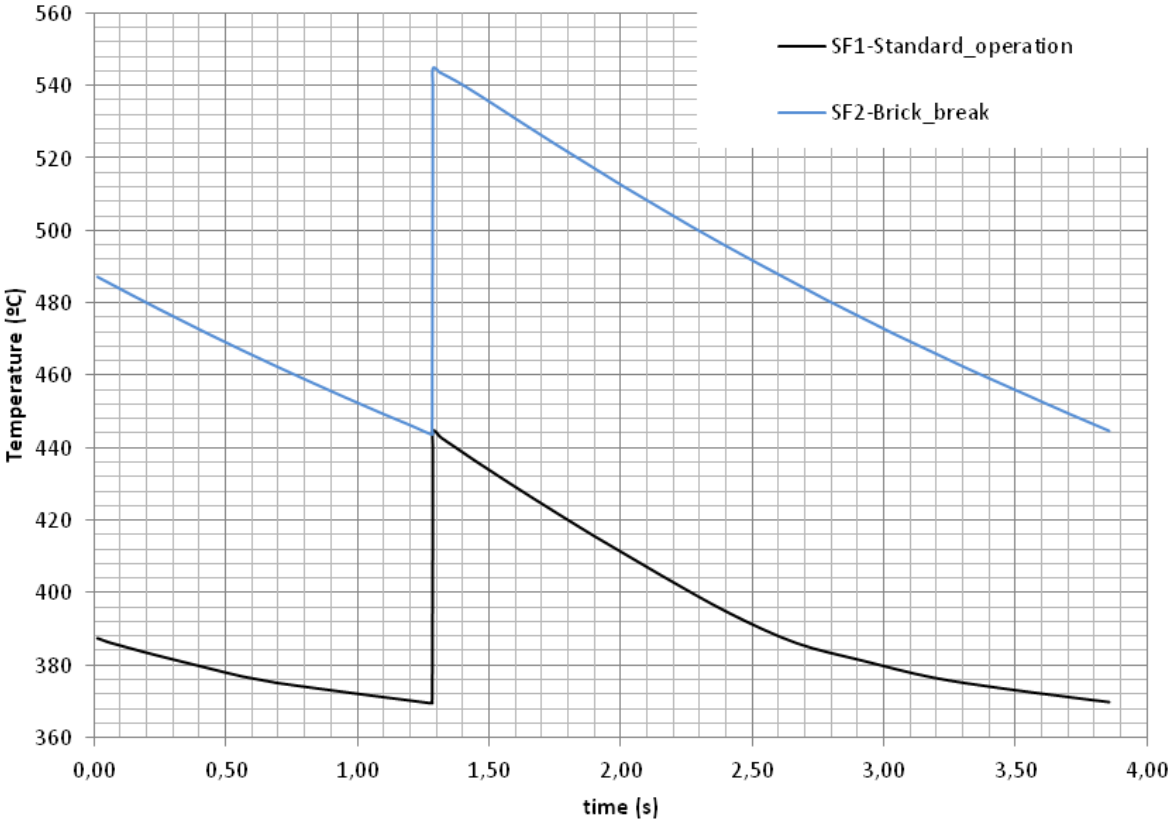

Figure 68: Time evolution of spallation material maximum temperature on SF1:Nominal conditions and SF2: Brick break.

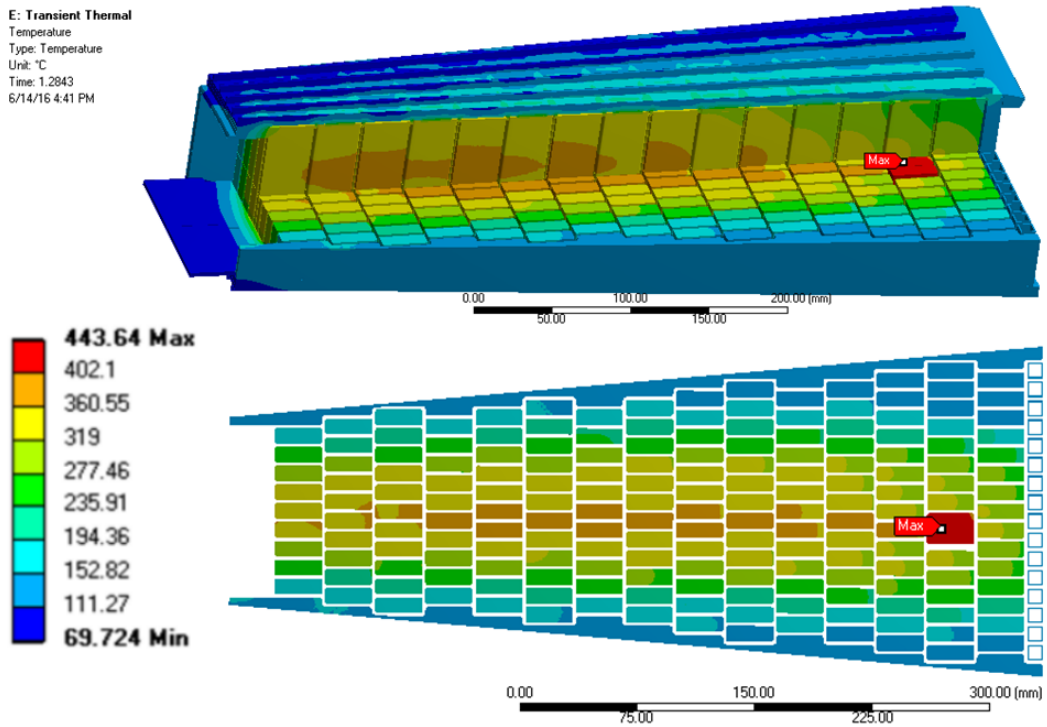

Figure 69: Temperature profile of the tungsten at the end of the cooling

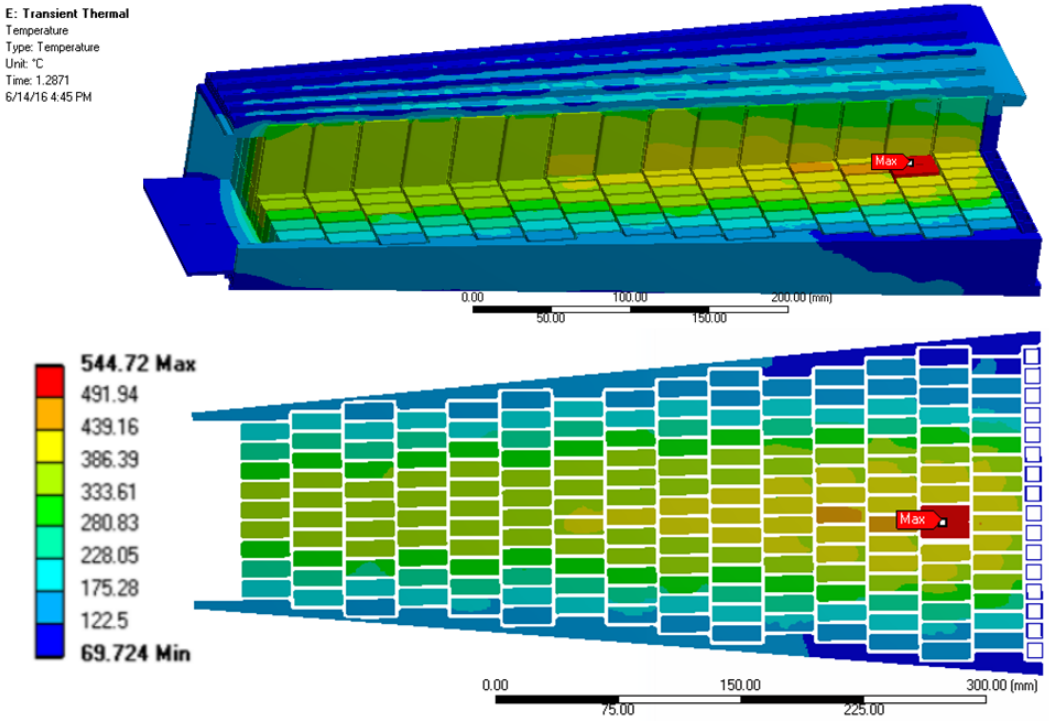

Figure 70: Temperature profile of the tungsten at the end of the pulse

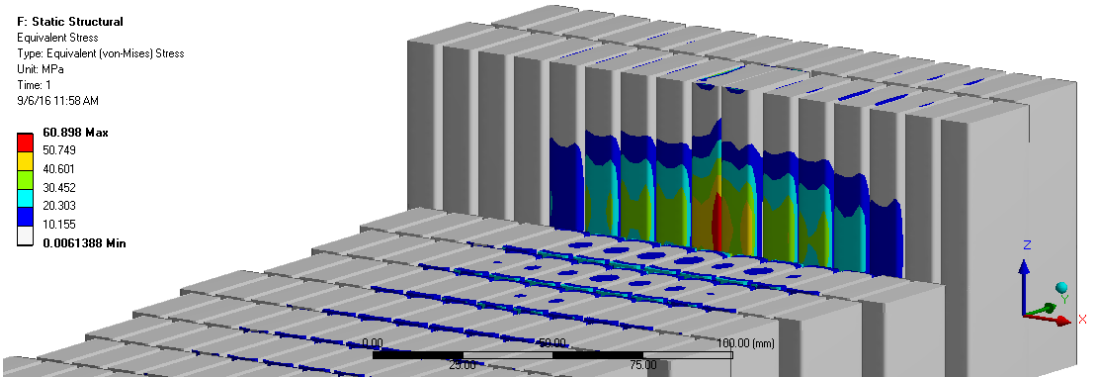

Figure 71: Von-Mises equivalent stress profile of the tungsten at the end of the cooling

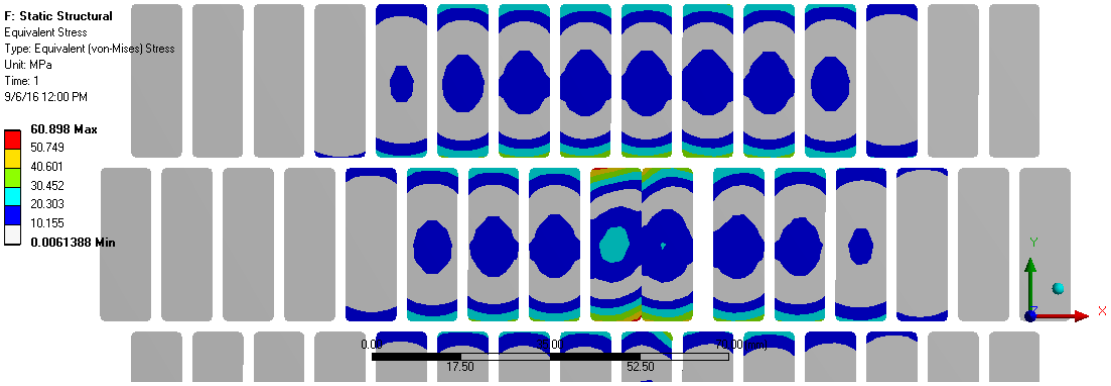

Figure 72: Von-Mises equivalent stress profile of the tungsten at the end of the cooling (XY plane section)

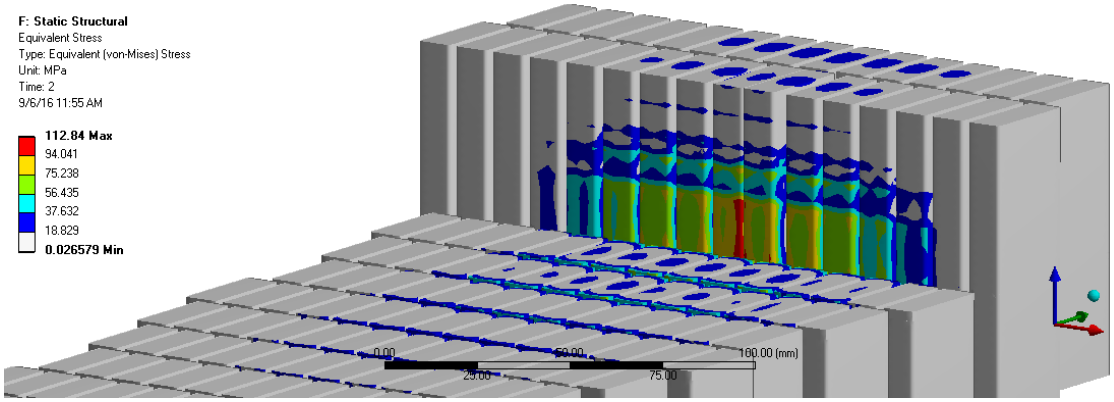

Figure 73: Von-Mises equivalent stress profile of the tungsten at the end of the pulse

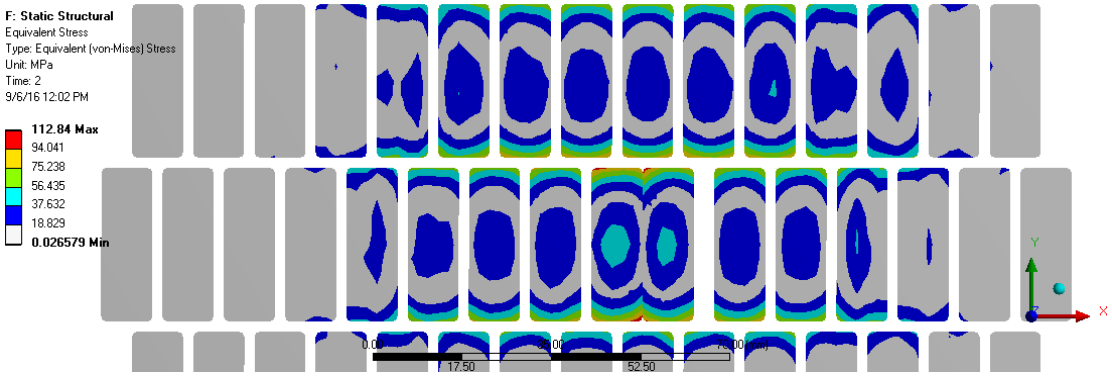

Figure 74: Von-Mises equivalent stress profile of the tungsten at the end of the pulse (XY plane section)

10.6 SF3: Loss of coolant flow and pressure

The conditions described on Table 2 as "Loss of coolant flow and pressure" corresponds to a series of operational accidents in the helium loop that modify the cooling conditions of the spallation material. The Table 10.6 shows the operational conditions for the case in which the cooling conditions is worse that nominal one.

	Entity	Nominal	Machine prot. system trip	Machine prot. max. delay	Target saf. system limit
Low helium pressure	1.1 MPa	1.05 MPa	5 s	0.62 MPa	10 s
Low helium massflow	3 $kg \cdot s^{-1}$	2.8 $kg \cdot s^{-1}$	5 s	2 $kg \cdot s^{-1}$	10 s
High helium inlet temperature	40^oC	50^oC	5 s	240^oC	10 s

Table 9: Loss of coolant flow and pressure scenarios

The modification in the helium inlet conditions will change the heat transfer coefficient and the bulk temperature for the spallation material. However, the stress in the tungsten is produced by the internal temperature gradient and this magnitude will not change significantly with the heat transfer coefficient. On the other hand, this accidental conditions (SF3) do not have any design limit related to the stress. Hence, only thermal problem will be consider for this accidental case.

The modification in the helium inlet conditions will change the heat transfer coefficient and the bulk temperature for the spallation material. However, the stress in the tungsten is produced by the internal temperature gradient and this magnitude will not change significantly with the heat transfer coefficient. On the other hand, this accidental conditions (SF3) do not have any design limit related with the stress. Hence, only thermal problem will be consider for this accidental case.

Regarding the temperature evolution, the "Machine protection system" will stop the beam after a short period of time. However the analysis has been done in steady state conditions that reproduce a very extreme accidental conditions in with the reaction time of the machine protection system is much longer than expected.

In order to simplify the calculations only the CFD model described in the section **??** was used to simulate the loss of coolant accidents and obtain the temperature of the spallation material for each scenario at at average power, this model considers only heat transfer between the tungsten bricks and the coolant which leads to higher maximum temperature in the spallation material than considering also conduction heat transfer between the tungsten and the cassette plates (as considered in FEM model in section 7.4).

The Table 10 shows, the maximum time average temperature during a pulse and the subsequent

cooling once reached the steady state at different scenarios. The maximum temperature at the end of a beam pulse was estimated considering adiabatic heat deposition which is a conservative approximation. Even in this conservative scenario, the maximum temperatures are below the 700^o degrees limit.

	Time average max Temp. [^{o}C]	Pulse end max Temp. [^{o}C]
Design	393	454
Low helium pressure	393	454
Low helium massflow	524	585
High helium inlet temperature	586	647
Low helium pressure and massflow	467	528

Table 10: Maximum temperature on the accidental scenarios

In the low helium pressure scenario the decrease of the operation pressure from the nominal value to 0.62 MPa leads to a decrease of the helium density. To maintain the 3 kg/s of coolant flow the velocity of the helium reaches high values and as consequence the pressure drop is increased in the coolant loop, from 0.12 bar to 0.19 bar just in the spallation material flow path. Due to the maximum pressure drop that the blowers can handle the mass flow will probably be reduced in case of the low helium pressure scenario. Extrapolating from results shown in the document ESS-0066301 1 "Target, Shaft and Rotating seal CFD analysis" to maintain the pressure drop in the helium loop at nominal conditions, the coolant flow should be reduced from 3 kg/s to 2,4 kg/s. For these reasons an additional loss of coolant scenario with 2.4 kg/s of helium massflow pressurized at 0.62MPa was performed (Low helium pressure and massflow).

10.7 SF3: Shut-down

On normal conditions, when the beam is off the helium loop will continue cooling the target along several hours to remove the decay heat. The shut-down scenario described on Section 2 is produced when the helium flow is interrupted after the shutdown of the beam.

The Figure 28 shows the evolution of the residual heat of the spallation material. This amount of heat have to be removed by thermal radiation on the surcaces of the target vessel. The model considered for the analysis is described on Section 7.5.

Figure 75 shows the evolution the evolution of the target maximum temperature. Two scenarios has been evaluated. The scenario 1 considers perfect thermal contact between top ribs in the cassette and the target vessel. For the scenario 2, thermal contact resistance equivalent to 1 mm helium has been included. The thermal resistance increase by $\sim 10^oC$ the temperature of the system hence, this is not the driven factor for the accident.

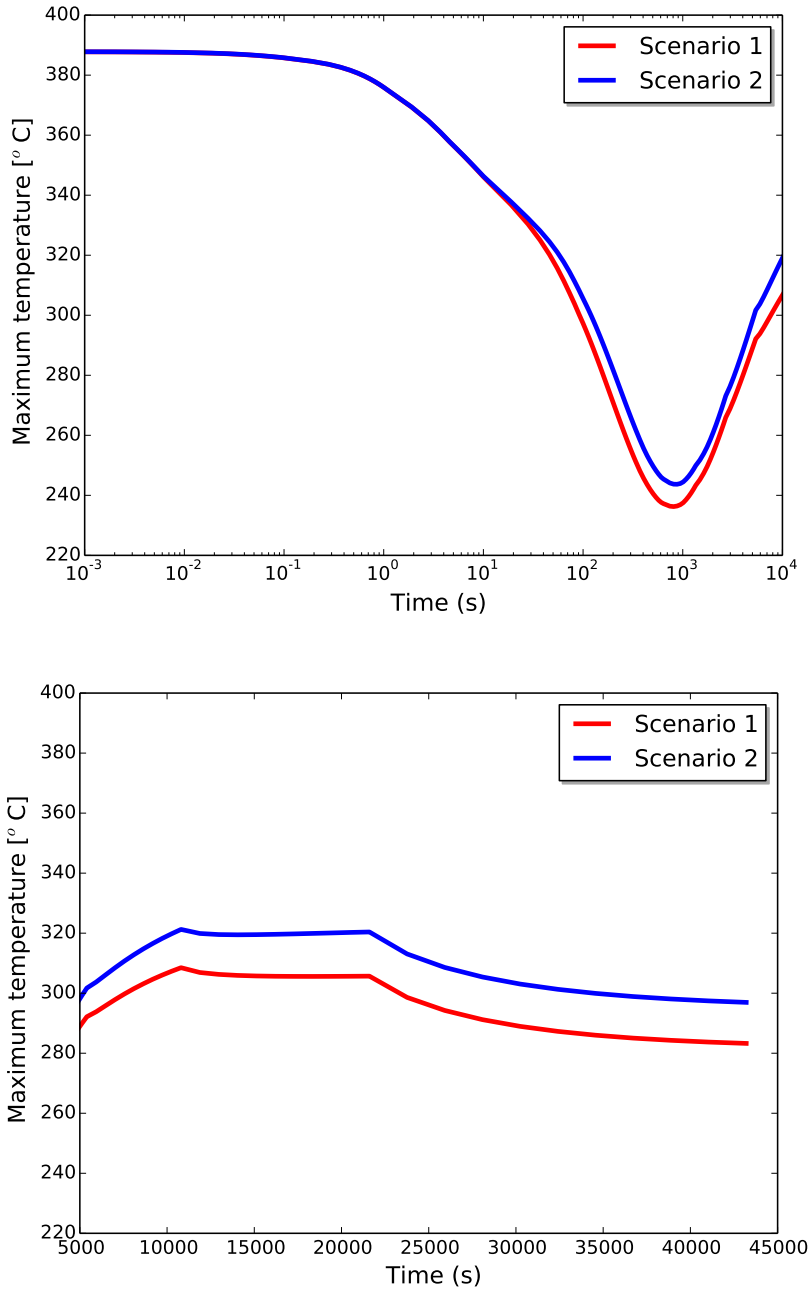

Figure 75: Maximum temperature evolution along the accident

The temperature distribution a few seconds after the shutdown is proportional to the target foot print due to the effect of the helium cooling. When the cooling is stop, the temperature is homogenized along 100 s, this produces a reducing the maximum temperature and increasing the minimum(Figures 76 and 77). After this initial redistribution of the heat the decay heat

increases slowly the temperature. The equilibrium is achieved after $\sim 10^4$ s with a maximum temperature below 330^oC.

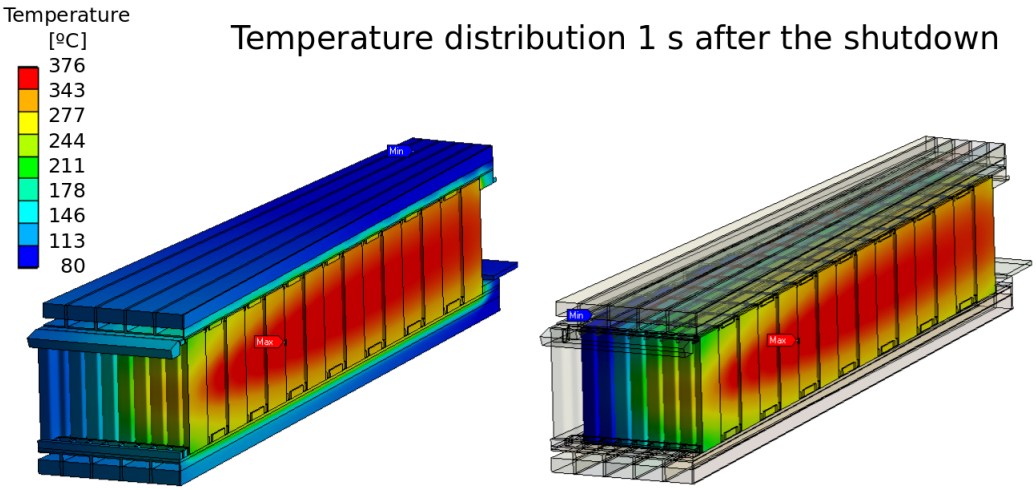

Figure 76: Temperature distribution 1 s after the shutdown

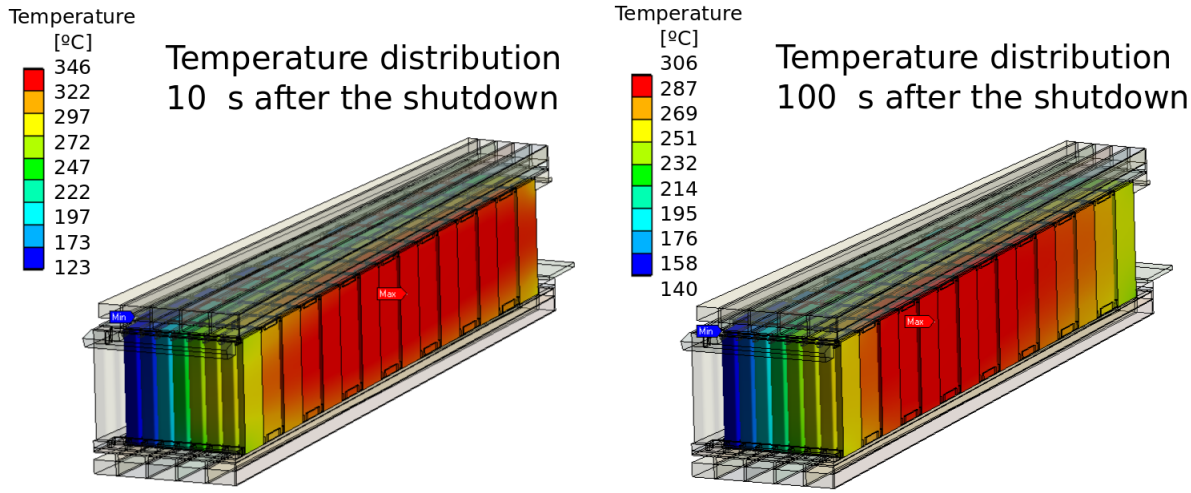

Figure 77: Temperature distribution 10 and 100 s after the shutdown

Figure 78 shows the heat flux in the vessel surfaces for both scenarios. In the scenario 1 (perfect contact) an small difference between top and bottom covers can be observed. This difference is produced by the expansion gap in between top cover of the cassette and spallation material. When the thermal resistance is considered (Scenario 2) the distance between both plates increases.

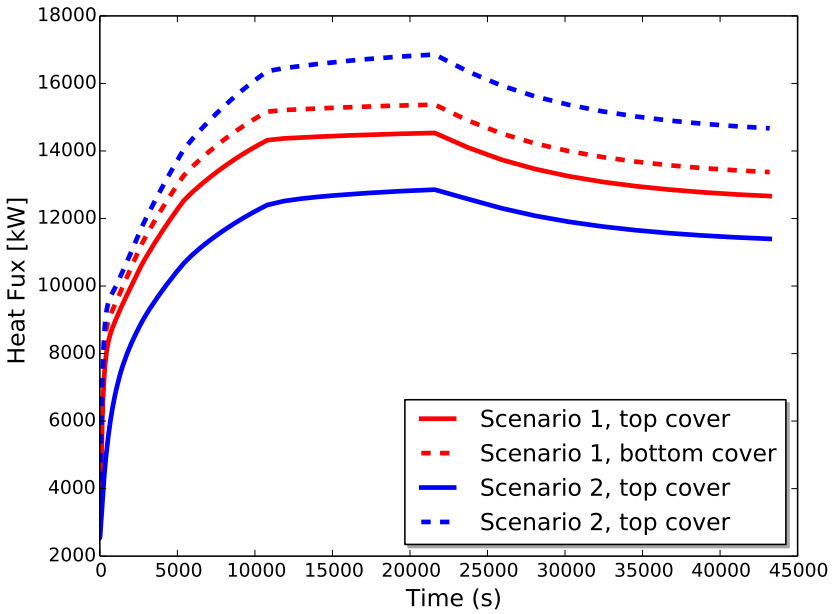

Figure 78: Heat flux along the accident for top and bottom covers

The radiation boundary conditions have been evaluated considering radiation to a black body at 22^oC and a surface emissivity of 0.6. If the black body temperature increases up to 200^oC the target external surface temperature will increase less that 50^o hence, the maximum temperature of the spallation material will be below 400^oC. Finally if we consider a low emissivity factor (0.3) in the black body, the maximum temperature increases up to $\sim 450^oC$ far below the 700^o limit.

The main conclusion for the shut-down case is that the maximum temperature in a conservative scenario is far below the requirements limit.

10.8 Conclusions for load cases

The Table 11 shows a summary of the main conditions for the spallation material for the design load cases. In all the cases maximum temperature and maximum stress values are below the limits described on Section 3. Taking into account that requirements for the spallation material already includes its own safety margin we can conclude that the design fulfill the design criteria.

	Temp. (^oC)	Max. Temp. (^oC)	Stress (σ)	Max. Stress (σ)
SF1: Nominal	444	500	77	100
SF2: Vertical	457	600	77	100
SF2: Unsynchronized	447	600	69	100
SF2: Channel block	518	600	91	100
SF2: W break	540	600	85	100
SF3: LOCA	647	700	-	-
SF3: Shut-down	330	700	-	-

Table 11: Load scenarios summary

11 Sensibility analysis

11.1 Nominal beam conditions

For the load scenarios described in the section 2 the heat source in the tungsten was produced by the design protons beam (Figure 38 and 39), the design beam includes the instrumentation uncertainty which means 20% more concentrated than the nominal beam. However this value is conservative, the heat generation, temperature and mechanical stress profiles obtained with the design beam are the highest possible during standard operation. In order to know a more realistic thermal and mechanical behaviour of the spallation material a CFD and FEM simulations employing the nominal beam to generate the thermal source were done. The loads are produced by the nominal beam under nominal frequency with the wheel at his nominal rotation speed. Also the beam is considered synchronized with the wheel and hitting in the center of the cassette. The cooling system is working at nominal conditions so helium mass flow trough the wheel is 3.0 kg/s which means 0.0833 kg/s in each cassette. Figures 38 and 39 shows the beam on nominal conditions.

The temperature and stress profile evolution of the spallation material during the low conductivity scenario are presented in the next figures. The solution has been obtained following the methodology described in the section 7 which means solve the described CFD and FEM models.

In the figure 79 is compared the tungsten maximum temperature time evolution during one pulse and subsequent cooling once reached the steady state employing the nominal and design beam. In the figures 80 and 81 it is shown respectively the temperature profile of the spallation material at the end of the cooling and at the end of a protons beam pulse for the low conductivity scenario. The maximum temperature at the end of the cooling is 338 °C and after the pulse is 416 °C. The tungsten maximum temperature at the end of the pulse achieved with the nominal beam is 26 °C below than employing the design beam.

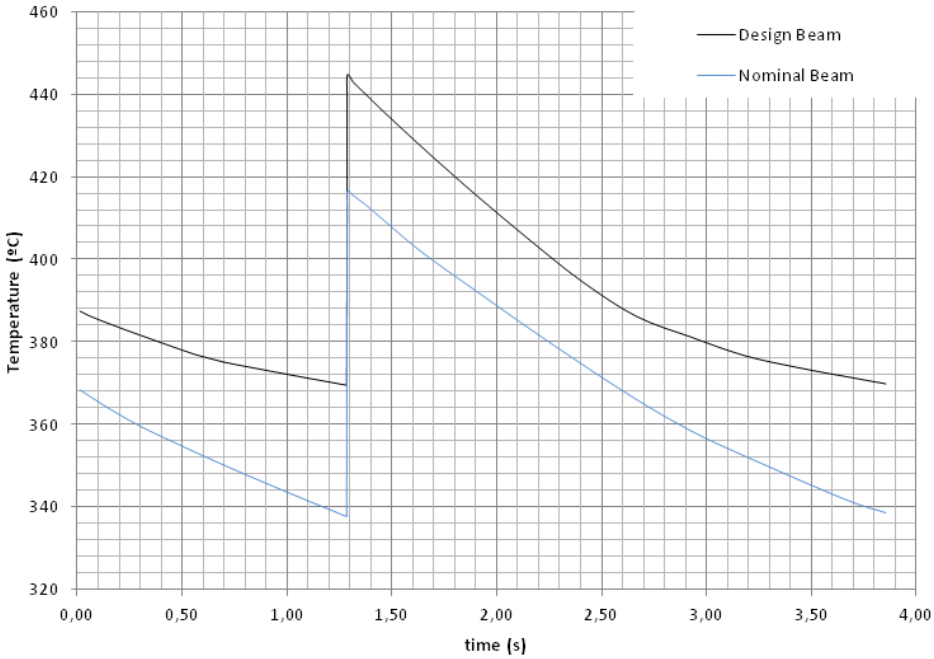

Figure 79: Time evolution of spallation material maximum temperature for Nominal beam conditions .

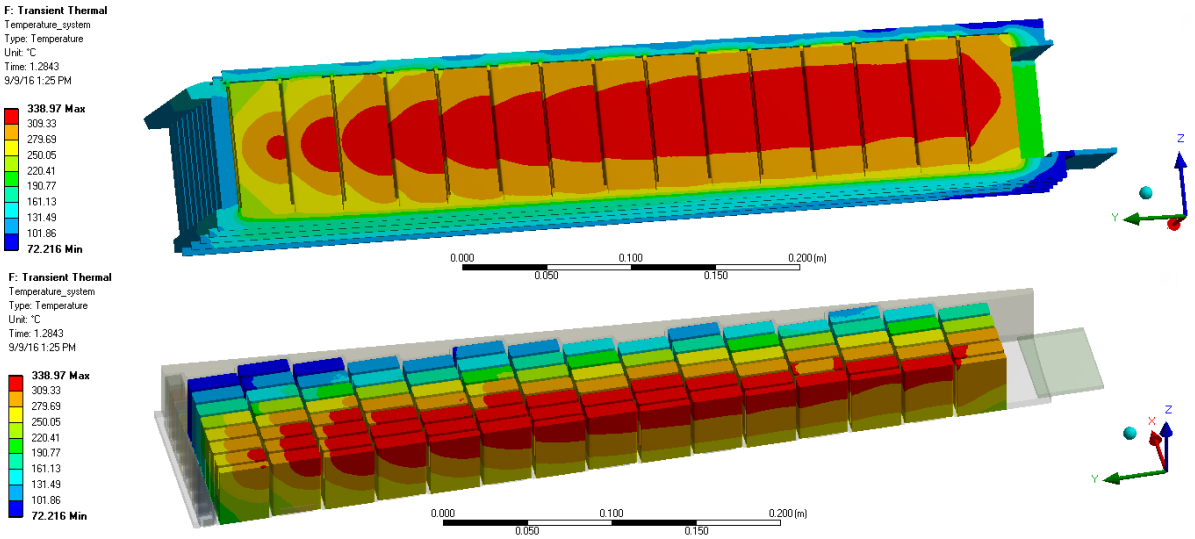

Figure 80: Temperature profile of the tungsten at the end of the cooling

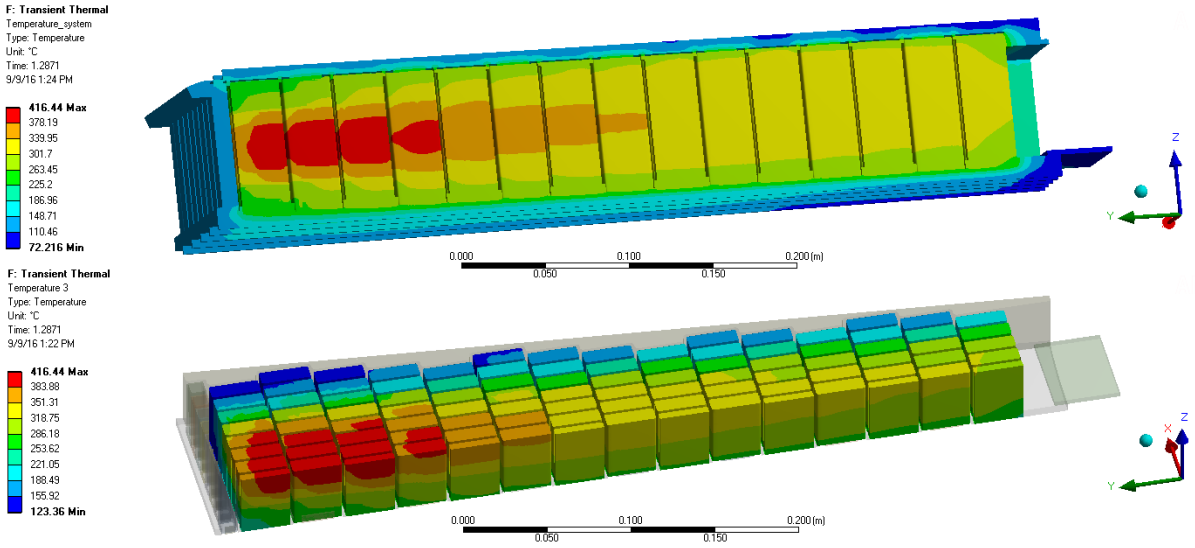

Figure 81: Temperature profile of the tungsten at the end of the pulse

In the figures 82 and 83 it is shown respectively the von-Mises equivalent stress profile of the spallation material at the end of the cooling and at the end of a proton beam pulse. The maximum stress at the end of the cooling is 40 MPa and after the pulse is 112 MPa. The stress profiles using the nominal beam and the design beam are very similar.

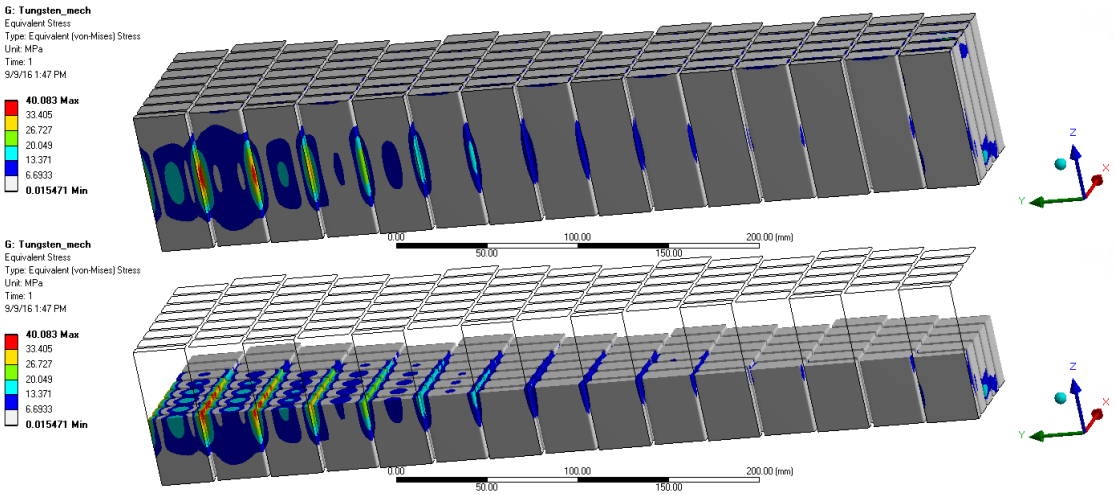

Figure 82: Von-Mises equivalent stress profile of the tungsten at the end of the cooling

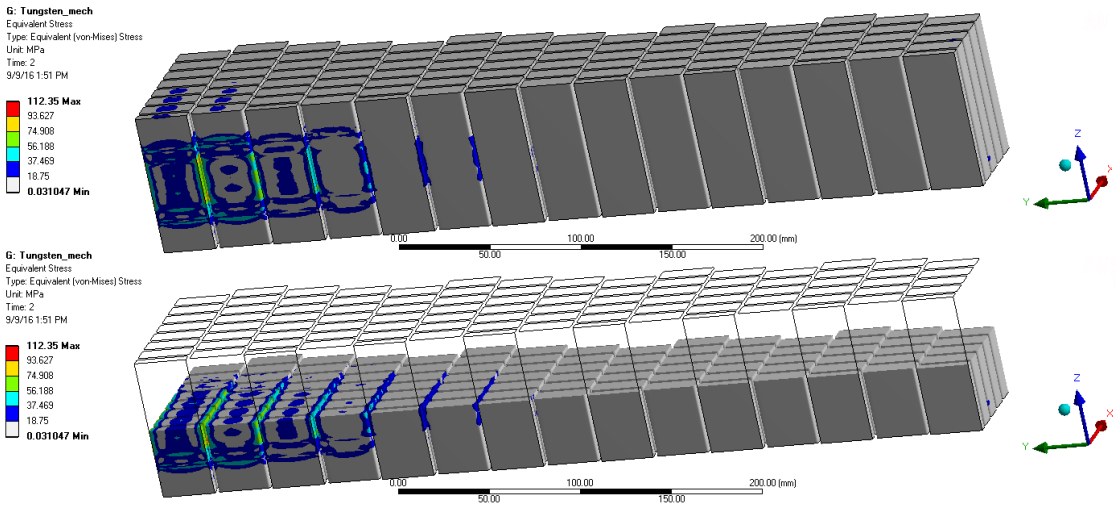

Figure 83: Von-Mises equivalent stress profile of the tungsten at the end of the pulse

11.2 Low conductivity

In order to study the influence of the spallation material thermal conductivity reduction due to the proton irradiation a CFD and FEM simulations were done. From the document ESS Target Materials Handbook [5] can be estimated that at the end of the Target life the thermal conductivity of the tungsten will be reduced by 20%.

The employed loads for the analysis are exactly the same as in the SF1 load scenario, which was described on section 2. These loads are produced by the design beam under nominal frequency with the wheel at his nominal rotation speed. Also the beam is considered synchronized with the wheel and hitting in the center of the cassette. The cooling system is working at nominal conditions so helium mass flow trough the wheel is 3.0 kg/s which means 0.0833 kg/s in each cassette. Figures 38 and 39 shows the beam on nominal conditions.

The temperature and stress profile evolution of the spallation material during the low conductivity scenario are presented in the next figures. The solution has been obtained following the methodology described in the section 7 which means solve the described CFD and FEM models.

In the figure 84 is compared the tungsten maximum temperature time evolution during one pulse and subsequent cooling once reached the steady state for the high and low conductivity scenarios. The temperature increase (ΔT) due to the beam pulse is practically the same in both scenarios, the short length of the pulse produces an adiabatic heating in which the thermal conductivity has no influence. In the figures 85 and 86 it is shown respectively the temperature profile of the spallation material at the end of the cooling and at the end of a protons beam pulse for the low conductivity scenario. The maximum temperature at the end of the cooling is 377 °C and after the pulse is 457 °C. The 20% decrease of the tungsten conductivity due to the irradiation leads to an increase of 12 °C in the system maximum temperature.

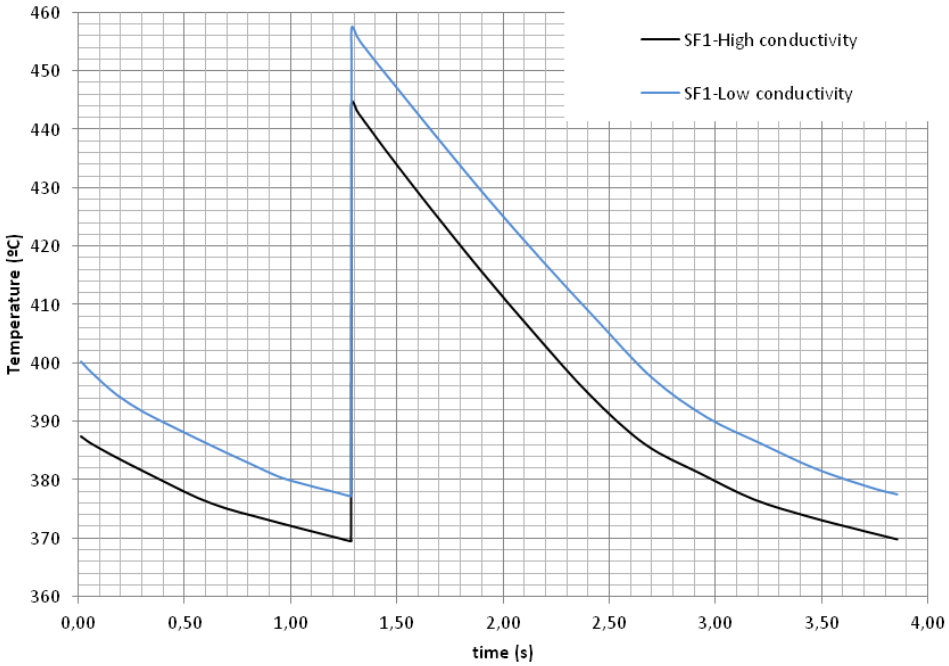

Figure 84: Time evolution of spallation material maximum temperature on SF1:High conductivity and SF1: Low conductivity.

In the figures 85 and 86 it is shown respectively the temperature profile of the spallation material at the end of the cooling and at the end of a protons beam pulse for the low conductivity scenario. The maximum temperature at the end of the cooling is 377 °C and after the pulse is 457 °C. The 20% decrease of the tungsten conductivity due to the irradiation leads to an increase of 12 °C in the system maximum temperature.africar venta

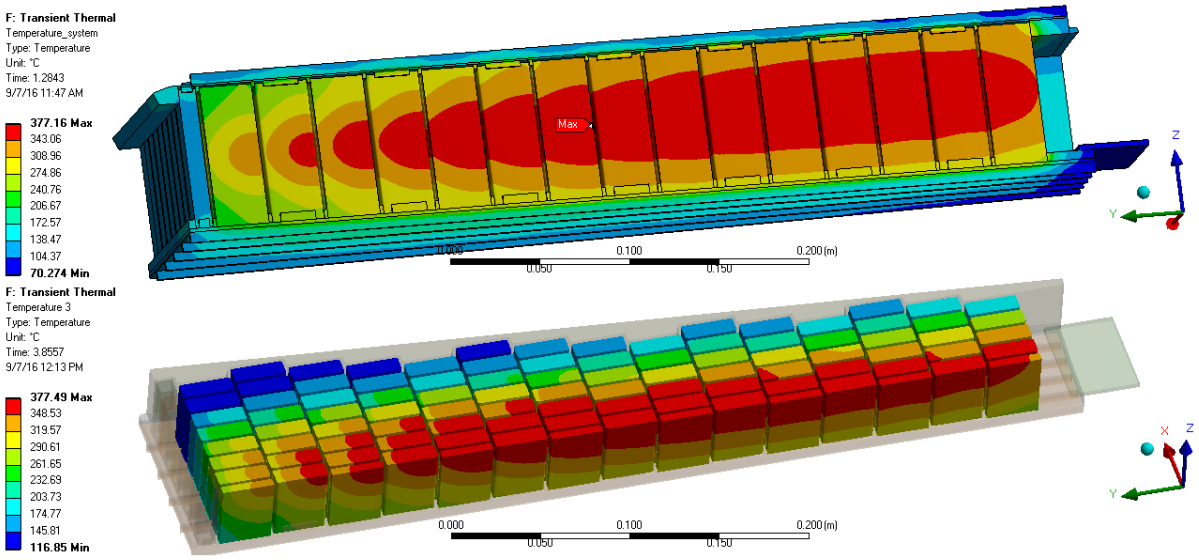

Figure 85: Temperature profile of the tungsten at the end of the cooling

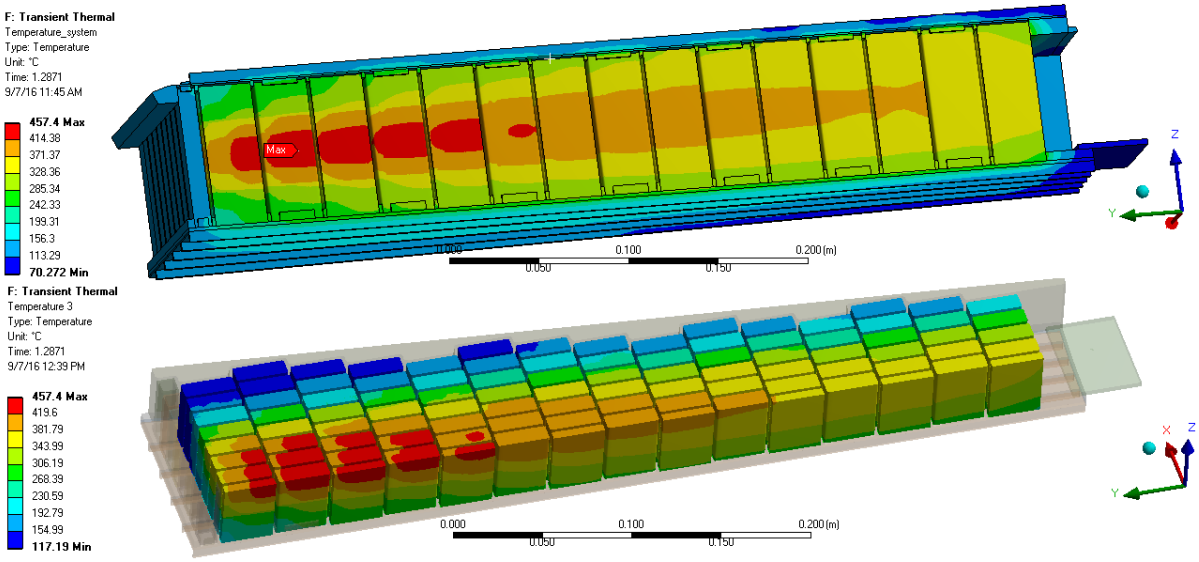

Figure 86: Temperature profile of the tungsten at the end of the pulse

In the figures **??** and **??** it is shown respectively the von-Mises equivalent stress profile of the spallation material at the end of the cooling and at the end of a proton beam pulse. The maximum stress at the end of the cooling is 56 MPa and after the pulse is 120 MPa. The 20% decrease of the tungsten conductivity due to the irradiation leads to an increase of 10 MPa in the spallation material maximum equivalent stress.

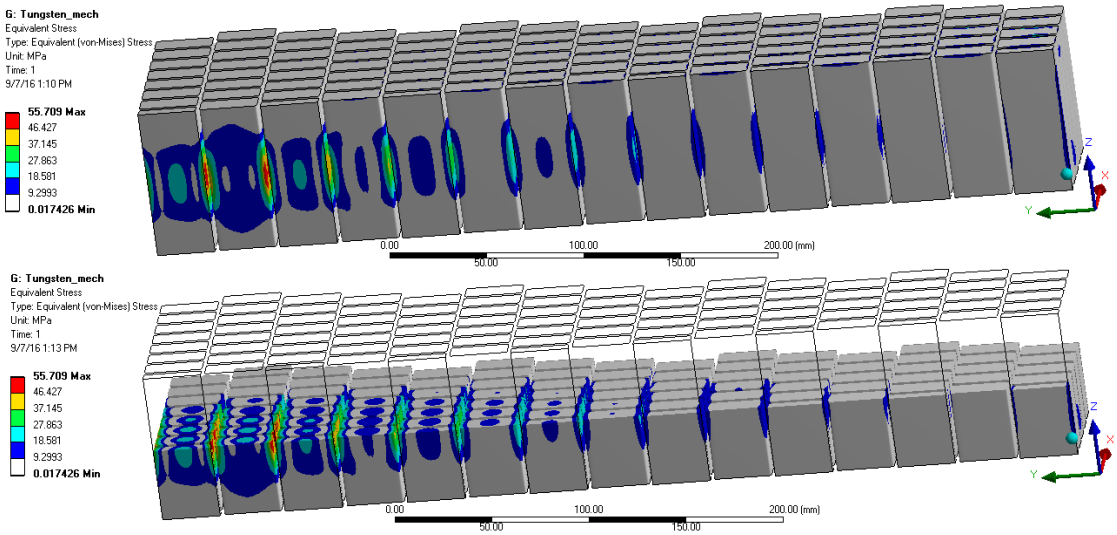

Figure 87: Von-Mises equivalent stress profile of the tungsten at the end of the cooling

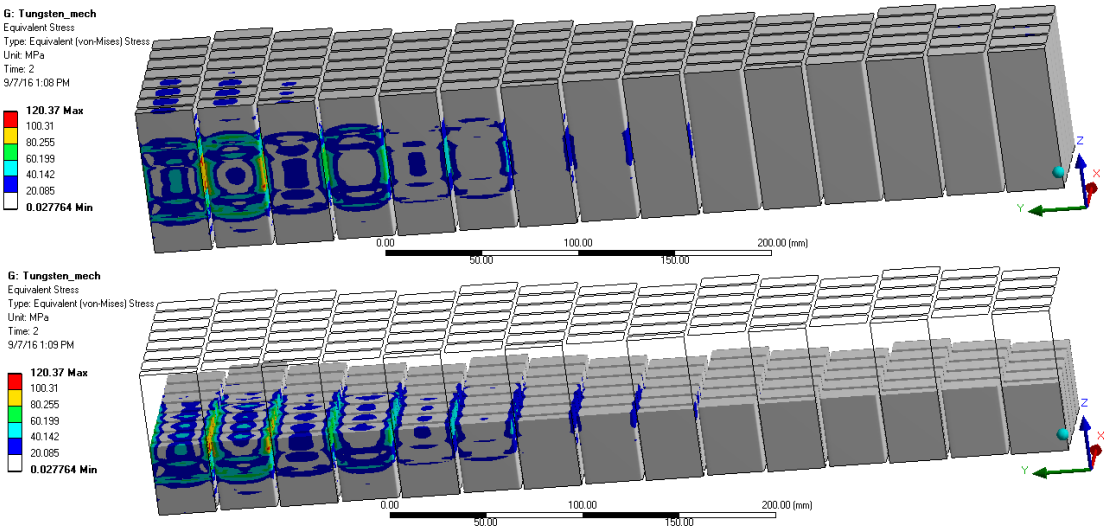

Figure 88: Von-Mises equivalent stress profile of the tungsten at the end of the pulse

11.3 Design power increase

In other to study the thermomechanical behaviour of the spallation material when the power of the design beam is increased by 4% keeping the same proton flux profile (Figures 38 and 39). The loads are produced by the design beam under nominal frequency with the wheel at his nominal rotation speed, however the protons current is increased by 4% which produces an increment of the beam power. Also the beam is considered synchronized with the wheel and hitting in the center of the cassette. The cooling system is working at nominal conditions so helium mass flow trough the wheel is 3.0 kg/s which means 0.0833 kg/s in each cassette.

In the figure 89 is compared the tungsten maximum temperature time evolution during one pulse and subsequent cooling once reached the steady state for the design beam at 100% and 104% power. The 4% power boost leads to an increase of 8 °C in the system maximum temperature. In the figures 90 and 91 it is shown respectively the temperature profile of the spallation material at the end of the cooling and at the end of a protons beam pulse for the design beam at 104% power. The maximum temperature at the end of the cooling is 379 °C and after the pulse is 453 °C.

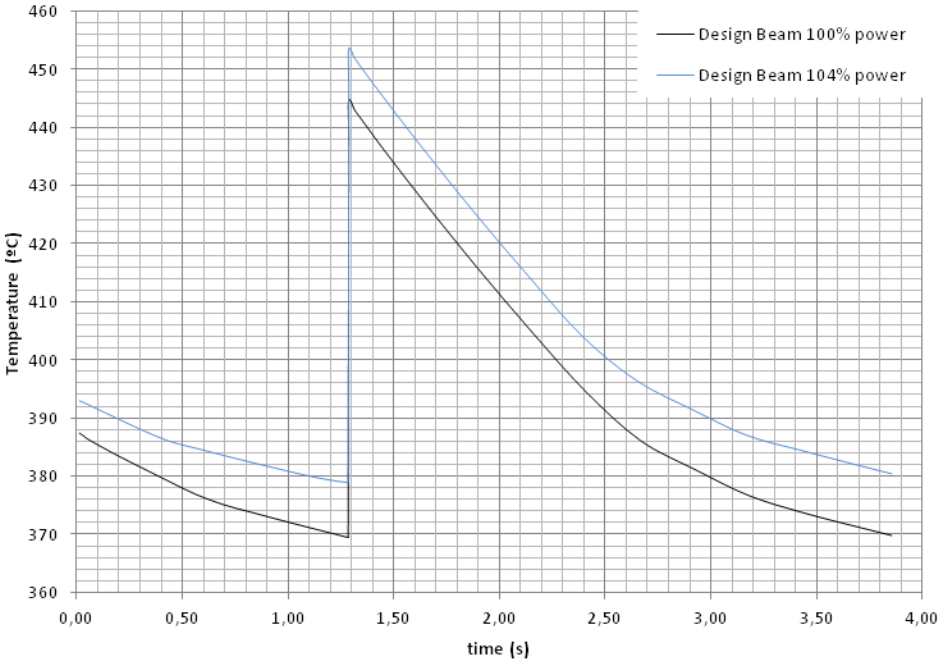

Figure 89: Time evolution of spallation material maximum temperature for design beam 100% power and 104%.

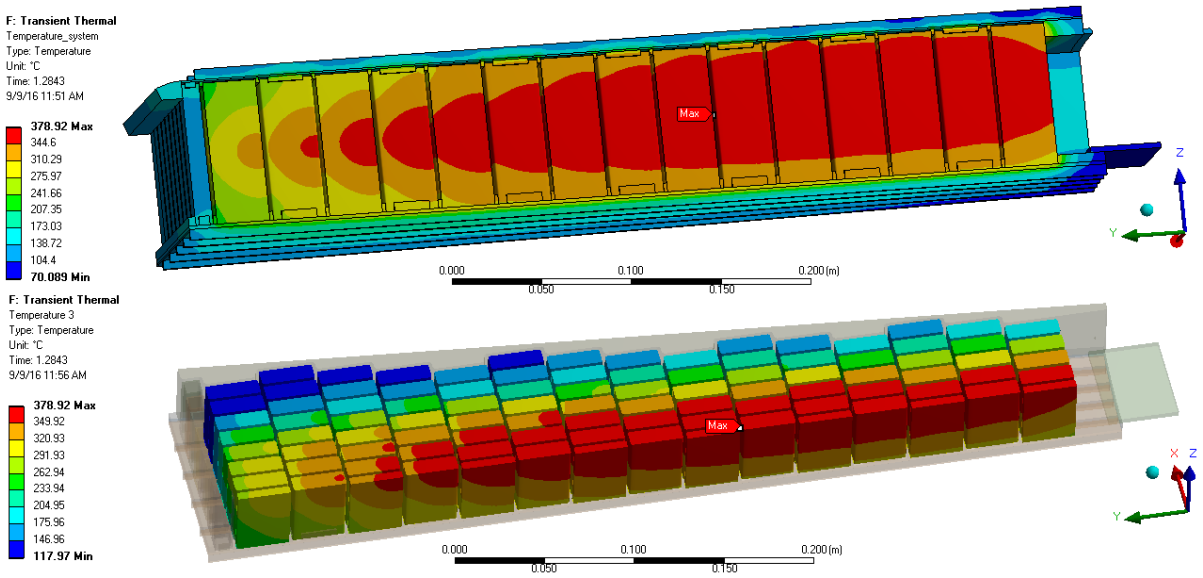

Figure 90: Temperature profile of the tungsten at the end of the cooling

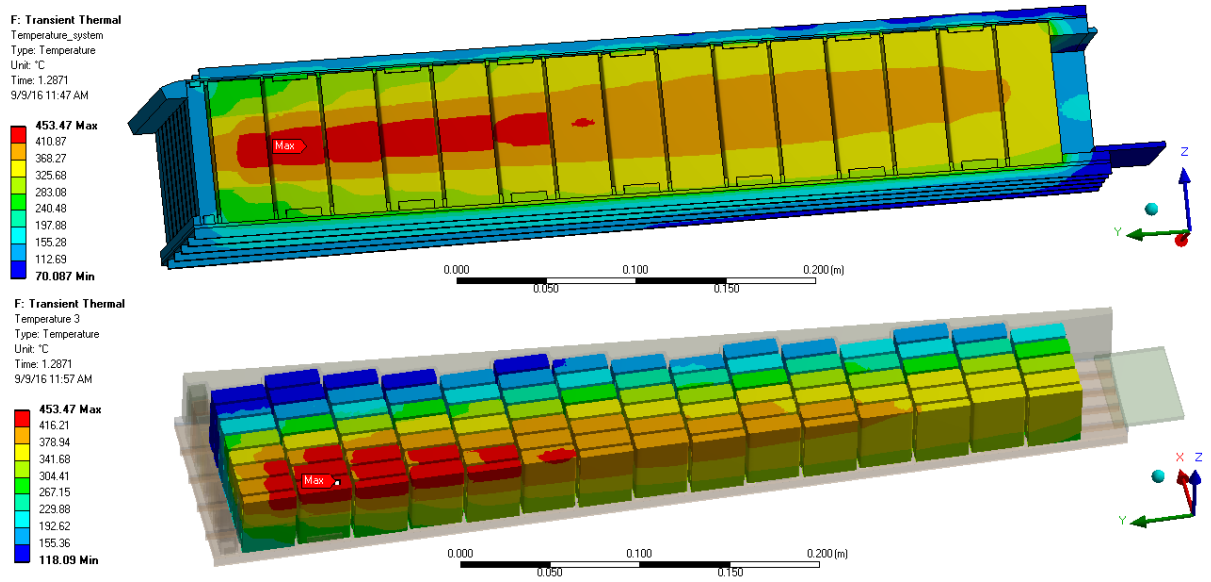

Figure 91: Temperature profile of the tungsten at the end of the pulse

In the figures 92 and 93 it is shown respectively the von-Mises equivalent stress profile of the spallation material at the end of the cooling and at the end of a proton beam pulse. The maximum stress at the end of the cooling is 41 MPa and after the pulse is 113 MPa.

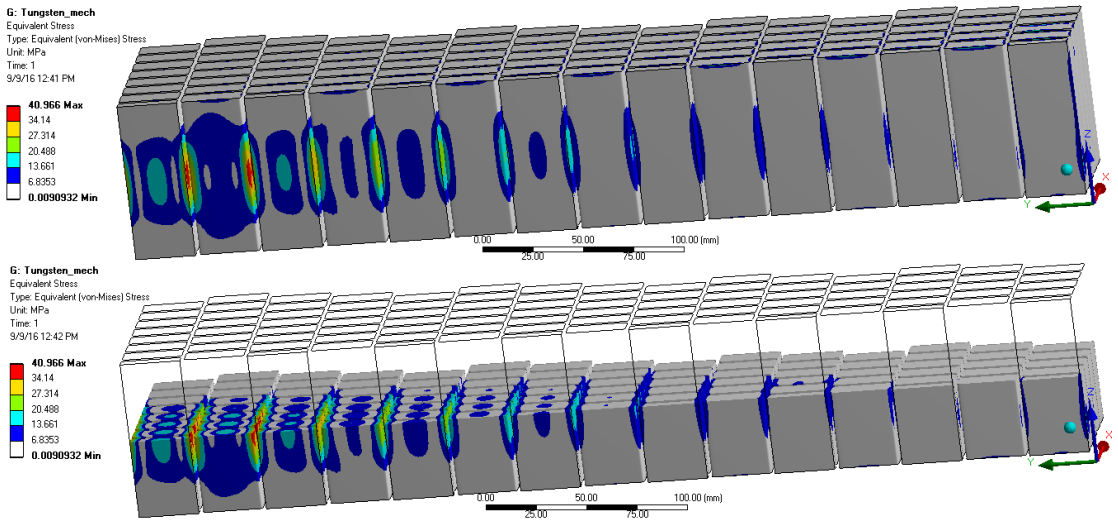

Figure 92: Von-Mises equivalent stress profile of the tungsten at the end of the cooling

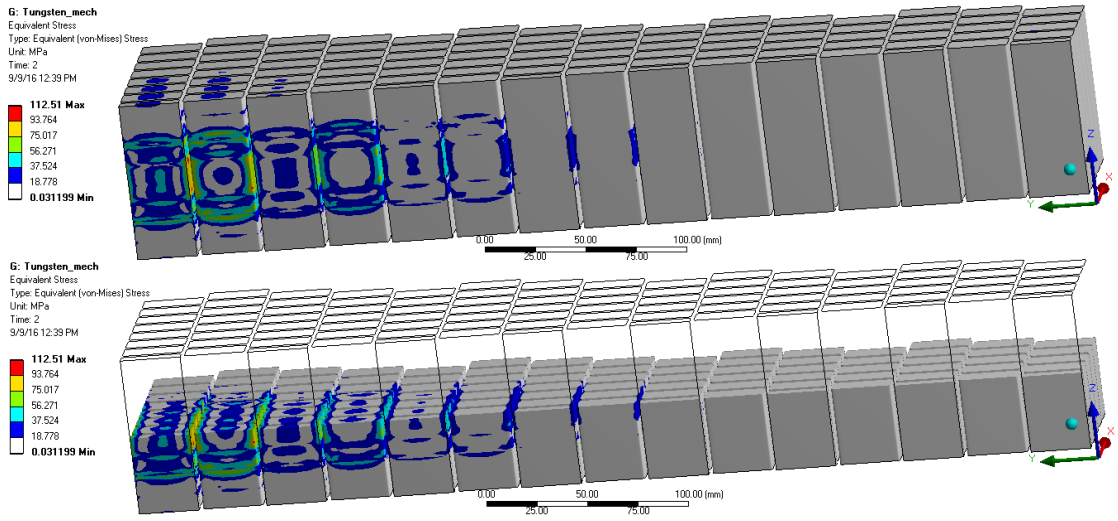

Figure 93: Von-Mises equivalent stress profile of the tungsten at the end of the pulse

11.4 Conclusions for sensibility analysis

The sensibility analysis results are summarized on Table 11. We can remark than the design is robust enough and any of the modifications in the design conditions produces significant increases of the temperature or stress. Even more, the conservative factors introduced by the design beam almost cover all the uncertainty associated to other factors. Hence, it can be concluded that the design is robust and its sensibility to the considered factors limited.

	Temp. (^oC)	Max. Temp. (^oC)	Stress (σ)	Max. Stress (σ)
Nominal Beam	420	500	76	100
Low conduct.	457	500	88	100
104 %	453	500	77	100

Table 12: Summary of sensibility cases

12 Spallation material supplier evaluation

The previous sections have analyze the behavior of the proposed solution according to the mechanical properties of the spallation material described on the ESS Materials Handbook. However, the production of tungsten is a complex process and quality assurance is critical for our application. Based on that, the proposed solution has been discussed with different tungsten suppliers. All of them has remark any special challenging associated with the geometry (bricks with rounded corners).

Following the qualification process, samples from 6 different suppliers has been summited to CEIT [21] for and extensive and detailed analysis in two steps. The description of this process is summarized on previous reports[22] [23]. The Table 96 shows the conclusion for the macroscopic analysis of the samples, as step 1. Based on this initial conclusions only 3 suppliers were considered for the second phase. Samples provided by supplier 1 were acceptable, however the analysis of the company shows a significant economical risk for that reason it was finally discarded. Goodfellow was not considered due to the lack on the traceability of the material.

On the second step, a detail microstructure analysis were perform (Figure 94). Material provided by 5 shows a grain structure not according to the hot rolled tungsten process, that means a high temperature recrystallization process has been carried on after the rolling process. This results agrees with the low surface residual stresses shown in the stage 1.

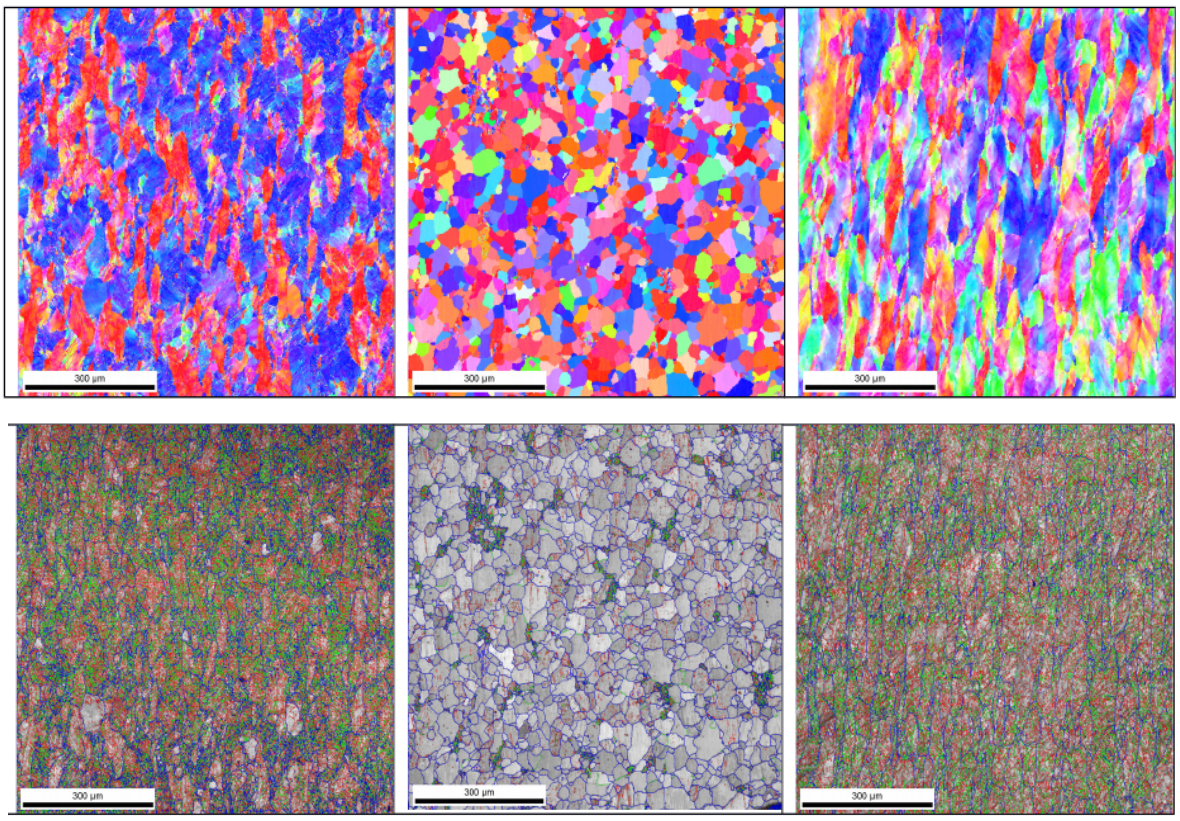

Figure 94: Grain structure in the middle plain. Microstructure of the samples in the second stage.

Hence, the material properties at working temperature are significantly worse that the other two. Based on these facts, the material from 5 is discarded.

Finally, microestructure of samples from 2 and 6 shows a clear directionality according to hot rolling processes. Figure 95 shows the transverse and longitudinal stress limit for both samples. Supplier 6 shows a much higher anisotropy in the mechanical properties so, taking into account the stress profiles produced by the proton beam, Supplier 2 structure is recommended.

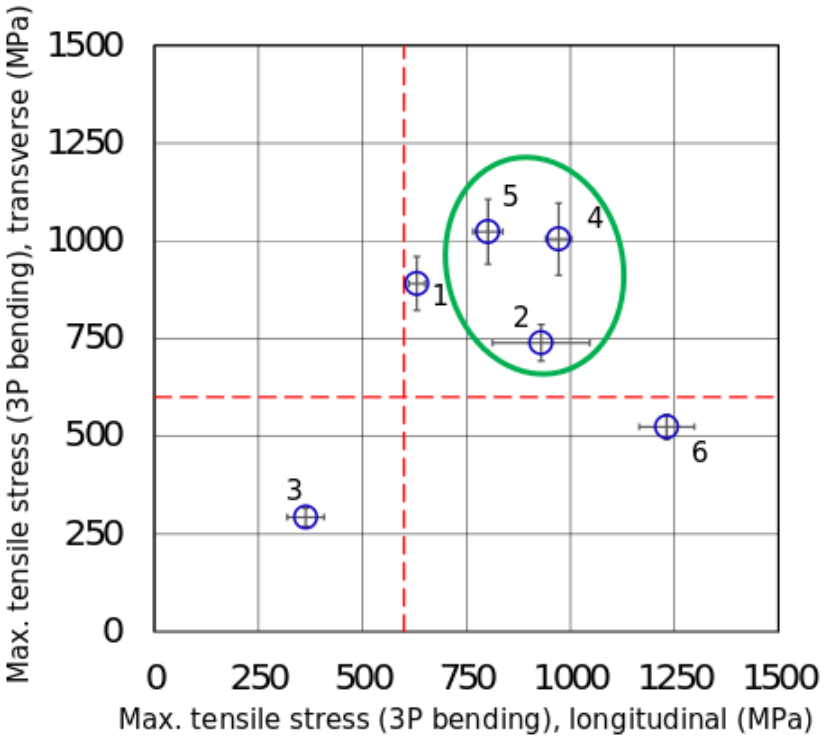

Figure 95: Longitudinal and transverse bending stress limit

The final conclusion of this analysis is that ESS-Bilbao has identify the best material for the proposed target geometry: Supplier 2. However, material provided by other supplier could be also acceptable, if they are able to fulfill the above mentioned mechanical parameters.

W supplier	Visual inspection	Density, ρ (g cm^{-3})		E, Young modulus RPN (GPa) ± assoc. error	HV (1 kg) RP (kg mm^{-2}) ± 95% cl	Res. stresses, surface (MPa) ± sd		Fractography	Chemical composition Impurities above threshold
		Geom. ± assoc. error	Water displ. ± sd			σ_{11} (LD)	σ_{22} (TD)		
1	Grey spots (oxide) on surface	19.22 ±0.03	18.95 ±0.22	403.9 ±0.7	423.7 ±25.7	-1276 ±9	-1074 ±13	Brittle, transgranular, distorted cleavage , oriented facets Minor intergranular fraction Scarce nano-porosity	-
2	Thin continuous (oxide) layer on surface	19.16 ±0.03	19.21 ±0.03	405.9 ±0.8	496.5 ±9.5	-789 ± 11	-1088 ± 9	Brittle, transgranular, distorted cleavage , oriented facets Minor intergranular fraction Some micro-porosity	-
3	Damaged edges. Scratches on surface, slightly oxidized (finger prints).	18.27 ±0.03	17.69 ±0.03	364.9 ±0.7	355 ±6	-956 ± 20	-1166 ± 8	Brittle, intergranular fracture, equiaxed grains, high porosity Some precs. at grain edges	-
4	Bright smooth surface, free from oxides	19.24 ±0.03	19.20 ±0.03	408.1 ±0.8	496 ±6.0	-225 ± 27	-1113 ± 11	Brittle, transgranular, distorted cleavage , oriented facets Minor intergranular fraction Scarce nano-porosity	-
5	Brightest, smoothest surface. Free from oxides	19.22 ±0.03	19.23 ±0.01	406.4 ±0.8	412 ±16	-230 ±24	-247 ±26	Brittle, transgranular, distorted cleavage , oriented facets Minor intergranular fraction Scarce nano-porosity	>30 ppm O (44 ppm)
6	Rough surface, free from oxides. Bricks slightly shorter?	19.26 ±0.03	19.15 ±0.05	391.4 ±0.7	470 ±5.0	-709 ± 18	-1055 ± 7	Brittle, transgranular, distorted cleavage , oriented facets Minor intergranular fraction Porosity not detected	-

Figure 96: Summary of the initial analysis of tungsten provided by 6 different suppliers

13 Spallation material Quality control

Previous section summarizes the quality analysis performed for several tungsten suppliers all over the world. The process allows to evaluate the critical parameters that have to be considered to guarantee the performance of the spallation material. Based on that, ESS-Bilbao has established the criteria that has to be fulfill by the supplier and the tests that have to be completed in the acceptance process. The extensive description of the statistical sampling process is described on CEIT reports[24].

13.1 Material requirements

The following requirements will be included in the Call for Tender. The supplier mush performed and documented the appropriate test in factory to prove that the material fulfill all the requirements before shipping.

Trazability

The bricks will be identify individually along all the production process.

Material produced by hot rolling

The material will have directional structure associated with the hot rolling process with clear grain elongation along the rolling direction. Annealing processes after the rolling should be avoided.

The material on its final shape will have compressive residual surface stresses in the longitudinal and transverse direction above 500 MPa. The residual stresses will be measured by X-ray diffraction or equivalent technique (ASTM E2860-12).

Chemical composition:

The amount of impurities of critical elements have to be evaluated:

- O and N concentration below 30 ppm. The concentration should be measured by inert gas fusion method or equivalent (ASTM E1569-09)
- C and S concentration below 30 and 10 ppm, respectively. The concentration should be measured by the induction furnace method or equivalent (ASTM E 1941-10)

Density

The minimum admissible density should be 19.0 $g \cdot cm^3$ measured at room temperature by water displacement method (ASTM B311-12) or equivalent standard.

Dimensional control

Bricks dimensions will be control according to the drawings included on section 15.

Tensile fracture stress in longitudinal direction

The mean RT fracture stress on longitudinal direction will be above 600 MPa at room temperature measured according to ATSM E8/E8M-15a or equivalent standard.

The supplier will provide the statistical probability distribution and its standard deviation. This information will be consider for the final definition of the number of pieces to be tested in the acceptance process.

13.2 Acceptance test

The acceptance of the spallation material will be done after several pieces (bricks) are tested in order to verify the supplier process. The test will be perform at ESS-Bilbao facilities or it will be subcontracted to a qualify third party body.

Metrology

A significant number of samples (100-200) will be individually measured to check the external dimensions of the brick (including density).

Tensile test

According to [24], a statistical sampling plan will be defined according to the data provided by the supplier. A representative number of bricks (40-100 bricks) will be tested to confirm the supplier distribution.

The tensile stresses will be evaluated by means of bending test at room temperature in longitudinal direction. For this tests, bricks as received from the supplier will be analyzed, in order to avoid machining processes. The test will confirm the statistical distribution provided by the supplier.

Structural inspection

Three samples from the tensile test population (those having the lower, mid and highest fracture stress) will be analyzed by SEM-EBSD metallography in longitudinal direction. The analysis will consider large enough areas containing a number of grains larger that 400. The test should show a clear directionality in the grain distribution with significant elongation in the rolling direction.

Surface residual stress

Three samples will be analyzed by means of X-ray diffraction according to ASTM E2860-12. The analysis will confirm the surface residual stress distribution provided by the supplier.

14 Conclusions

The previous sections shows the design process carried on for the design of the spallation material for the ESS Target. The following conclusions can be remarked

- The Methodology developed for the analysis allows to evaluate all the physical processes of interest for the spallation material (damage, activation, thermal and mechanical conditions).
- The analysis of the design scenarios shows enough safety margin on nominal (SF1) and accidental conditions conditions (SF2 and SF3).
- The sensitivity analysis shows a robust design with low sensibility to change in the boundary conditions.
- The characterization process of the different suppliers shows that the demanded mechanical conditions are achievable for several supplier. However, one of then shows better mechanical properties.
- The proposed process for the procurement can guaranty a high quality standard in the material.

15 Drawings

Front view
Scale: 2:1

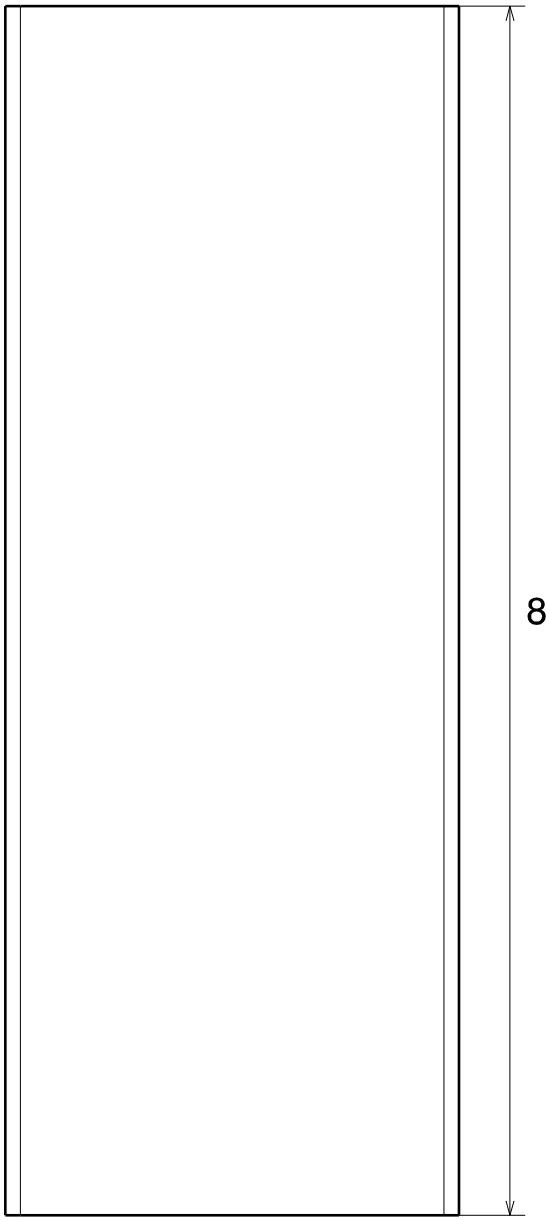

Top view
Scale: 2:1

Rounded corners: R = 1mm

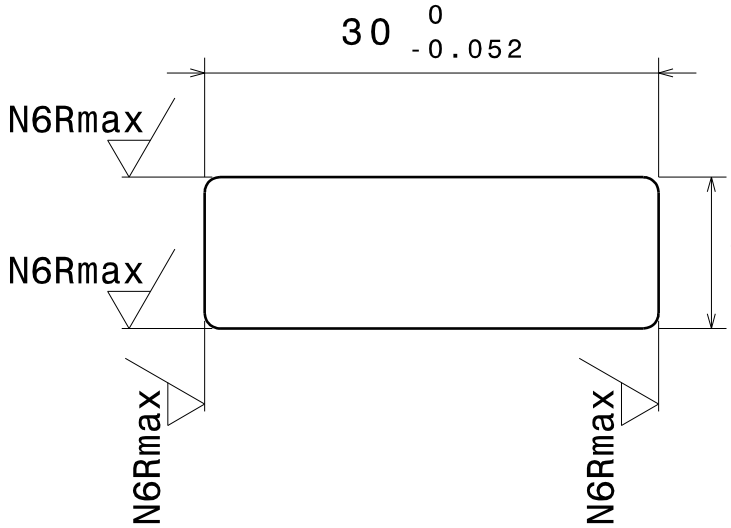

Isometric view

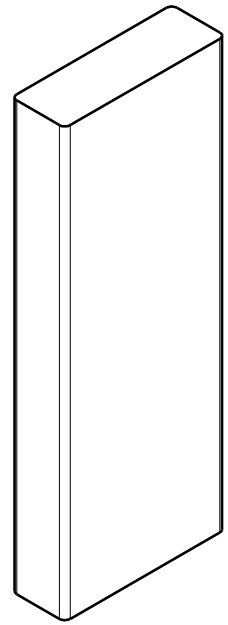

Projection	Finishing	T.	Linear dimensions (mm)							Broken edges (mm)			Angular dimensions (mm)				
	Break and deburr all sharp edges	>	0,5	6	30	120	400	1.000	2.000	0,5	3	6	-	10	50	120	400
		≤	6	30	120	400	1.000	2.000	4.000	3	6	-	10	50	120	400	-
Ra DIN		V.	± 0,1	± 0,2	± 0,3	± 0,5	± 0,8	± 1,2	± 2,0	± 0,2	± 0,5	± 1,0	± 1°	± 30'	± 20'	± 10'	± 5'

50 µm	N12	Title	ESS BILBAO TARGET		General threads tolerances: DIN 13 6H - 6g
		Description	Tungsten Bar		General tolerances for form: ISO 2768-2(K)
6,3 µm	N9	Drawing n°	Dimensions	Dimensions in mm	General dimensional tolerances: ISO 2768-1(m)
		Rev. 02	Name	Date	
0,8 µm	N6	Designed	RSM	10/03/2016	
		Drawn	RSM	10/03/2016	
0,1 µm	N3	Checked	----------	--/--/----	
		Rounded corners and roughness mod.			

Polígono Industrial Júndiz
C/ Basaldea, 23 C
01015 Vitoria - Gasteiz
SPAIN
Tfno.: +34 945 290 121
www.essbilbao.org

Format A4

Sheet 01 de 01

References

[1] Reference is needed.

[2] Lebarbe, T., et al. "Presentation of the Afcen RCC-MRx Code for Sodium Reactors (SFR), Research Reactors (RR) and Fusion (ITER): General Overview." ASME 2010 Pressure Vessels and Piping Division/K-PVP Conference. American Society of Mechanical Engineers, 2010.

[3] ESS-0037038: Load Cases, Classification and system parts Target Wheel, Drive and Shaft

[4] ESS-0003310: Beam on Target Requirements

[5] ESS Target Materials Handbook (ESS-0028465)

[6] ESS-0009043: Requirements for maximum stress and maximum temperature in proton-irradiated tungsten

[7] Andersen, K. "ESS Technical Design Report." (2012).

[8] ESS-0036673: ESS-Bilbao Target Proposal

[9] F.J. Alonso, J. Sanz, J.M. Perlado, Daño en materiales estructurales candidatos para un reactor comercial de fusión, DENIM 198, 1989

[10] ESS-0055645: Vibration Test

[11] Dai, Y., et al. "The second SINQ target irradiation program, STIP-II." Journal of nuclear materials 343.1 (2005): 33-44.

[12] SuperMC/MCAM 5.2 User Manual, Institute of Nuclear Energy Safety Technology, CAS

[13] ESS-0051512: Neutron Activation Analysis ESS

[14] Sanz, J., O. Cabellos, and N. García-Herranz. "ACAB-2008, ACtivation ABacus Code V2008." NEA Data Bank NEA-1839 (2008).

[15] Goorley, T., et al. "Initial MCNP6 release overview." Nuclear Technology 180.3 (2012): 298-315.

[16] ESS-0037287: Radiation Damage Analysis for the ESS Target

[17] ESS-0066301: Target, Shaft and Rotating seal CFD analysis

[18] K. K. Gudima M. I. Baznat et al CEM03.S1, CEM03.G1, LAQGSM03.S1, and LAQGSM03.G1 Versions of CEM03.01 and LAQGSM03.01 Event-Generators. Technical report, Los Alamos National Laboratory, March 2006

[19] Incropera, Frank P.; DeWitt, David P. (2000). Fundamentals of Heat and Mass Transfer (4th ed.). New York: Wiley. p. 493. ISBN 0-471-30460-3.

[20] MCNPX user's Manual. Version 2.6.0. 2007

[21] ESS-0036739: J. Gil Sevillano, A testing protocol for selection of tungsten bricks for the target of the European Spallation Source.

[22] ESS-0066195: J. Gil Sevillano, Assessment of six batches of tungsten bricks (intended for the target of the ESS) according to a technical selection protocol agreed with ESS-Bilbao. Stage 1 results

[23] ESS-0066192: J. Gil Sevillano, Assessment of tungsten bricks (intended for the target of the ESS) according to a technical selection protocol agreed with ESS-Bilbao. Stage 2 results of tests of three batches selected after Stage 1

[24] Reference is needed